

RICE UNIVERSITY

**Hot-Carrier-Mediated Chemical Processes in Plasmonic
Photocatalysis**

by

Linan Zhou

A THESIS SUBMITTED
IN PARTIAL FULFILLMENT OF THE
REQUIREMENTS FOR THE DEGREE

Doctor of Philosophy

APPROVED, THESIS COMMITTEE



Naomi J. Halas, Chair
Stanley C. Moore Professor in Electrical
and Computer Engineering
Professor of Biomedical Engineering,
Chemistry, Physics and Astronomy
Director, Laboratory for Nanophotonics
Director, Smalley-Curl Institute



Peter Nordlander
Wiess Chair and Professor of Physics and
Astronomy
Professor of Electrical and Computer
Engineering



Stephan Link
Professor of Chemistry, Electrical and
Computer Engineering

HOUSTON, TEXAS

November 2018

Copyright

Linan Zhou

2018

ABSTRACT

Hot-Carrier-Mediated Chemical Processes in Plasmonic Photocatalysis

by

Linan Zhou

Plasmonic nanomaterials, featured with high optical cross-section resulted from the induction of the collective oscillation of free electrons in metallic nanostructures, known as localized surface plasmon resonance, by the alternative electromagnetic wave in light, is emerging as a new promising photocatalyst. Hot carriers derived from the non-radiative decay of LSPR are capable in activating chemical bond, in an intrinsically different mechanism from the conventional thermal-driven means, and provide the possibility in achieving chemical transformation in milder conditions with sustainable energy. When further combined with catalytically active materials in a synergic way to form the antenna-reactor complexes, the versatility and efficiency of plasmonic photocatalysts are greatly boosted. In this thesis, I will present four plasmonic photocatalysts, classified into two categories, for three reactions to show the stepwise understanding of the structure-property-function relationship in plasmonic photocatalysts and subsequent improvement in the design of photocatalysts. The first part, including chapters 3 and 4, involves applying monometallic plasmonic nanomaterials in H₂ activation. Au and Al nanomaterials, though being inert towards H₂ activation if driven thermally, are demonstrated to be active in hydrogen dissociation under light excitation. They both

exhibit linear intensity dependence in photocatalytic H₂-D₂ exchange reaction and H-H bond activated by the electronic transition of initial hot carriers is proposed to be the dominated mechanism. In contrast, Cu nanoparticles exhibit an S-shape intensity dependence in photocatalytic H₂-D₂ exchange reaction with a more-than-1 external quantum yield of light-to-chemical conversion. The hot carrier multiplication resulted from thermalization of hot carriers through electron-electron scattering plays a crucial role in the Cu system. The rate-determining step (RDS) is believed to be associative desorption of HD, different from the dissociative adsorption of H₂/D₂ on Au and Al surface, making the transition barrier of hot carriers low and the thermalized hot carriers effective. Next, I designed a new antenna-reactor structure, surface alloy, to incorporate materials with the favorable electronic structure for activation of specific molecules into plasmonic nanomaterials with intent to achieve better usage of hot carriers. Cu-Ru surface alloy was prepared and shows highly efficient photocatalytic activity towards ammonia decomposition reaction, making it feasible for studying the effect of plasmon-mediated hot carriers on the activation barrier of chemical reactions. By carefully tuning the loading ratio of Cu and Ru, I further synthesized single-atom-alloy plasmonic photocatalyst composed of a Cu core antenna with atomically dispersed Ru sites reactor on the surface. This antenna-reactor complex exhibits outstanding coke resistance in methane dry reforming reaction under illumination. Both of the hot carriers and single-atom structure were demonstrated to be essential for the observed stability. This thesis increases the knowledge in the mechanism of hot-carrier-mediated chemical reaction and guides the design of new generation of plasmonic photocatalysts.

Acknowledgments

With this thesis, I would love to thank everyone who has accompanied me along this journey. I would love to thank my thesis advisor, Professor Naomi Halas, for her continuous support and encouragement to me. I am deeply impressed by her enthusiasm in scientific research and erudite knowledge in both physics and chemistry. Her spirit of exploring truth inspires me to think critically and devote my whole life in science. I appreciate her for all the opportunities and favors she provided to help improve my skills in doing research as well as presenting the ideas in both oral and writing forms, and help me grow.

I would love to thank Professor Peter Nordlander, my kindly scientific mentor and collaborator for sharing his knowledge and ideas in plasmonics and surface science. I would also love to thank Professor Stephan Link for the inspiring discussions we had on the topic of hot carriers. I appreciate the favors that all the past and current Halas group members have ever offered, and will offer, to me. In particular, I would love to thank Dr. Chao Zhang for helping me solve experimental problems with his expertise in physics and optics, and having insightful and inspiring discussions with me throughout my graduate career. I would like to thank Halas group members, Nordlander group members and Rice staffs: Dr. Shaunak Mukherjee, Dr. Amanda Goodman, Dr. Michael McClain, Dr. Sam Gottheim, Dr. Hangqi Zhao, Dr. Jun Liu, Dayne Swearer, Hossein Robotjazi, Minhan Lou, Dr. Surbhi Lal, Dr. Yu Zhang, Dr. Nathan Hogan, Luke Henderson, Dr. Fangfang Wen, Dr. Oara Neumann, Dr. Ming Lun Tseng, Dr. Andrea Schlather, Dr. Bob Zhang, Dr. Adam Lauchner, Dr. Ciceron

Ayala-Orozco, Liangliang Dong, Shu Tian, Benjamin Cerjan, Michael Semmlinger, Jian Yang, Dr. Yue Zhang, Lin Yuan, Minghe Lou, Dr. Bo Chen, and Dr. Wenhua Guo, Dr. Alessandro Alabastri, Dr. Nicholas Large and Dr. Alejandro Manjavacas for contributing to this thesis and creating such an enjoyable environment.

I would love to thank my collaborators from Princeton University, Dr. Caroline Krauter, Dr. John Mark Martirez and Professor Emily Carter, for their kindly help and input in quantum mechanical calculations.

I would love to thank Professor Phillips Christopher in UCSB for his constructive comments and suggestion. His inspiring ideas and philosophy also deeply influence my perception of science and research. I would love to thank Henry Everitt from Duke University for his organization of an online seminar on heterogeneous catalysis and involvement in many discussion about my research.

I would love to thank my friends: Dr. Ruquan Ye, Dr. Bin Huang, Dr. Yufan Zhang, Dr. Xiaoyu Bai, Dr. Mingyang Liu, Dr. Ruocheng Yu, Dr. Xiqian Jiang, Xinxin Li, Yingying Xu for their daily caring.

Also, I would love to thank my colleagues in Syzygy Plasmonics: Trevor Best, Dr. Suman Khatiwada, Dr. Shreya Shah and John Welch for their effort in realizing the commercialization of the technique that I co-invented in the lab and increasing the impact of plasmonic photocatalysis in the society.

Finally, I would love to thank my families, in particular, my mom Liping Yan and my dad Jianyou Zhou. Their unconditional support is extremely important and essential to all the achievement I have made. They are the mentally perpetual motion for me to pursue my dream.

Contents

Hot-Carrier-Mediated Chemical Processes in Plasmonic Photocatalysis	i
Acknowledgments.....	v
Contents	vii
List of Figures	ix
List of Tables	xvii
List of Equations.....	xviii
Nomenclature	xix
Introduction.....	1
Plasmon decay and hot-carrier-mediated chemical processes	7
2.1. Localized surface plasmon resonance.....	7
2.2. Plasmon decay.....	10
2.3. Hot-carrier-mediated chemical process.....	13
H₂ activation by hot carriers on plasmonic metal nanoparticles.....	17
3.1. Hydrogen activation	17
3.2. Supported gold nanoparticles as a photocatalytic platform for hot-carrier-mediated H ₂ dissociation	18
3.2.1. Synthesis and characterization of Au/SiO ₂ photocatalyst.....	18
3.2.2. Photocatalytic H ₂ -D ₂ exchange reaction on Au/SiO ₂	20
3.3. Plasmonic aluminum nanocrystals for photocatalytic H ₂ dissociation	28
3.3.1. Synthesis and characterization of Al nanocrystals (NCs) and γ -Al ₂ O ₃ supported Al NCs.....	29
3.3.2. Photocatalytic H ₂ -D ₂ exchange reaction on Al NCs/ γ -Al ₂ O ₃	32
3.4. Conclusion	37
Appendix A	38
Demonstration of hot carrier multiplication in plasmonic photocatalysis	39
4.1. Initial hot carriers versus thermalized hot carriers.....	39
4.2. Synthesis and characterization of supported copper NPs	40
4.3. Photocatalytic H ₂ -D ₂ exchange on Cu/MgO-Al ₂ O ₃	45

4.4. Quantification of the photothermal effect	47
4.5. Demonstration of the thermalized-hot-carrier mechanism	52
4.6. Conclusion	56
Appendix B.....	58
Surface alloy as a promising antenna-reactor structure for plasmonic photocatalysis	60
5.1. Antenna-reactor plasmonic photocatalysts.....	60
5.2. Ru-on-Cu surface alloy for photocatalytic ammonia decomposition	62
5.2.1. Synthesis and characterization of photocatalysts.....	62
5.2.2. Photocatalytic ammonia decomposition for hydrogen storage	67
5.2.3. Light-dependent activation barrier	72
5.3. Conclusion	80
Coke-resistant methane activation by single-atom-alloy plasmonic photocatalysts ...	81
6.1. Methane activation	81
6.2. Light-driven methane dry reforming with Ru-on-Cu single-atom-alloy photocatalysts	82
6.2.1. Synthesis and characterization of Cu-Ru single atom alloy.....	82
6.2.2. Photocatalytic performance of Ru-on-Cu surface alloys with different Ru loading for methane dry reforming.....	87
6.2.3. Photo- vs. thermo- catalysis on the single-atom-alloy catalyst with $\text{Cu}_{19.8}\text{Ru}_{0.2}$ composition	94
6.2.4. Energy efficiency and reaction conversion consideration	98
6.3. Conclusion	100
Appendix C.....	101
Reference.....	105

List of Figures

Figure 2.1 (a) Schematics of excitation of LSPR in plasmonic metal nanoparticles by the electromagnetic wave of light. (b) Representative UV-Vis extinction spectrum of a gold NPs solution. (c) Left panel: Normalized extinction spectra of spherical Ag (38 ± 12 nm diameter), Au (25 ± 5 nm) and Cu (133 ± 23 nm) particles. The metal extinction is a consequence of the excitation of surface plasmon resonance. Dashed portions of the metal extinction curves indicate interband transitions; Middle panel: Normalized extinction spectra for Ag wire, cube and sphere nanoparticles. Wire-shaped particles are 90 ± 12 nm diameter and >30 aspect ratio, cubic particles are 79 ± 12 nm edge length and spherical particles are 38 ± 12 nm diameter; right panel: Normalized extinction spectra for Ag nanocubes as a function of size (56 ± 8 nm, 79 ± 13 nm and 129 ± 7 nm edge lengths correspond to orange, red and blue spectra respectively). The inset shows a photograph of the three nanocube samples suspended in ethanol. ²¹ 9

Figure 2.2 Schematic of the time evolution of photoexcitation and subsequent decay of localized surface plasmon resonance. (a) The excitation of a localized surface plasmon redirects the flow of light (Poynting vector) towards and into the nanoparticle. (b) In the first 1–100 fs, LSPR decays either radiatively to remit photon, or non-radiatively through Landau damping to generate hot electron-hole pairs. During this very short time interval τ_{nth} , the hot carrier distribution is highly non-thermal. (c) The hot carriers will redistribute their energy by electron-electron scattering processes on a timescale τ_{el} ranging from 100 fs to 1 ps to achieve a quasi-Fermi-Dirac distribution. (d) Finally, heat transfers to the surroundings of the metallic structure on a longer timescale τ_{ph} ranging from 100 ps to 10 ns, via thermal conduction. ¹⁵ 12

Figure 2.3 (a) Schematic of energy transfer from photo-excited plasmon to surface adsorbed species. The excited plasmon states interact through an electron transferring process with unpopulated adsorbate states. (b) Schematic of the desorption induced by electronic transitions mechanism for a dissociation reaction on a photoexcited plasmonic metal. (1) The adsorbate initially sits at the equilibrium position on its ground-state potential energy surface, requiring activation energy E_a to dissociate. (2) Photoexcitation of the plasmonic nanoparticle deposits plasmon energy into the adsorbate and elevates it to an excited potential energy surface. The adsorbate then moves

along the excited potential energy surface, gaining kinetic energy and possibly reacting in the excited state. (3) If the adsorbate does not react in the excited state, it decays back down to the ground-state potential energy surface in a vibrationally excited state effectively lowering the barrier for dissociation. (c) The efficiency of the transferring processes for inducing a catalytic reaction depends on E_a , the thermal population of adsorbate vibrational states, the magnitude of the difference between the equilibrium positions of the neutral and TNI potential energy surfaces, the slope of the TNI potential energy surface (PES) and the lifetime of the TNI state τ . a&c, ref. 21; b, ref. 35..... 15

Figure 3.1 Characterization of 1% Au/SiO₂. (a,b) High-resolution transmission electron microscopy (HR-TEM) images of Au NPs supported on SiO₂ matrix. (c) Size statistics of Au NPs. (d) UV-Vis extinction spectrum of Au/SiO₂ measured by UV-Vis diffused reflectance spectroscopy.⁴⁰ 20

Figure 3.2 Schematics of home-built photocatalysis setup in Halas group..... 22

Figure 3.3 Photocatalytic H₂-D₂ exchange reaction on 1% Au/SiO₂. (a) Real-time detection of HD formation rate with laser excitation (2.4 W/cm², on) and without (0.0 W/cm², off) laser excitation. (b) A comparison of the HD formation rate using 1% Au/SiO₂ (red) and sole SiO₂ matrix (cyan) at the same experimental conditions and laser intensities (2.4W/cm²), inset showing the baseline of HD formation. No photocatalytic rate was observed with pristine SiO₂. (c) The rate of formation of HD as a function of laser intensity using 1% Au/SiO₂ kept at a fixed temperature of 100 °C. Linear intensity dependence is observed.⁴⁵ 24

Figure 3.4 Photothermal effect of laser excitation on 1% Au/SiO₂. (a) Comparison of photocatalysis under 2.4 W/cm² laser excitation at room temperature and thermocatalysis at 100 °C in the dark. Other experiment conditions, including flow rate and pressure, are the same. (b) The calculated local temperature increase of individual Au NP as functions of NP size and laser intensity.⁴⁵ 26

Figure 3.5 Wavelength dependence of photocatalytic H₂-D₂ exchange on 1% Au/SiO₂. (a) The rate of HD formation at 100 °C as a function of band-pass filter wavelengths each adjusted to an intensity of 260 mW/cm² using 1% Au/SiO₂. Error bars were calculated as the standard deviation of the instrumental fluctuations in rate measurements using the quadrupole mass spectrometer. (b) Simulated absorption cross-section spectrum of Au/SiO photocatalyst sample modeled as 10 nm AuNP 75% embedded into a 40 nm

SiO₂ NP. It features a dipole mode located at 590 nm. The inset shows the local field enhancement $|E/E_0|^2$.⁴⁵28

Figure 3.6 Characterization of Al NCs and 5% Al NCs supported on γ -Al₂O₃. (a) Transmission electron microscope (TEM) image of Al NCs. (b) High-resolution TEM (HRTEM) image of a portion of an individual Al NC. The crystalline surface of the Al NC and the native amorphous aluminum oxide layer are resolved. (c) Size distribution of Al NCs. (d) UV-Vis-NIR extinction spectrum of Al NCs in isopropanol. A plasmonic dipolar resonance at ~ 460 nm and interband transition at ~ 800 nm manifest as a peak and a shoulder, respectively. (e) TEM image of Al NCs supported on γ -Al₂O₃. Al NCs are highlighted by red circles. (f) UV-Vis-NIR diffuse reflectance spectrum of Al NCs supported on γ -Al₂O₃. The plasmonic dipolar resonance blueshifts due to the change of the dielectric environment, while the interband absorption is shown as a dip in the reflectance spectrum.⁶.....31

Figure 3.7 Photocatalytic H₂-D₂ exchange reaction on 5% Al NCs supported on γ -Al₂O₃. (a) Real-time measurement of HD formation rate with (4 kW/cm²) and without laser excitation. Dashed blue lines represent the moments when laser light was turned on and off. (b) Comparison of photocatalytic HD formation rate of 5% Al NCs supported on γ -Al₂O₃ (red) with pure γ -Al₂O₃ matrix (black) under 4 kW/cm² laser illumination. (c) HD production (red circles) on photocatalyst illuminated by monochromatic light as a function of excitation wavelength. The error bars represent the standard deviation of multiple measurements. The calculated absorption cross-section of a single Al NC surrounded by a porous 100 nm thick γ -Al₂O₃ shell is shown as a blue curve. (d) Power dependence of HD formation rate using 800 nm (red squares) and 461 nm (blue circles) light as excitation sources. Red and blue lines are linear fits of experimental data. ⁶.....33

Figure 3.8 Photothermal effect and thermocatalytic H₂-D₂ exchange reaction on 5% Al NCs supported on γ -Al₂O₃. (a) Comparison of photocatalytic reaction rate under 300 mW white light illumination (grey shadow) with a thermocatalytic reaction rate at 50 °C in the dark (red shadow). (b) Temperature dependence of thermocatalytic HD formation rate. (c) Wavelength- and intensity-dependence of instantaneous temperature increase of a single 100 nm Al NC excited a laser pulse.⁶.....36

Figure 4.1 Electron microscopy measurement of supported Cu NPs on MgO-Al₂O₃ composite. (a) HR-TEM image of a Cu NP embedded in a MgO

nanomatrix. (b-c) HAADF-STEM images of Cu NPs supported on MgO-Al₂O₃ composite. (d) Size distribution of Cu NPs..... 42

Figure 4.2 (a) Powder X-ray diffraction spectrum of supported Cu NPs. (b) X-ray photoelectron spectrum of supported Cu NPs. The BE of Cu 3p and the absence of shake-up satellite peaks indicate the metallic state of Cu NPs..... 43

Figure 4.3 Optical property of supported Cu NPs. (a) The absorption spectrum of Cu/MgO-Al₂O₃ derived from UV-Vis diffused reflectance spectrum. (b) Calculated absorption cross-section spectrum of a single Cu NP embedded in an effective dielectric environment using FDTD simulation. (C) Calculated absorption fraction spectrum of Cu NPs ensemble using Monte Carlo simulation. (d) Comparison of the normalized experimental absorption spectrum with normalized simulated absorption spectra by Mie theory and Monte Carlo simulation, respectively 44

Figure 4.4 (a) Photocatalytic H₂-D₂ exchange reaction on Cu/MgO-Al₂O₃ and controlled experiments. (b) Intensity dependence of photocatalytic H₂-D₂ exchange reaction on Cu/MgO-Al₂O₃..... 47

Figure 4.5 Instantaneous photothermal effect of laser pulse excitation. (a) Schematics of the local temporal temperature of copper nanoparticles under illumination of periodic pulses. (b-d) Contour map of the calculated instantaneous, local temperature increase of (b) 3 nm, (c) 5 nm and (d) 10 nm Cu NP. ¹⁶ 49

Figure 4.6 Quantification of photothermal effect. (a) The 3D temperature distribution of catalyst pellet under 16.2 W/cm² while light illumination without external heating. (b) Comparison of experimentally measured surface temperature with simulated surface temperature. (c) Temperature dependence of thermocatalytic reaction rate. The Dash straight line is the Arrhenius fitting. (d) The calculated photothermal HD formation rate in photocatalysis. 51

Figure 4.7 (a) Intensity dependence of hot-carrier-mediated chemical reaction. (b) Intensity dependence of contribution of hot-carrier-mediated chemical reaction and photothermal effect in photocatalysis..... 54

Figure 4.8 Theoretical calculation of generation of thermalized hot carriers (a) quasi-Fermi-Dirac distribution of thermalized hot carriers with color shadows indicating the integration ranges for different thresholds of hot carrier

transferring. (b) Calculated input energy dependence of quantum yield of thermalized hot carriers generation..... 56

Figure 5.1 Transmission electron microscope (TEM) images and size statistics of supported metal NPs. (a) HR-TEM image of a single Ru-on-Cu surface alloy NP. (b) HAADF image of Ru-on-Cu surface alloy NPs on MgO-Al₂O₃ support. (c) Size distribution of Ru-on-Cu surface alloy NPs. (d,e) HAADF images of Cu NPs on MgO-Al₂O₃ support. (f) Size distribution of Cu NPs. (g,h) HAADF images of Ru NPs on MgO-Al₂O₃ support. (i) Size distribution of Ru NPs. ¹⁶ 64

Figure 5.2 Other characterizations of Ru-on-Cu surface alloy NPs and Cu and Ru NPs. (a) Powder X-ray diffraction (PXRD) spectrum of supported Cu-Ru surface alloy NPs. The standard PXRD data of Cu, Ru, MgO, and Al₂O₃ from International Centre for Diffraction Data (ICDD) were plotted for reference. (b) X-ray photoelectron spectra of Ru 3p_{3/2} peaks for (top panel) supported Ru NPs (Ru_{0.5}) and (bottom panel) supported Cu-Ru surface alloy NPs (Cu_{19.5}Ru_{0.5}). The chemical shift of Ru 3p_{3/2} in Cu_{19.5}Ru_{0.5} to higher energy compared to that in Ru_{0.5} indicates electron transfer from Ru to Cu. (c) N₂O chemisorption spectra of 50 mg supported Cu-Ru surface alloy NPs (blue), and 50 mg supported Cu NPs (red) at 313 K. Solid lines represent the N₂ formation rates, while dash lines show the total released N₂ by integrating the formation rate of N₂ over time. (d) UV-Vis diffuse reflectance spectra of supported Cu-Ru surface alloy NPs (solid line), Cu NPs (dashed line) and Ru NPs (short-dashed line).¹⁶ 66

Figure 5.3 Catalytic measurement of ammonia decomposition reaction. (a) The H₂ formation rate of photocatalysis (9.6 W/cm²) and thermocatalysis (482 °C) on supported Cu-Ru surface alloy, Cu NPs, and Ru NPs (b) Multiple-hour measurement of photocatalytic ammonia decomposition on Cu_{19.5}Ru_{0.5} surface alloy NPs under 9.6 W/cm² white light illumination without external heating. (c) Comparison of photocatalytic and thermocatalytic reaction rates on supported Cu-Ru surface alloy. The x-axis values of photocatalysis data points correspond to the highest surface temperature of the photocatalyst due to light-..... 70

Figure 5.4 Photocatalytic behavior of supported Cu-Ru surface alloy NPs. (a) Intensity dependence of reaction rate and energy efficiency under white light illumination. Feeding rate of NH₃ was 5 sccm for the intensity range of 1.6-3.2 W/cm² and 100 sccm for 4-9.6 W/cm². (b) Wavelength dependence of reaction rate and energy efficiency. The intensity was kept 3.2 W/cm² for all the wavelengths. Feeding rate of NH₃ was 5 sccm.¹⁶ 72

Figure 5.5 Light-dependent activation barrier and reaction order of ammonia. (a) Arrhenius plots of apparent activation barriers for different wavelengths under the constant intensity of 3.2 W/cm^2 (upper panel) and various light intensities at 550 nm (bottom panel). The black line represents thermocatalysis in the dark. (b) A 3D contour map of activation barrier for different wavelengths and intensities through interpolation of 46 data points. (c) Reaction order with respect to PNH_3 in photocatalysis (6.4 W/cm^2 white light) and thermocatalysis (427°C). r denotes the H_2 production rate while n represents the reaction order.¹⁶ 75

Figure 5.6 Mechanisms for hot-carrier-mediated reduction of activation barrier. (A) Schematic energetics of elementary reaction steps for NH_3 decomposition. The \ddagger denotes transition state, and the two relevant RDSs, N-H bond scission and associative desorption of N_2 , are labeled. N^* refers to excited Ru-N surface species: either vibronic levels in an excited electronic state (red dashed arrow and box) or vibrational excitations in the electronic ground state (red solid arrow and box). The activation barriers after excitation (red, yellow, and blue dotted lines) are all lower than that of the ground state (black dotted line). The Franck-Condon diagram inset illustrates the mechanisms in more detail. Dark red and yellow dashed arrows denote possible hot carrier transfer into or electronic excitation of the Ru-N surface species. Blue solid arrows denote multiple vibrational excitations of the electronic ground state. e^- , electron; h^+ , hole. (B) Schematics of surface coverage under heating versus light-illumination conditions. In contrast to thermocatalysis (left), photocatalysis and hot carrier generation (right) can promote desorption of “poisoning” adsorbed intermediates. $h\nu$, light.¹⁶..... 79

Figure 6.1 HAADF images and size distribution of (a,b) Cu_{20} NPs, (c,d) $\text{Cu}_{19.9}\text{Ru}_{0.1}$ surface alloy NPs, (e,f) $\text{Cu}_{19.8}\text{Ru}_{0.2}$ surface alloy NPs (g,h) $\text{Cu}_{19.5}\text{Ru}_{0.5}$ surface alloy NPs. 85

Figure 6.2 Representative N_2O dissociative chemisorption spectra of (a) Cu_{20} , (b) $\text{Cu}_{19.9}\text{Ru}_{0.1}$, (c) $\text{Cu}_{19.8}\text{Ru}_{0.2}$ and (d) $\text{Cu}_{19.5}\text{Ru}_{0.5}$. Desorbing N_2 is the measured reaction product. Note differences in scale of vertical axes. 85

Figure 6.3 UV-Vis diffuse reflectance spectra of CuRu surface alloy samples. Reflectance was transformed to absorption through Kubelka-Munk transformation¹⁰², $FR = (1 - R_\infty) / 2R_\infty$ 87

Figure 6.4 Effect of ruthenium loading on the photocatalytic behavior of Ru-on-Cu surface alloy NPs. (a) Reaction rate and long-term stability as a function

of Ru loading of the photocatalyst nanoparticles. (b) Selectivity of photocatalytic MDR reaction under $19.2 \text{ W}\cdot\text{cm}^{-2}$ white light illumination. The reactor was kept at room temperature, and selectivity is defined as the ratio of the formation rate of H_2 to CO 88

Figure 6.5 Raman spectra at the spot of light illumination before (black lines) and after (red lines) 2h photocatalysis under $19.2 \text{ W}\cdot\text{cm}^{-2}$ white light illumination for samples of (A) Cu_{20} , (B) $\text{Cu}_{19.95}\text{Ru}_{0.05}$, (C) $\text{Cu}_{19.9}\text{Ru}_{0.1}$, (D) $\text{Cu}_{19.8}\text{Ru}_{0.2}$ and (E) $\text{Cu}_{19.5}\text{Ru}_{0.5}$ 90

Figure 6.6 (a-b) HR-TEM images, (c-d) HAADF images and (e) size distribution of Cu NPs in Cu_{20} sample after 2h photocatalysis under $19.2 \text{ W}/\text{cm}^2$ while-light illumination. 92

Figure 6.7. (a) DFT calculation for C diffusion away from Ru. Pathway for C diffusion away from Ru onto a Cu_3 fcc-hollow site via a Cu-Cu bridge-site transition state. Red arrows point to the diffusing C. Corresponding MEPs is shown in the right panel with the barriers marked. (b) Schematics of the compositional dependence of the Cu_xRu_y photocatalysts with respect to coke resistance. 93

Figure 6.8 Photo- and thermo-catalytic characterization of the $\text{Cu}_{19.8}\text{Ru}_{0.2}$ catalyst for methane dry reforming. (a) Long-term stability (filled circles) and selectivity (open circles) for photocatalysis under $19.2 \text{ W}\cdot\text{cm}^{-2}$ white light illumination (blue circles) and thermocatalysis at 1000 K reactor temperature (red circles). (b) Light intensity dependence of reaction rate and selectivity in photocatalysis. Error bars represent the standard deviation (σ_{std}) of measurements of three different batches of the sample. (c) Light intensity dependence of the highest surface temperature (T_{hs}) on sample pellet. (d) Temperature dependence of reaction rate and selectivity in thermocatalysis. Error bars represent the σ_{std} of measurements of two different batches of sample. 96

Figure 6.9 Photocatalytic energy efficiency and the methane conversion of $\text{Cu}_{19.8}\text{Ru}_{0.2}$. (a) Light-to-chemical energy efficiency of photocatalysis as a function of white light intensity. (b) Methane conversion by photocatalysis (blue and olive) and thermocatalysis (red and orange) as a function of space velocity, defined as the volumetric flow rate of the reactants divided the mass of the catalyst. Error bars represent the σ_{std} of measurements of two different batches of the sample. 98

Figure 6.10 Arrhenius fitting of thermocatalytic MDR and RWGS reactions on Cu_{19.8}Ru_{0.2}.....	104
--	------------

List of Tables

Table 6.1 N₂O chemisorption experiment results	86
Table 6.2 Element concentration determined from ICP-MS	86
Table 6.3 Calculated selectivity of thermocatalysis based on data from NIST database¹⁰⁶	97

List of Equations

Equation 3.1 Local temperature increase due to plasmonic heating	25
Equation 3.2 instantaneous temperature increase of a single Al NC.....	38
Equation 4.1 rate equation of thermocatalytic H ₂ -D ₂ exchange reaction	50
Equation 5.1 Turnover frequency of H ₂ production rate.....	68
Equation 5.2 Energy efficiency of photocatalytic NH ₃ decomposition	68
Equation 5.3 Quantum yield of photocatalytic NH ₃ decomposition.....	68

Nomenclature

AR	Antenna-reactor
DIET	Desorption induced by electronic transitions
DIMET	Desorption induced by multiple electronic transitions
DMR	Dry methane reforming
DRS	Diffused reflectance spectroscopy
HR-TEM	High-resolution transmission electron microscopy
HAADF-STEM	High-angle annular dark-field scan transmission electron microscopy
ICP-MS	Inductively coupled plasma mass spectroscopy
LSPR	Localized surface plasmon resonance
MS	Mass spectroscopy
NCs	Nanocrystals
NIR	Near-infrared
NPs	Nanoparticles
PXRD	Powder X-ray diffraction
RWGS	Reversed water gas shift
UV	Ultraviolet
Vis	Visible
XPS	X-ray photoelectron spectroscopy

Chapter 1

Introduction

Over the past decay, plasmonic photocatalysis based on metal nanoparticles has attracted tremendous interest in photocatalysis community due to its capability in driving chemical reactions with light under milder conditions than conventional thermocatalysis¹. This achievement is mainly attributed to the high optical cross-section of plasmonic nanoparticles, resulted from the unique collective oscillation of free electrons in metal nanoparticles under the excitation of the alternating electromagnetic field in light, known as localized surface plasmon resonance (LSPR). The strong coupling between light and plasmonic nanoparticles provides the energy channel needed for the light-to-chemicals conversion. Various plasmonically active metals, such as Au²⁻³, Ag⁴, Cu⁵, and Al⁶ have been demonstrated as effective photocatalysts for a series of catalytic reactions. For example, plasmonics has been shown experimentally and theoretically to facilitate H₂-D₂ exchange⁷⁻⁹, CO₂ reduction¹⁰⁻¹¹, selective oxidation⁵ and N₂ activation¹²⁻¹³. Compared to semiconductor photocatalysts, several characters are

2

unique to plasmonic photocatalysts¹⁴: (1) they exhibit super-linear intensity dependence under specific conditions; (2) thermal excitation is synergetic to light excitation and high temperature is beneficial to plasmonic photocatalysis. These features make plasmonic photocatalysis extremely attractive in energy application since the photocatalytic efficiency could increase dramatically with light intensity and temperature.

The hot-carrier-mediated chemical transformation is generally accepted as the main mechanism in plasmonic photocatalysis¹⁵. Upon excited by light on plasmonic nanoparticles, the localized surface plasmon resonance will decay, either re-emits a photon out through radiative decay or generates a hot carrier with energy above the Fermi level through non-radiative decay. When there are adsorbates on the surface of plasmonic nanoparticles with frontier orbitals of chemical bond(s) appropriately aligning in energy, hot electrons/holes could weaken the chemical bond(s) through electronic excitation by transferring to its LUMO/HOMO orbitals, facilitating bond breaking and chemical reactions. Hot carriers can also excite the chemical bonds through electron-vibrational scattering¹⁶. This mechanism releases the requirement of energy resonance between hot carriers and the molecular orbitals. Moreover, multiple excitations of vibrational levels are feasible. Finally, the photothermal effect, which resulted from electron-phonon interaction, could also contribute to photocatalysis by heating the metal nanoparticles and driving catalytic reaction through conventional thermocatalysis.

3

Unfortunately, most of the plasmonically active metals, mainly including Au, Ag, Al and Cu, exhibit weak catalytic activity compared to the noble metals. This severely limits the full employment of hot carriers in catalytic reaction and hinder the breakthrough in the performance of plasmonic photocatalysts. Very recently, people propose the antenna-reactor structure, which combines plasmonically active metal “antenna” nanoparticles with catalytically active “reactor” materials. The antenna-reactor concept has been demonstrated to be successful in improving the photocatalytic performance^{12-13, 17-20}, in several cases. It is clear that the performance of antenna-reactor complexes depends on the structure and the way that they are combined. A new type of antenna-reactor structure, surface alloy, will be discussed in this thesis.

In chapter 2, I will introduce the properties of localized surface plasmon resonance and its decay process, especially the non-radiative decay path, which generates hot carriers and cause the photothermal effect. Two forms of hot carriers and the photothermal effect are the central concepts to explain various phenomena. The mechanism of hot-carrier-mediated chemical reaction will be subsequently discussed. This chapter mainly serves as the knowledge preparation for understanding the following cases of plasmonic photocatalysis in this thesis.

Two plasmonic photocatalysts, Au nanoparticles and Al nanocrystals, will be investigated for light-induced H₂ dissociation in Chapter 3. They exhibit similar intensity dependence and are proposed to be driven by the same initial hot carriers. The results demonstrated the capability of the hot carrier in activating elementary

4

surface reaction with high barriers and its advantage over the traditional phonon-excited process.

Another monometallic plasmonic photocatalyst, Cu nanoparticles, will be studied in chapter 4 for photocatalyzing the same H₂-D₂ exchange reaction. The photothermal effect observed in plasmonic Cu NPs is not negligible and a method for quantifying the photothermal effect by combining experimental measurement and theoretical simulation will be developed to extract out the contribution of hot-carrier-mediated mechanism. The obtained intensity dependence of hot-carrier-mediated reaction rate exhibits very different behaviors compared to that of Au- and Al-based plasmonic photocatalysts. Hot carrier multiplication is proposed to explain the observation and will be demonstrated with a theoretical model.

Ru-on-Cu surface alloy will be introduced in chapter 5 as a promising antenna-reactor structure. It exhibits excellent activity towards ammonia decomposition reaction, a promising reaction for hydrogen storage application. The effect of hot-carrier activation on the apparent activation barrier will be explored comprehensively, covering a wide range of intensity and wavelength conditions. The mechanism of light-dependent activation barrier will be discussed.

In chapter 6, the surface alloy structure will be further developed to achieve single-atom-alloy structure. This structure effectively depresses the coke formation in methane activation under light excitation, exhibiting high stability in photocatalytic methane dry reforming reaction. Supported by the controlled thermocatalytic experiments and quantum mechanics calculation, both the single-atom structure and

hot-carrier-mediated mechanism are demonstrated to be essential for coke-resistant merit.

This thesis is based on my following coauthored papers:

- (1) Shaunak Mukherjee, Linan Zhou, Amanda M. Goodman, Nicholas Large, Ciceron Ayala-Orozco, Yu Zhang, Peter Nordlander, Naomi J. Halas. "Hot-Electron-Induced Dissociation of H₂ on Gold Nanoparticles Supported on SiO₂." *J. Am. Chem. Soc.* **2014**, 136, 64-67.
- (2) Linan Zhou, Chao Zhang, Michael J. McClain, Alejandro Manjavacas, Caroline M. Krauter, Shu Tian, Felix Berg, Henry O. Everitt, Emily A. Carter, Peter Nordlander, Naomi J. Halas. "Aluminum Nanocrystal as a Plasmonic Photocatalyst for Hydrogen Dissociation." *Nano Lett.* **2016**, 16, 1478-1484.
- (3) Linan Zhou, Dayne F. Swearer, Chao Zhang, Hossein Robotjazi, Hangqi Zhao, Luke Henderson, Liangliang Dong, Phillip Christopher, Emily A. Carter, Peter Nordlander, Naomi J. Halas. "Quantifying hot carrier and thermal contributions in plasmonic photocatalysis." *Science.* **2018**, 362, 69-72.
- (4) Linan Zhou, John Mark P. Martirez, Chao Zhang, Dayne F. Swearer, Shu Tian, Hossein Robotjazi, Luke Henderson, Emily A. Carter, Peter Nordlander, Naomi J. Halas. "Light-driven methane dry reforming with single atomic site antenna-reactor plasmonic photocatalysts." Submitted
- (5) Linan Zhou, Minhan Lou, Jun G. Liu, Chao Zhang, Dayne F. Swearer, Nathaniel J. Hogan, Hossein Robotjazi, Shu Tian, Liangliang Dong, Peter Nordlander,

6

Naomi J. Halas. "Demonstration of hot carrier multiplication in plasmonic photocatalysis." under preparation

Chapter 2

Plasmon decay and hot-carrier-mediated chemical processes

2.1. Localized surface plasmon resonance

Unique in the metallic nanoparticles, the conduction free electrons could collectively oscillate driven by the alternative electromagnetic waves in light, leading to the so-called localized surface plasmon resonance when the wavelength of the light resonant with the natural frequency of the oscillating electrons against the restoring force of the metal ion core (Figure 2.1a). The excitation of LSPR manifests itself with an extinction peak in the UV-Vis extinction spectrum of plasmonic nanomaterials (Figure 2.1b). The resonant wavelength of plasmonic nanostructures vary with materials²¹ (Figure 2.1c), size²¹⁻²² and shape²¹⁻²² of metallic nanostructures (Figure 2.1c), dielectric environment²² and the coupling between plasmonic nanoparticles²³.

It is feasible to design nanostructures that strongly interact with a specific portion of the electromagnetic spectrum, or even the entire solar spectrum, by designing and engineering the compositions and structures of plasmonic nanomaterials²³.

Excitation of LSPR of a plasmonic nanoparticle will manipulate and concentrate the light within a space larger than its physical volume into a small volume near the surface of the nanoparticle, creating an intense electromagnetic field at nanometer scale surrounding the nanoparticle²⁴. The enhancements of the electric fields (E/E_0) could achieve 10-100 times on the surface of isolated nanoparticles or 10^3 times in the hot spot of two closed nanoparticles with nanogap²⁵. The capability of plasmonic nanomaterials to strongly couple with light enable them to transduce light energy to other energy forms, including but not limited to electricity, chemical and heat, efficiently and be applied in various applications such as photovoltaic cell²⁶, photocatalysis¹ and photothermal heating²⁷.

Theoretically speaking, all the materials containing enough free electrons can support LSPR, but only specific metals exhibit strong LSPR in the UV-Vis ranges owing to their specific electronic structures supporting ideal free electrons with suitable electron density and low damping effect²⁸. Among them, Au, Ag, Al and Cu are the most investigated plasmonic materials in the visible range due to their relatively stable chemical property. Other good plasmonic materials, like the alkali metals, are less frequently studied as they are too reactive to be practical in plasmonic

application. While d-block transition metals generally show strong interband transition across the whole UV-Vis region, highly damping the LSPR.

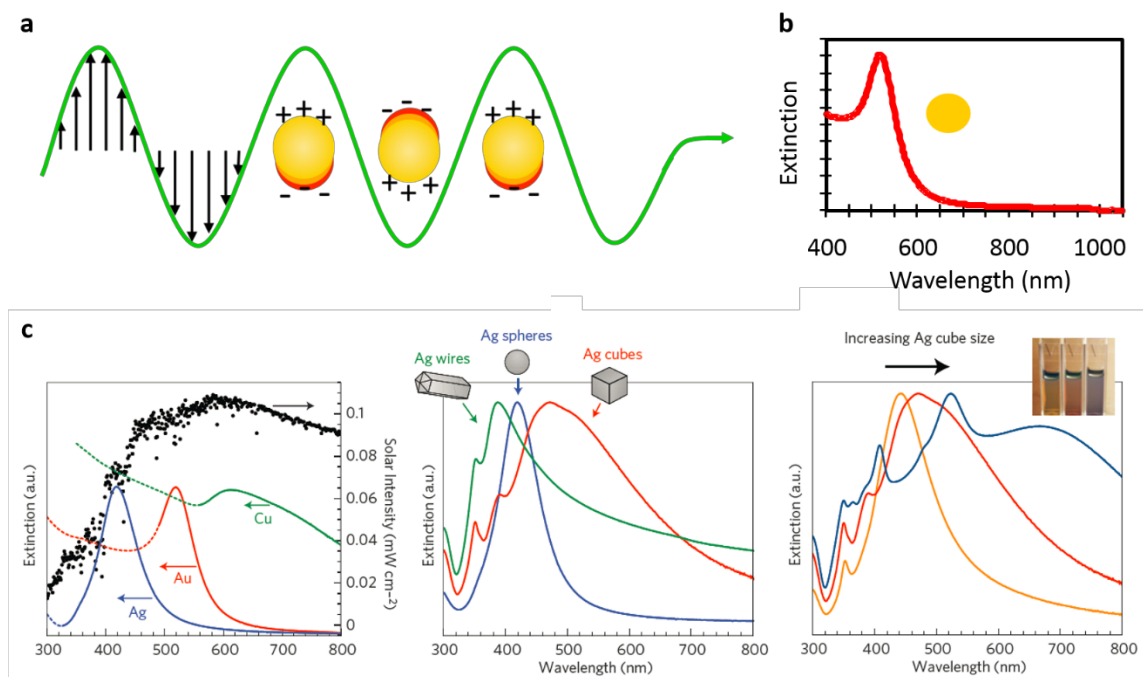


Figure 2.1 (a) Schematics of excitation of LSPR in plasmonic metal nanoparticles by the electromagnetic wave of light. (b) Representative UV-Vis extinction spectrum of a gold NPs solution. (c) Left panel: Normalized extinction spectra of spherical Ag (38 ± 12 nm diameter), Au (25 ± 5 nm) and Cu (133 ± 23 nm) particles. The metal extinction is a consequence of the excitation of surface plasmon resonance. Dashed portions of the metal extinction curves indicate interband transitions; Middle panel: Normalized extinction spectra for Ag wire, cube and sphere nanoparticles. Wire-shaped particles are 90 ± 12 nm diameter and >30 aspect ratio, cubic particles are 79 ± 12 nm edge length and spherical particles are 38 ± 12 nm diameter; right panel: Normalized extinction spectra for Ag nanocubes as a function of size (56 ± 8 nm, 79 ± 13 nm and 129 ± 7 nm edge lengths correspond to orange, red and blue spectra respectively). The

inset shows a photograph of the three nanocube samples suspended in ethanol.

21

2.2. Plasmon decay

Once excited (Figure 2.2a), within 1-100 fs, plasmon resonances in the plasmonic nanostructures can be damped radiatively by re-emitting a photon out or non-radiatively into generating hot electron-hole pairs (hot carriers), which are essential in the application of plasmonic nanomaterials as photocatalysts, through Landau damping (Figure 2.2b)²⁹. The branching ratio of these two decay paths depends on the size, composition and surface modification²⁰ of the plasmonic nanostructures, and the plasmonic mode and excitation wavelength³⁰. In the non-radiative decay, excited hot carriers lying above the Fermi level are generated by energy transfer from a plasmon quantum to a single electron below Fermi level through the interaction between the conduction electrons and the oscillating plasmon-induced electric field and form a non-thermal distribution. One factor affecting the distribution of hot carriers is the excitation wavelength, or correspondingly the plasmon energy. For plasmon energy below the interband transition, intraband transition dominates and hot electrons will lay high above the Fermi level while hot holes locate just below the Fermi level. On the other hand, for plasmon energy above the interband transition, hot electrons mainly distribute just above the Fermi level while hot holes locate deep under the Fermi level³¹.

Soon later, these initial hot electrons will quickly redistribute their energy to unexcited electrons through electron-electron scattering processes with a time scale of 100 fs to 1 ps³². This hot carrier multiplication generates many more hot electrons with lower energy and reaches a quasi-Fermi-Dirac distribution with an effective electron temperature (T_{el}) much higher than the ambient temperature as a measurement of the energy stored in the hot carriers (Figure 2.2c). With the generation of low-energy hot carriers, the events of electron-phonon scattering increase due to the energy match between the low-energy hot carriers and phonons. This results in an equilibrium process between the hot carriers and the lattice of the plasmonic nanostructure over a time scale of a few picoseconds, which could be described through a two-temperature model³².

Finally, the phonon-phonon interaction between the lattice of the plasmonic nanoparticles and the surrounding substrate dissipates the energy to the environment in the form of heat. This process will take from 100 ps to 10 ns depending on the thermal conductivity and heat capacitor of the plasmonic materials and the environment (Figure 2.2).

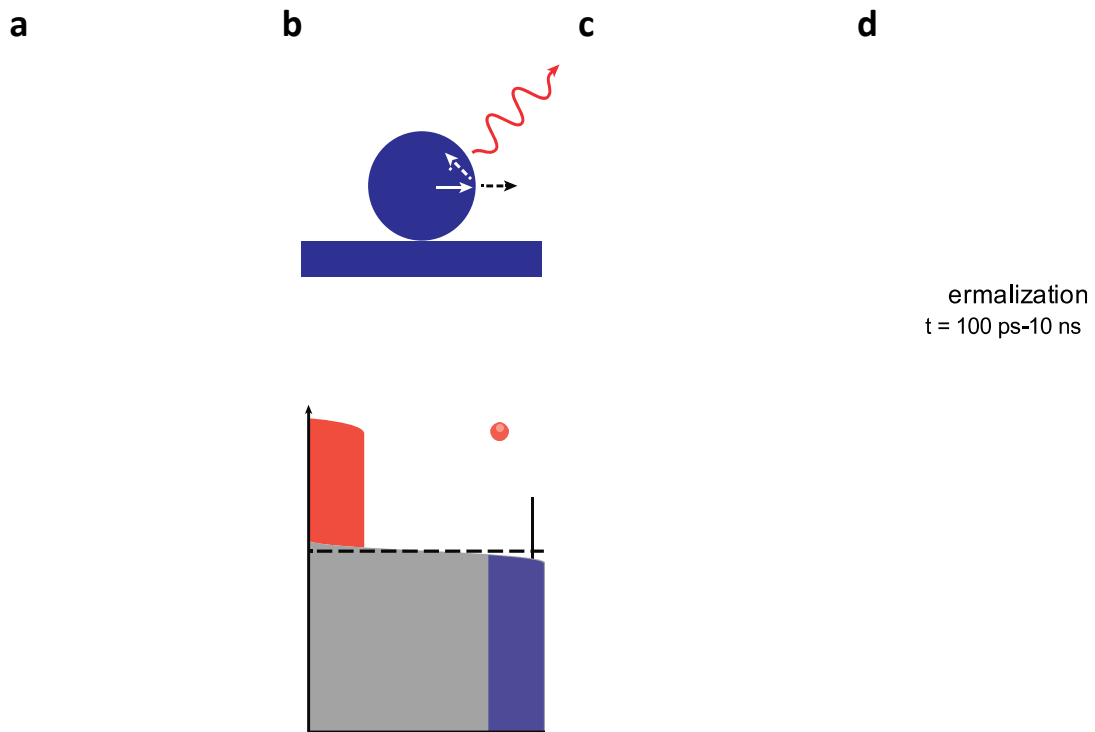


Figure 2.2 Schematic of the time evolution of photoexcitation and subsequent decay of localized surface plasmon resonance. (a) The excitation of a localized surface plasmon redirects the flow of light (Poynting vector) towards and into the nanoparticle. (b) In the first 1–100 fs, LSPR decays either radiatively to emit photon, or non-radiatively through Landau damping to generate hot electron-hole pairs. During this very short time interval τ_{nth} , the hot carrier distribution is highly non-thermal. (c) The hot carriers will redistribute their energy by electron-electron scattering processes on a timescale τ_{ei} ranging from 100 fs to 1 ps to achieve a quasi-Fermi-Dirac distribution. (d) Finally, heat transfers to the surroundings of the metallic structure on a longer timescale τ_{ph} ranging from 100 ps to 10 ns, via thermal conduction.¹⁵

2.3. Hot-carrier-mediated chemical process

As mentioned above, the hot carriers derived from plasmon decay have recently been demonstrated to be capable in molecular activation through electronic transitions, a concept developed from desorption induced by electronic transition (DIET) and desorption induced by multiple electronic transitions (DIMET) used in describing laser-induced molecule desorption from bulk metal surface³³⁻³⁴. This enables plasmonic materials function as photocatalysts for light-induced chemical transformation. When an adsorbed species with suitable empty orbitals present on the surface of plasmonic nanoparticles, hot carriers can transfer to the molecule and form the transient negative ion (TNI), providing the energy needed for bond activation and/or breaking. According to the Franck-Condon principle, due to the slower nuclear motion compared to electronic transition, the formed TNI will initially stay at the equilibrium position of the ground-state potential energy surface (PES) of the adsorbate, but forced to evolve to accommodate the PES of TNI. This molecular evolution can either directly induce bond breaking along the PES of TNI (Figure 2.3b(2)), or activate the bond vibrationally once the TNI decays back to the neutral ground state from a position other than the equilibrium position of the neutral ground state (Figure 2.3b(3)). The lifetime of the TNI are generally tens of femtoseconds while the vibrationally excited states could last several picoseconds, both of which are long-lived enough to induce chemical transformation. Models based on DIET and DIMET³³ showed that the probability for LSPR-induced hot-carrier-mediated chemical

reaction on metals depends on hot carriers distribution, the transition matrix of hot carriers to the available molecular orbitals on the adsorbate, the PES for the ground (neutral) and excited (charged) states, the lifetime of the excited state, and the initial vibrational distribution of the ground state (Figure 2.3c).

To achieve an efficient hot-carrier-driven chemical reaction, theoretically speaking, we could control the size (smaller) and shape of plasmonic nanomaterials to increase the branching ratio of non-radiative decay to generate more hot carriers, and tune the energy distribution of hot carriers to make them resonant with the available states of adsorbates. Modifying the surface with active metals could effectively lower the position of the antibonding orbital of adsorbates while creating an electronically inhomogeneous surface that facilitates the non-radiative decay of plasmon^{16, 20}. Increasing the lattice temperature also works as phonon is synergic with hot carriers in activating molecules on the metal surface, which is a unique property of plasmonic metal nanostructures compared to semiconductors^{14, 16}.

While there are tremendous researches on the mechanism of the hot-carrier-mediated chemical process, there is little discussion in distinguishing the contribution and behavior of initial hot carriers and thermalized hot carriers. Generally, initial hot carriers are believed to be more effective since they are energetic in activating molecules with antibonding orbital laying high above the Fermi level. This drive researchers to design systems with direct resonant energy transfer to absorbed molecules to avoid energy lost through e-e scattering. However, in cases

where the molecules are vibronically activated on plasmonic nanomaterials with a reactive surface, thermalized hot carriers are potentially energetic enough to drive the reaction and enhance the usage of photons through hot carrier multiplication. The comparison of initial hot carriers and thermalized hot carriers will be made combining the results of chapter 3 and 4.

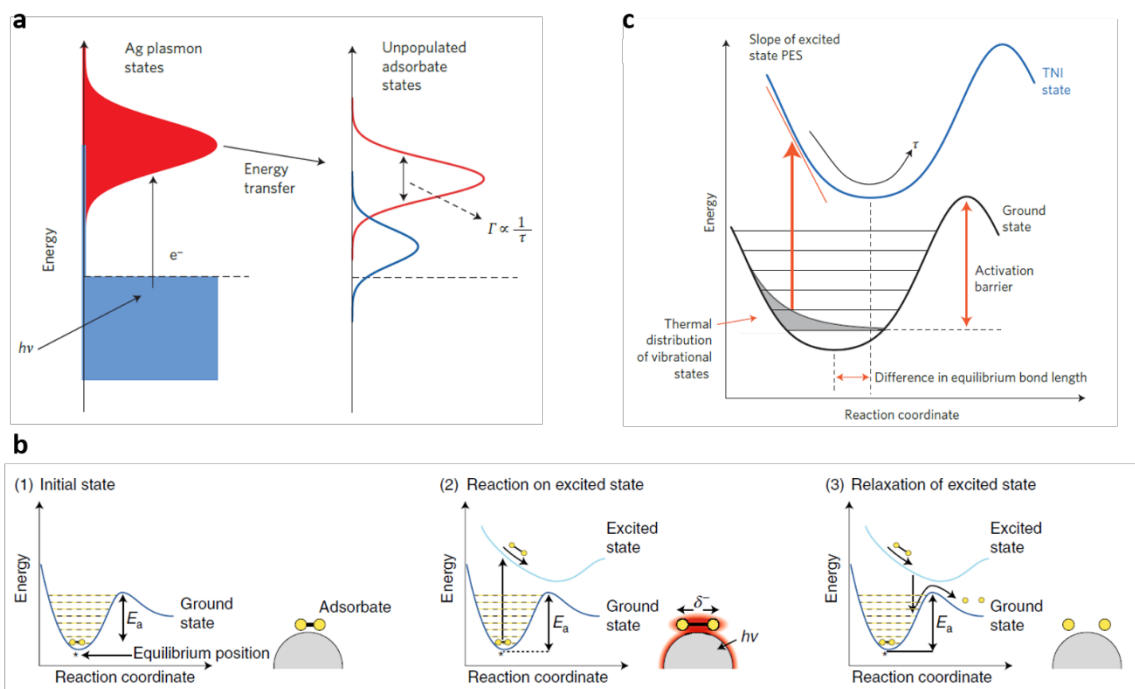


Figure 2.3 (a) Schematic of energy transfer from photo-excited plasmon to surface adsorbed species. The excited plasmon states interact through an electron transferring process with unpopulated adsorbate states. (b) Schematic of the desorption induced by electronic transitions mechanism for a dissociation reaction on a photoexcited plasmonic metal. (1) The adsorbate initially sits at the equilibrium position on its ground-state potential energy surface, requiring activation energy E_a to dissociate. (2) Photoexcitation of the

plasmonic nanoparticle deposits plasmon energy into the adsorbate and elevates it to an excited potential energy surface. The adsorbate then moves along the excited potential energy surface, gaining kinetic energy and possibly reacting in the excited state. (3) If the adsorbate does not react in the excited state, it decays back down to the ground-state potential energy surface in a vibrationally excited state effectively lowering the barrier for dissociation. (c) The efficiency of the transferring processes for inducing a catalytic reaction depends on E_a , the thermal population of adsorbate vibrational states, the magnitude of the difference between the equilibrium positions of the neutral and TNI potential energy surfaces, the slope of the TNI potential energy surface (PES) and the lifetime of the TNI state τ . a&c, ref. 21; b, ref. 35.

H₂ activation by hot carriers on plasmonic metal nanoparticles

3.1. Hydrogen activation

Hydrogenation, as one of the largest families of heterogeneous catalysis in industry, plays a crucial role in many aspects of our society. From gas & oil upgrading³⁶⁻³⁷, plastic synthesis³⁸⁻³⁹, to food treatment and drug synthesis⁴⁰, hydrogenation is indispensable in our life. H₂ activation, namely breaking of H-H bond to form active atomic H species on the catalyst surface, is an essential step in catalytic hydrogenation and attracts tremendous research in both academy and industry. Supported precious metal nanoparticles are frequently used as the catalysts for hydrogenation attributed to their excellent activity in hydrogen activation⁴¹. Despite the outstanding property of noble metals, elevated temperatures, and high pressures are generally required for most processes. This makes it desirable to find an alternative mechanism for H₂ activation under milder conditions.

3.2. Supported gold nanoparticles as a photocatalytic platform for hot-carrier-mediated H₂ dissociation

Gold is traditionally viewed as inactive for thermally activating hydrogen dissociation due to its unfavorable electronic structure. Recently, Shaunak Mukherjee *et al.* demonstrated the feasibility of H₂ activation on Au/TiO₂ photocatalyst at low temperature by photoexcited hot carriers on Au⁴². However, TiO₂ might act as a hot carrier scavenger due to the relative low Schottky barrier (0.9-1 eV) formed at the Au/TiO₂ interface and decrease the branching ratio of hot carriers in activating adsorbed molecules. Therefore, performing the H₂ dissociation reaction with Au NPs on an entirely inert dielectric support could potentially obtain higher photocatalytic efficiency. To demonstrate this idea, I designed a new gold-based plasmonic photocatalyst, Au/SiO₂, by replacing the matrix of TiO₂ with SiO₂ and investigated its performance in the photocatalytic H₂-D₂ exchange reaction

3.2.1. Synthesis and characterization of Au/SiO₂ photocatalyst

1 wt% gold nanoparticles supported on SiO₂ matrix was synthesized through deposition-precipitation (DP) method³. Briefly, 0.16 g HAuCl₄ · 3H₂O (Sigma-Aldrich) was dissolved in 100 mL water and added to a 500 mL round bottom flask containing 1 g SiO₂ nanopowder (Sigma Aldrich) that has been dried and activated at 100 °C

overnight. The slurry was heated to 80 °C under stirring in the dark while the pH of the solution was adjusted to ~9 by adding 1 M NaOH dropwise. The slurry was further stirred for another 2 h at 80 °C before cooled down and exhaustively washed with water and centrifuged at 3800 rpm to obtain a brown precipitation. The solid was dried at 100 °C overnight and further annealed at 300 °C for 2 h.

The size of gold NPs spans from 5 nm to 30 nm (Figure 3.1c), with an average diameter of ~11 nm, as observed by transmission electron microscopy (TEM) (Figure 3.1a-b). Optical measurement by UV-Vis diffused reflectance spectroscopy revealed a dipolar LSPR peak at around 520 nm (Figure 3.1d).

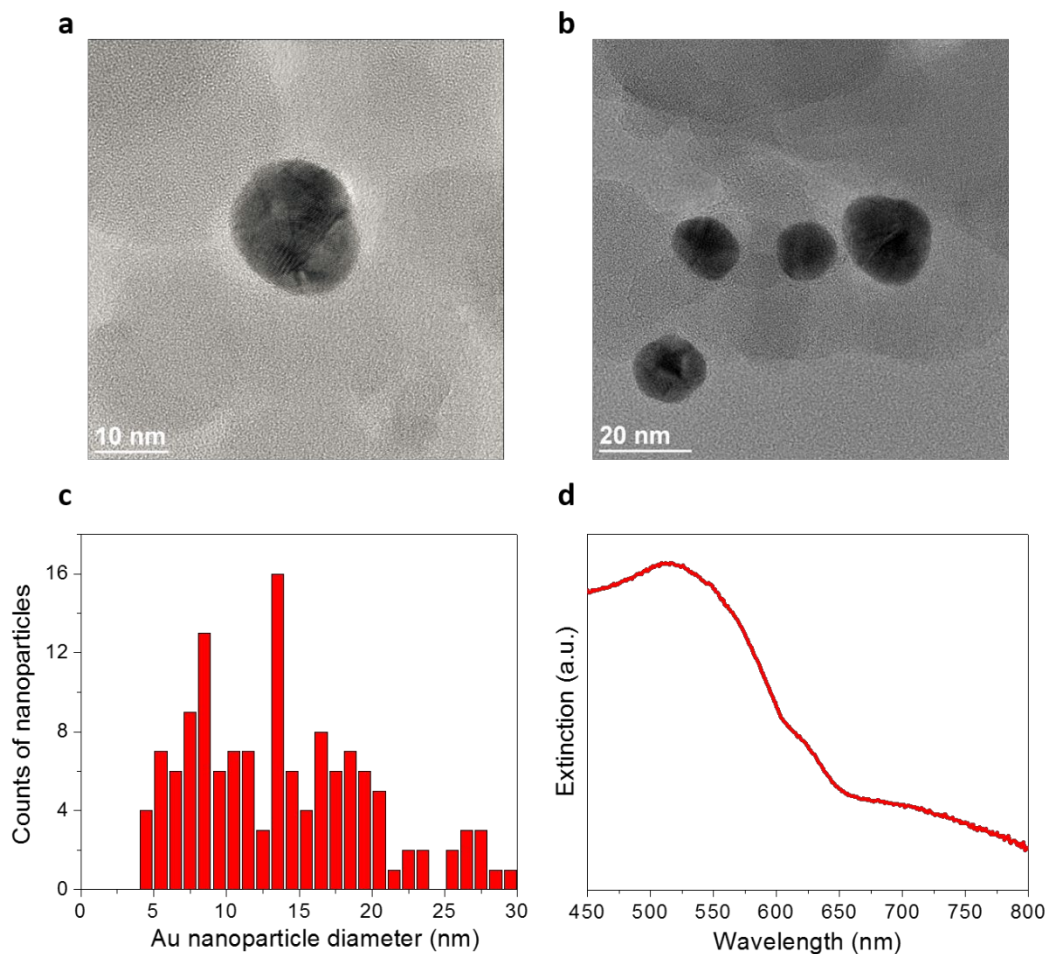


Figure 3.1 Characterization of 1% Au/SiO₂. (a,b) High-resolution transmission electron microscopy (HR-TEM) images of Au NPs supported on SiO₂ matrix. (c) Size statistics of Au NPs. (d) UV-Vis extinction spectrum of Au/SiO₂ measured by UV-Vis diffused reflectance spectroscopy.⁴⁰

3.2.2. Photocatalytic H₂-D₂ exchange reaction on Au/SiO₂

Unless otherwise stated, the photocatalytic H₂-D₂ exchange reaction was performed at ambient condition (room temperature and 1 atmospheric pressure) in a home-

built photocatalysis reaction system (Figure 3.2)⁴². In a typical photocatalytic experiment, highly pure gases from gas tanks are fed into the reaction chamber, which has a CaF₂ window for white-light excitation (laser spectrum of SC-400-4 is shown on the left for example) and IR thermal imaging (an IR image is shown on the right for example). The chamber can be externally heated by a temperature controller. Effluents can be detected by the mass spectrometer and/or gas chromatograph. Around 10 mg of supported gold NPs were loaded into a Harrick high-temperature reaction chamber. 10 sccm H₂ and 10 sccm D₂ gases (Matheson, research purity) flew as the feed reactants and the effluents were monitored by Hiden quadrupole mass spectrometry ($m/z = 2$ for H₂, 3 for HD and 4 for D₂) in real time. White light from a supercontinuum laser source (Fianium, SC-450-2) was used to excite the plasmon of Au nanoparticles over a range of intensities and wavelengths. Before laser excitation, a low-level, steady-state HD background level was observed, mostly due to HD impurity present in the H₂ and D₂ gases. The feed gases were flown into the chamber in the dark for around 20 min to get a steady HD background before starting the experiment.

The HD formation rate with and without the white light excitation on the Au/SiO₂ is shown in Figure 3.3a. Upon laser excitation with the intensity of 2.4 W/cm², the signal of HD increases instantaneously, reaching 2×10^6 counts/s of mass spec signal, which corresponding to ~ 0.77 $\mu\text{mol/s}$ HD formation rate after calibration. As soon as the laser was switched off, the HD signal decreased back the initial signal immediately, showing reversibility of the process. This process is

repeatable and the signal is the same for each run of laser excitation, demonstrating the stability of photocatalysis in this system. Control experiments were performed using pure SiO₂ matrix and the zero signal suggests that the observed HD formation in the Au/SiO₂ originates from the photocatalytic activity of plasmonic Au NPs.

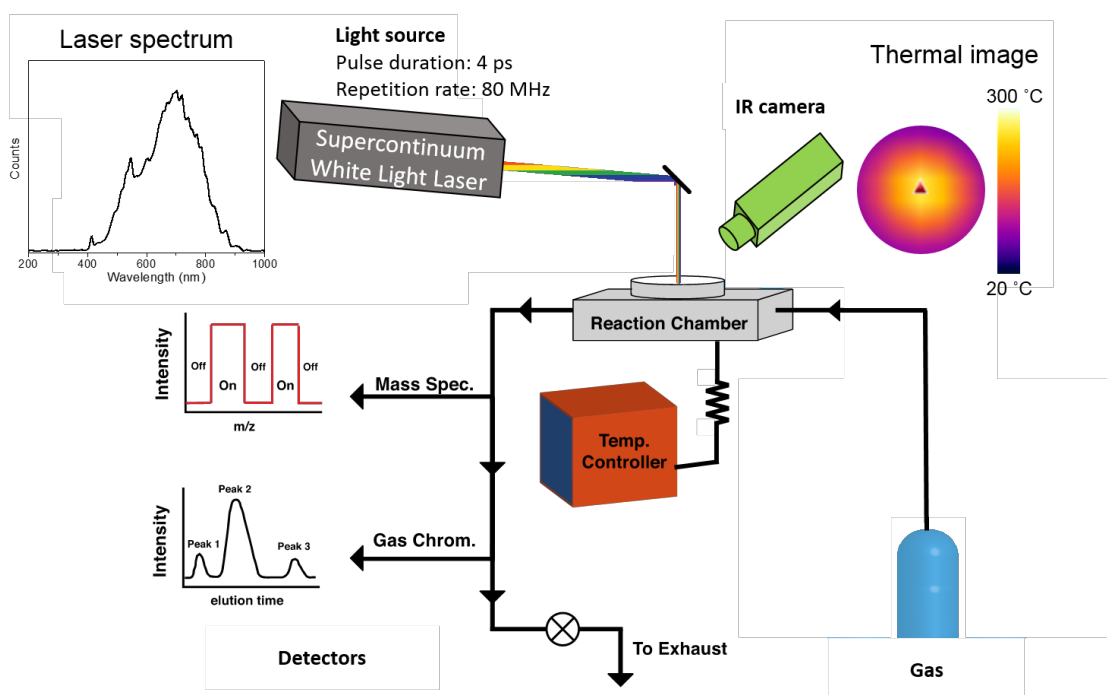


Figure 3.2 Schematics of home-built photocatalysis setup in Halas group.

We noticed that the photocatalytic HD formation rate of 1% Au/SiO₂ is two orders of magnitude higher than that of 1% Au/TiO₂ we reported previously⁴². The low at the interface of Au-TiO₂ metal-semiconductor junction (0.8 - 1 eV)⁴³ is responsible for the much lower rate obtained for Au/TiO₂ photocatalyst. The hot

electrons with energies greater than the barrier can transfer from the Au NP to the TiO₂, resulting in a substantial reduction of the number of hot electrons available to the physisorbed H₂ to excite H₂ dissociation. However, in case of Au/SiO₂, there is a much higher barrier between the Au-SiO₂ metal-insulator junction, and thus more hot electrons derived from plasmon decay on the surface of Au NPs can contribute the chemical process.

The intensity dependence of the HD formation rate was also investigated for 1% Au/SiO₂ at a constant temperature of 100 °C, as shown in Figure 3.3c. We observed a linear dependence of the photocatalytic rate on excitation laser intensity, which supports our understanding that the rate of photocatalysis is dominated by conversion of a single photon to a single hot electron which initiates a single H₂ dissociation event. This suggests that the initial hot carriers play the dominated role here, probably because it requires hot carriers with high energy (> 1eV) to excite the H₂ dissociation on Au surface⁴⁴.

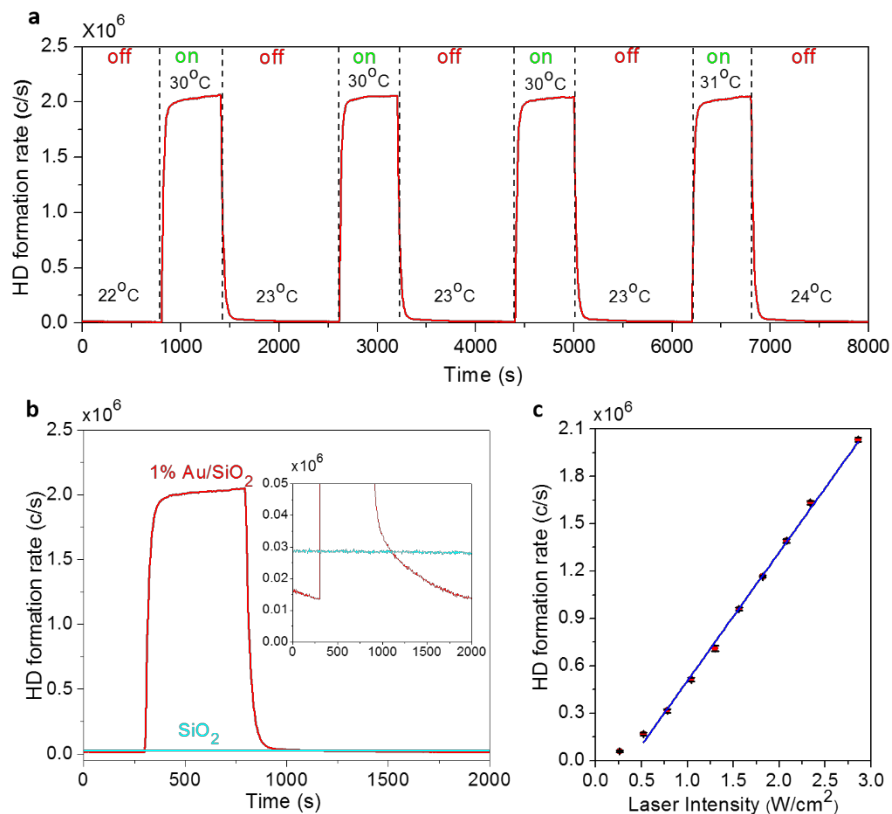


Figure 3.3 Photocatalytic H₂-D₂ exchange reaction on 1% Au/SiO₂. (a) Real-time detection of HD formation rate with laser excitation (2.4 W/cm², on) and without (0.0 W/cm², off) laser excitation. (b) A comparison of the HD formation rate using 1% Au/SiO₂ (red) and sole SiO₂ matrix (cyan) at the same experimental conditions and laser intensities (2.4W/cm²), inset showing the baseline of HD formation. No photocatalytic rate was observed with pristine SiO₂. (c) The rate of formation of HD as a function of laser intensity using 1% Au/SiO₂ kept at a fixed temperature of 100 °C. Linear intensity dependence is observed.⁴⁵

To confirm that the observed photocatalytic activity was not due to laser heating, we first performed the thermocatalytic H₂-D₂ exchange using 1% Au/SiO₂ as the controlled experiment. As shown in Figure 3.4a, even under 100 °C, the signal of

HD was only $\sim 5 \cdot 10^4$ counts/s, far way lower than the signal obtained under 2.4 W/cm² laser excitation.

To consider the local photothermal effect, we further applied a plasmonic heating model^{42, 46-48} to calculate the local temperature increase of individual gold nanoparticle under pulsed laser excitation. Isolated Au NPs were simulated as being 75% embedded inside a SiO₂ matrix. The local change in temperature on the Au NP due to plasmonic heating can be expressed as

$$\Delta T = \frac{\sigma_{\text{abs}} I}{4\pi R \beta \kappa_m}$$

Equation 3.1 Local temperature increase due to plasmonic heating

where σ_{abs} is the effective absorption cross-section of a single Au NP embedded in a SiO₂ matrix by integrating the product of absorption cross-section spectrum of a single Au NP with the laser spectrum, I is the laser intensity, R is the radius of the spherical Au nanoparticle, β is the thermal capacitance coefficient depending on the nanoparticle aspect ratio ($\beta = 1$ for a spherical nanoparticle), and κ_m denotes the temperature-dependent thermal conductivity of the surrounding dielectric (SiO₂)⁴⁹, respectively. The absorption cross-section spectra of a single spherical Au NP embedded in a SiO₂ matrix for Au NP sizes ranging from 5 nm to 30 nm were calculated using Finite-Difference Time-Domain (FDTD) simulation with dielectric functions of Au and SiO₂ from Johnson & Christy⁴⁸ and Palik⁵⁰ data,

respectively. The maximal local temperature increase was only 1.5 K, corresponding to 2.5W/cm² laser excitation and 5 nm Au NP (Figure 3.4b). This confirms that photothermal heating barely contributes to the observed photocatalytic activity.

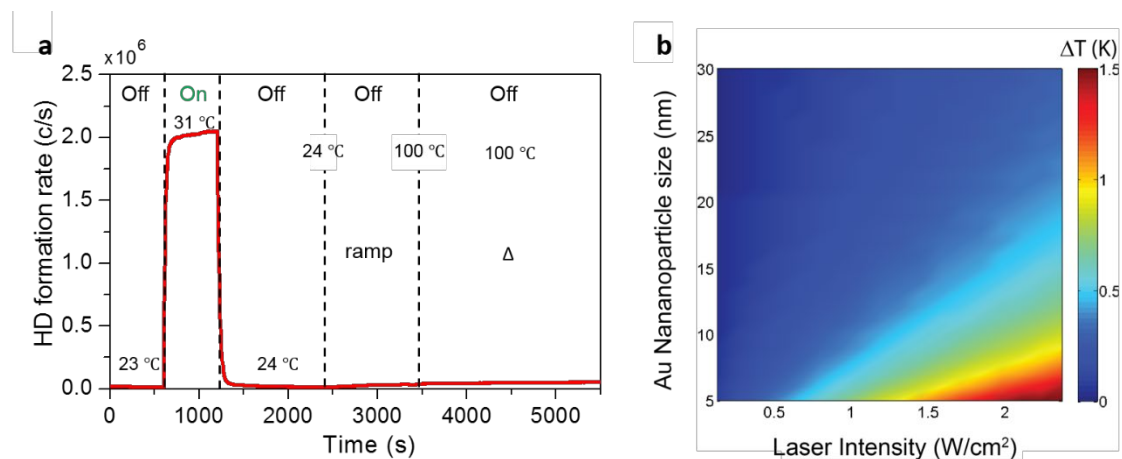


Figure 3.4 Photothermal effect of laser excitation on 1% Au/SiO₂. (a) Comparison of photocatalysis under 2.4 W/cm² laser excitation at room temperature and thermocatalysis at 100 °C in the dark. Other experiment conditions, including flow rate and pressure, are the same. (b) The calculated local temperature increase of individual Au NP as functions of NP size and laser intensity.⁴⁵

The wavelength dependence of photocatalytic H₂-D₂ exchange reaction on 1% Au/SiO₂ photocatalyst was performed at 100°C chamber temperature to minimize thermal fluctuations due to laser heating. Bandpass filters (Edmund Optics, Interference filters) with a bandwidth of 40 nm were used to obtain monochromatic lights from 450-800 nm with central wavelengths separated by 25 nm. The impinged intensity of each monochromatic light on sample pellet was adjusted to 130 mW/cm².

The wavelength dependence of HD formation exhibits a peak at ~ 590 nm (Figure 3.5a), in contrast to the experimentally measured diffuse reflectance spectrum which has a peak at 525 nm (Figure 3.1d). This is proposed to be attributable to the reduction of SiO_2 to Si-O(H)-Si during the H_2 activation, and the concomitant increase in refractive index from 1.5 (SiO_2) to 2.2-2.5 (Si-O(H)-Si)⁵¹. After H_2/D_2 is photocatalytically dissociated on the Au NPs' surface, the atomic H/D species could diffuse onto the oxide support by spillover mechanism⁵²⁻⁵⁴, resulting in the reduction of SiO_2 to SiO:H ⁵⁵⁻⁵⁷. The substantial increase in the refractive index of the environment of Au NPs could further cause the large redshift of the absorption spectrum of Au/SiO in-situ.

FDTD simulation was performed with a 10 nm Au NP 75% embedded by volume inside a 40 nm SiO nanoparticle with a refractive index of 2.5⁵⁸. The calculated absorption spectrum (Figure 3.5b) exhibits a dipolar LSPR at 590 nm, in agreement with the peak observed in the HD formation rate spectrum (Figure 3.5a). A near-field enhancement ($|E/E_0|^2$) contour plot is also shown as an inset, to illustrate the field distribution of the LSPR and to display the geometry used in the simulations.

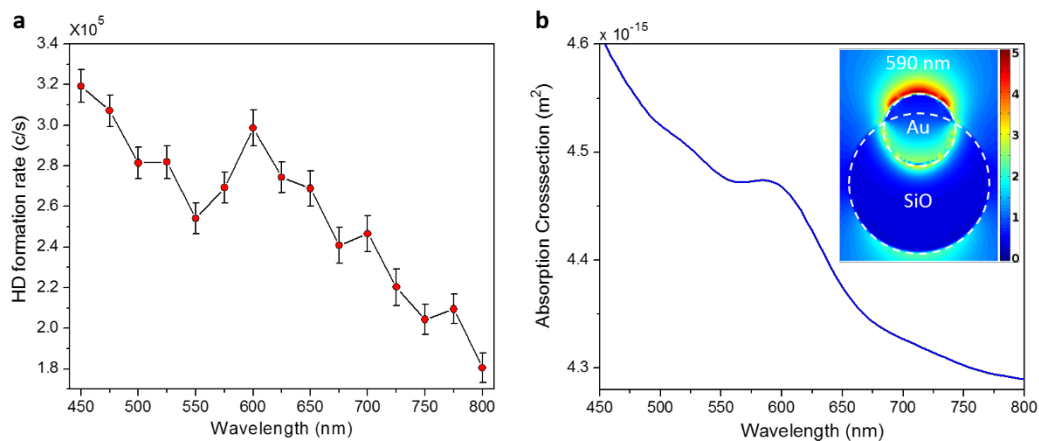


Figure 3.5 Wavelength dependence of photocatalytic H₂-D₂ exchange on 1% Au/SiO₂. (a) The rate of HD formation at 100 °C as a function of band-pass filter wavelengths each adjusted to an intensity of 260 mW/cm² using 1% Au/SiO₂. Error bars were calculated as the standard deviation of the instrumental fluctuations in rate measurements using the quadrupole mass spectrometer. (b) Simulated absorption cross-section spectrum of Au/SiO photocatalyst sample modeled as 10 nm AuNP 75% embedded into a 40 nm SiO₂ NP. It features a dipole mode located at 590 nm. The inset shows the local field enhancement $|E/E_0|^2$.⁴⁵

3.3. Plasmonic aluminum nanocrystals for photocatalytic H₂ dissociation

The high cost of gold might hinder its wide application in large-scale reaction. Aluminum, as the most abundant metallic element in the Earth's crust and ten thousand times cheaper than precious metals, has been shown to support strong LSPR spanning from visible to ultraviolet wavelength regions⁵⁹⁻⁶⁰. However, direct photocatalysis with Al nanostructures is less explored due to its unfavorable

electronic band structure and thus poor affinity for molecules⁶¹⁻⁶². Therefore exploring Al nanostructure as plasmonic photocatalysis is desirable and could open the possibility of widespread application of plasmonic photocatalysis in practical production. Here I investigated the Aluminum nanocrystal as a potential plasmonic photocatalyst for H₂ activation.

3.3.1. Synthesis and characterization of Al nanocrystals (NCs) and γ -Al₂O₃ supported Al NCs

The Al NCs were synthesized following the published protocol⁶³ with minor modification. Briefly, 12.5 mL dehydrated THF, 12.5 mL dehydrated dioxane and 6.5 mL of 0.5 M dimethyl ethyl amine alane solution in toluene were injected into a 100 mL flask connected to Schlenk line, through syringes. The whole solution was heated to 40 °C in an oil bath under stirring. Then a 0.5 mL solution of 3.3 mM titanium (IV) isopropoxide in toluene was added as a catalyst to trigger the nucleation and growth of Al nanocrystals. The solution became brown color immediately and then changed to grey-green gradually. After 2 hrs, the reaction was quenched by adding 0.5 – 1 mL oleyl acid. The solution was washed with 30 mL toluene twice and 30 mL IPA 3 times. The Al NCs were obtained by centrifuging at 1000 – 4000 rpm between each washing.

The photocatalyst sample was prepared as a 5 wt% Al NCs dispersed on a commercial γ -Al₂O₃ support (Alfa) to avoid aggregation in the photocatalytic experiment. In a 100mL conical flask containing ~ 95 mg γ - Al₂O₃ support, a 50 mL IPA dispersion with ~ 5 mg Al NCs was added. The solution was stirred overnight and

then centrifuged at 3000 rpm for 10 min to collect the solid sample. The solid sample was vacuum dried at room temperature overnight and grounded to a fine powder for photocatalytic measurements.

The Al NCs used in our experiments were around 100 nm in diameter (Figure 3.6a) with a 3 nm native oxide layer (Figure 3.6b). This photocatalyst supports a dipolar plasmon mode at around 461 nm (Figure 4.6c), as determined by the UV-Vis-NIR extinction spectra of Al NCs dispersed in IPA. A shoulder at ~ 800 nm is attributed to the interband transition of Al⁵⁹. After deposited Al NCs onto γ -Al₂O₃, as confirmed by TEM (Figure 3.6e), the dipolar LSPR peak of Al NCs/ γ -Al₂O₃ blue shifts to 446 nm due to the decrease of effective dielectric constant (Figure 3.6f). Although γ -Al₂O₃ ($\epsilon \sim 1.768$) has a higher refractive index than IPA ($n \sim 1.377$), the majority volume of Al NCs was immersed in the gas phase, which has dielectric constant close to 1. The interband transition was manifested as a dip in diffuse reflectance spectra due to its absorptive nature.

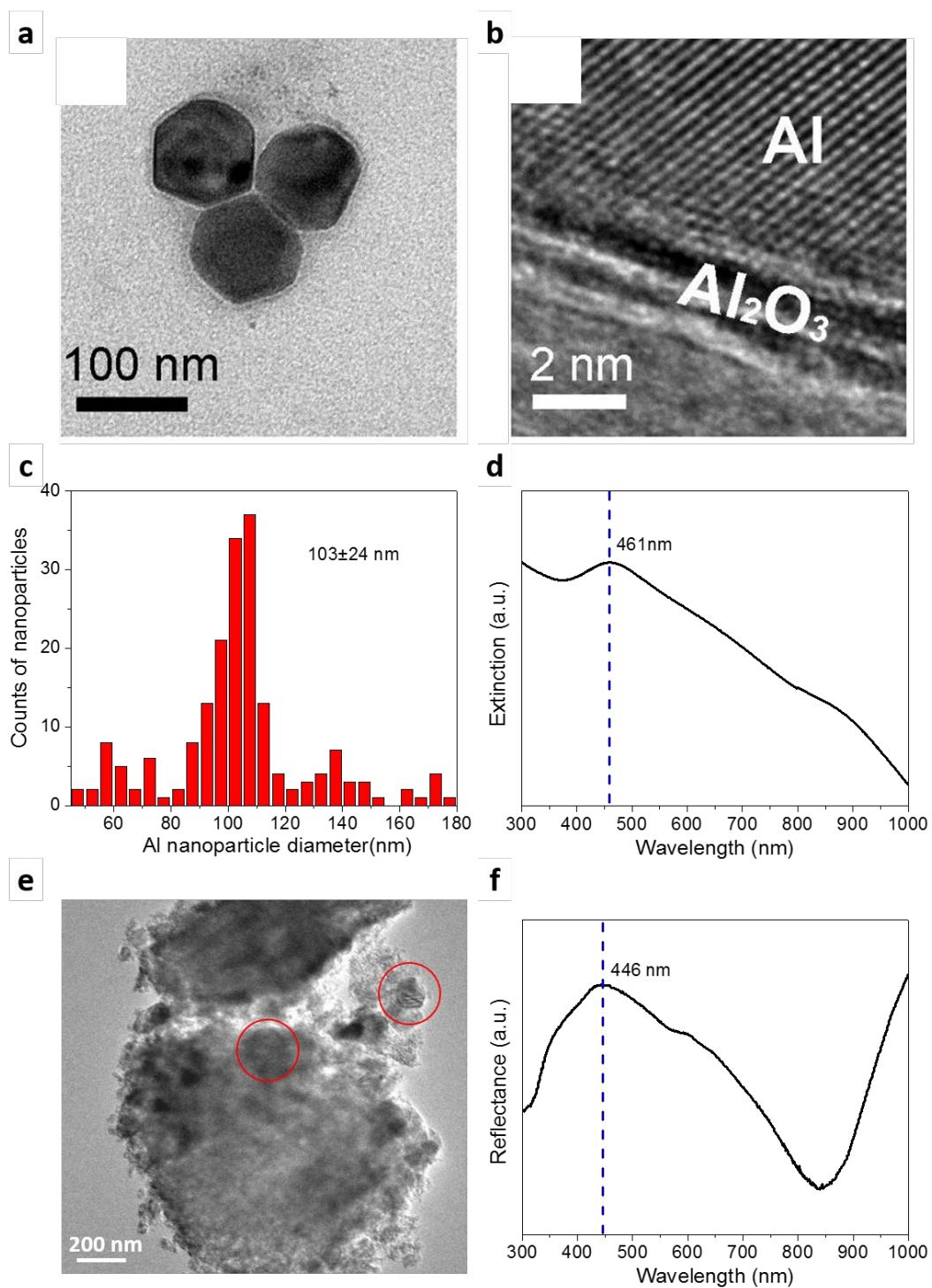


Figure 3.6 Characterization of Al NCs and 5% Al NCs supported on γ -Al₂O₃. (a) Transmission electron microscope (TEM) image of Al NCs. (b) High-resolution

TEM (HRTEM) image of a portion of an individual Al NC. The crystalline surface of the Al NC and the native amorphous aluminum oxide layer are resolved. (c) Size distribution of Al NCs. (d) UV-Vis-NIR extinction spectrum of Al NCs in isopropanol. A plasmonic dipolar resonance at ~ 460 nm and interband transition at ~ 800 nm manifest as a peak and a shoulder, respectively. (e) TEM image of Al NCs supported on γ -Al₂O₃. Al NCs are highlighted by red circles. (f) UV-Vis-NIR diffuse reflectance spectrum of Al NCs supported on γ -Al₂O₃. The plasmonic dipolar resonance blueshifts due to the change of the dielectric environment, while the interband absorption is shown as a dip in the reflectance spectrum.⁶

3.3.2. Photocatalytic H₂-D₂ exchange reaction on Al NCs/ γ -Al₂O₃

The Al NCs/ γ -Al₂O₃ photocatalyst was then loaded into the same photocatalysis reaction chamber as described in section 3.2.2 for H₂-D₂ exchange reaction. White light from the supercontinuum fiber laser and Hiden mass spectrometer were again used as the light source and detector, respectively. But for wavelength dependence measurements, monochromatic light from a tunable Ti:sapphire laser (Coherent, Chameleon Ultra II, 150 fs, 80 MHz, 680–1080 nm, bandwidth ~10 nm) equipped with a second harmonic generator (Angewandte Physik und Elektronik GmbH, output wavelength 350–530 nm) was used. The chamber was kept at room temperature for the photocatalytic experiment. Upon white-light laser excitation, the HD rate increased to $\sim 1.5 \times 10^5$ counts/s within 5 min (Figure 3.7a). After the laser was turned off, the HD rate dropped back to the initial background level. This process could be repeated multiple times with good reproducibility. The Al NCs were demonstrated to be the active component of

photocatalytic H₂ dissociation, as the pure γ -Al₂O₃ showed no activity under the same illumination condition (Figure 3.7b, black line).

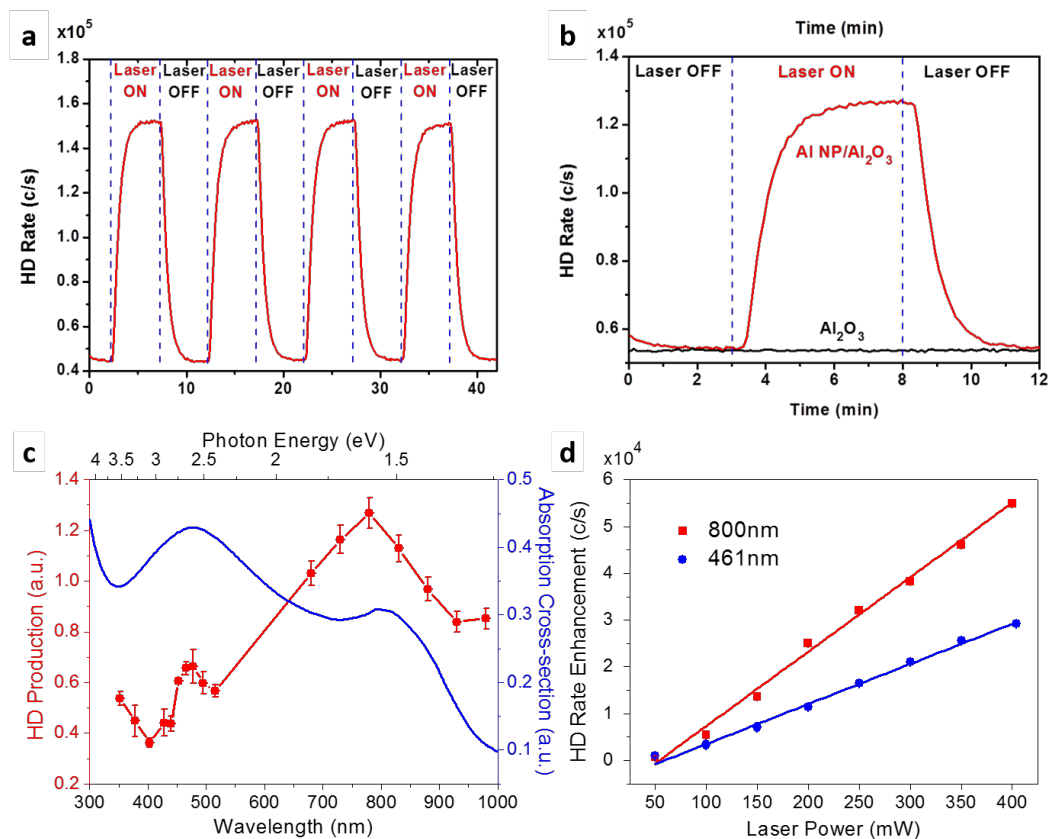


Figure 3.7 Photocatalytic H₂-D₂ exchange reaction on 5% Al NCs supported on γ -Al₂O₃. **(a)** Real-time measurement of HD formation rate with (4 kW/cm²) and without laser excitation. Dashed blue lines represent the moments when laser light was turned on and off. **(b)** Comparison of photocatalytic HD formation rate of 5% Al NCs supported on γ -Al₂O₃ (red) with pure γ -Al₂O₃ matrix (black) under 4 kW/cm² laser illumination. **(c)** HD production (red circles) on photocatalyst illuminated by monochromatic light as a function of excitation wavelength. The error bars represent the standard deviation of multiple measurements. The calculated absorption cross-section of a single Al NC surrounded by a porous 100 nm thick γ -Al₂O₃ shell is shown as a blue curve. **(d)** Power dependence of

HD formation rate using 800 nm (red squares) and 461 nm (blue circles) light as excitation sources. Red and blue lines are linear fits of experimental data. ⁶

To better understand the light-induced catalytic response, I measured the photocatalytic rate under excitations of different wavelengths with 65 mW power. Due to the low power of monochromatic light, I performed the photocatalysis using static mode⁶ to achieve better signal/noise ratio. The amount of HD produced exhibits a small peak at around 460 nm (Figure 3.7c), corresponding to the dipolar LSPR mode of the Al NCs where hot electrons are generated through the plasmon decay. However, maximum HD formation rate is observed at around 800 nm, which corresponds to the interband transitions in Al. Hot electrons are produced by direct photon-excited electron transitions from filled to unfilled sp-derived bands of Al, which has a band edge of ~ 1 -1.5 eV above the Fermi level^{31, 64}. The absorption cross section of a 100 nm Al NC was calculated using Mie theory for comparison (Figure 3.7c, blue curve). The absorption peaks around 460 and 800 nm are the dipolar LSPR and Al interband transition, respectively. Although the absorption cross-section at interband transition is smaller than the LSPR region, the hot carriers derived from interband transition are more effective given that more HD produced under light excitation at interband transition wavelength. Recent work on hot-carrier-mediated processes indicates that the energy alignment of a metal nanostructure with an adsorbed molecule⁶⁵ or a semiconductor⁶⁶ interface is crucial in determining the efficacy of different processes. In Al, the interband transition yields hot electrons with energies

1–1.5 eV above the Fermi level, which are energetic enough to transfer to the antibonding orbital of the absorbed H₂ and facilitate dissociation.

The intensity dependence of the HD formation rate was measured at 800 nm (interband transition) and 461 nm (LSPR). We observed a linear dependence on the excitation power at both wavelengths, for power densities up to 4 kW/cm² (Figure 3.7d), indicating that the hydrogen dissociation reaction studied here is triggered by a single hot electron for both LSPR and interband transition excitations, as in the case of Au/SiO₂.

During the photoreaction, we noticed that the temperature of the photocatalyst increased slightly (<5 K) due to laser-induced heating. To evaluate the photothermal effect in the observed photocatalytic activity, I compared the purely thermocatalytic rate with the light-induced reaction rate. As shown in Figure 3.8a, the HD generation rate by heating at 50 °C in the dark was less than 3% of the photocatalytic rate under 300 mW while light illumination of the catalyst. Even at a temperature as high as 127 °C, the thermocatalytic HD formation rate is only around 2×10^4 counts/s (Figure 3.8b). We also calculated the upper limit of instantaneous, local temperature increase of an individual Al NC induced by laser pulses as a function of time-average laser intensity and wavelength through an adiabatic heating model⁶. The temperature increase was calculated as the ratio of the light energy absorbed by an Al NC (product of the laser intensity and the effective absorption cross-section of the Al NC towards our light source) to its heat capacity. The predicted temperature

increase is less than 5 K for all of our experimental conditions (Figure 3.8c). This result confirms that the observed hydrogen dissociation reaction on the photocatalyst is mainly light-triggered rather than thermally driven.

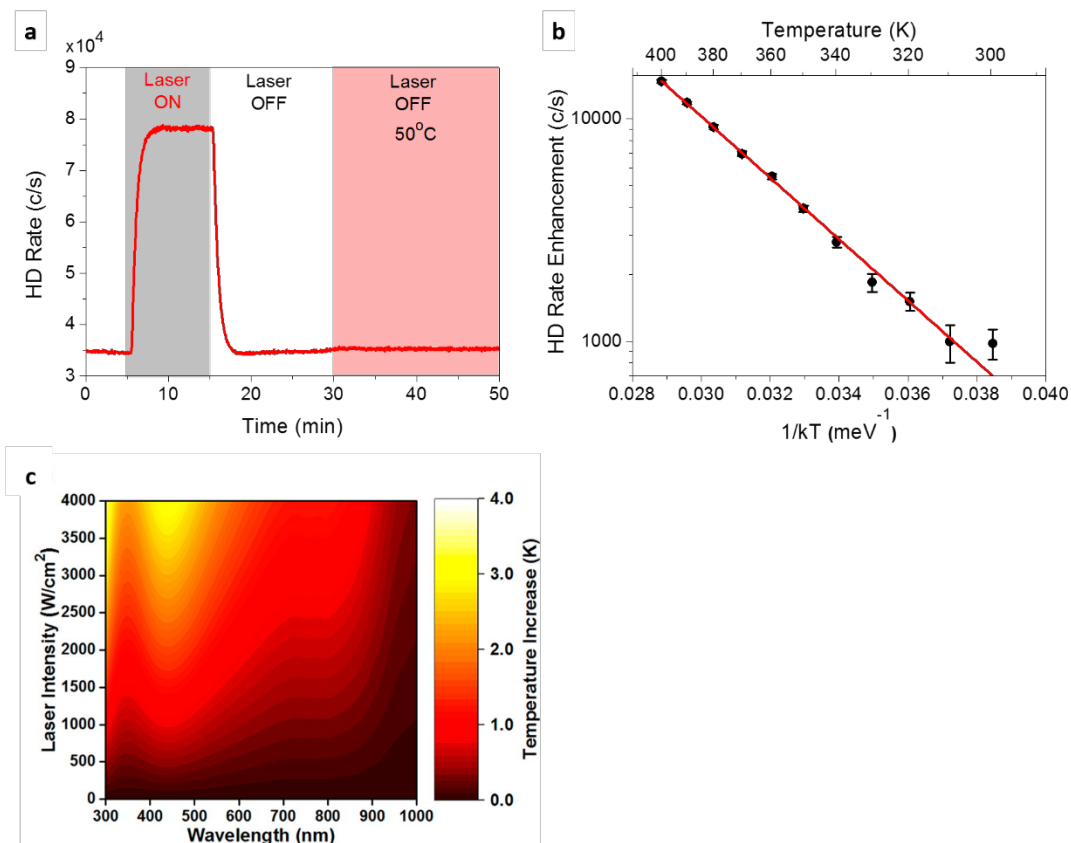


Figure 3.8 Photothermal effect and thermocatalytic H₂-D₂ exchange reaction on 5% Al NCs supported on γ -Al₂O₃. **(a)** Comparison of photocatalytic reaction rate under 300 mW white light illumination (grey shadow) with a thermocatalytic reaction rate at 50 °C in the dark (red shadow). **(b)** Temperature dependence of thermocatalytic HD formation rate. **(c)** Wavelength- and intensity-

dependence of instantaneous temperature increase of a single 100 nm Al NC excited a laser pulse.⁶

3.4. Conclusion

I have observed plasmon-induced H₂/D₂ dissociation on both of Au NPs and Al NCs, supported on SiO₂ and Al₂O₃, respectively. Both samples show a linear intensity dependence of photocatalytic H₂-D₂ exchange reaction. Transferring of initial hot carriers to the antibonding orbital of H₂ and sequent activation of H-H bond is proposed to be the mechanism for both cases. Au/SiO₂ exhibits almost 2 orders of magnitude higher efficiency than Au/TiO₂, which is compromised by the scavenge effect of TiO₂. The interband transition in Al is unique, giving energetic enough hot carriers for molecule activation due to its special electronic structure different from other d-block plasmonic metals (Cu, Ag, and Au).

Appendix A

Calculation of upper-limit of instantaneous, local temperature increase of a single Al NC by a laser pulse

We estimated the maximum temperature increase of the Al NPs when illuminated with the laser following the theory developed in ref ⁶⁷. In particular, we assumed that the electron-phonon scattering occurred much faster than the external heat diffusion and the time separation between laser pulses, which in our case was $\sim 1/80$ MHz ~ 12.5 ns. This allowed us to write the maximum temperature increase as

$$\Delta T_{max} = \frac{\sigma_{abs}}{V_{Al}\rho_{Al}c_{Al}} \frac{I}{f}$$

Equation 3.2 instantaneous temperature increase of a single Al NC

being σ_{abs} the absorption cross-section of the nanoparticle, V_{Al} the volume of the Al core, ρ_{Al} the aluminum mass density, c_{Al} the Al heat capacity, I the laser average intensity, and f the pulse repetition rate. This expression implies that all the energy is absorbed in the Al core, which is a realistic assumption, given the negligible absorption of Al_2O_3 in the spectral range under consideration.

Demonstration of hot carrier multiplication in plasmonic photocatalysis

4.1. Initial hot carriers versus thermalized hot carriers

Although the hot-carrier-mediated process has been widely accepted as an activation mechanism in plasmonic photocatalysis^{15, 68}, there is barely report that distinguish the roles of initial hot carriers and thermalized hot carriers in plasmonic photocatalysis. Thus the investigation on behaviors and features of either initial hot carriers or thermalized hot carriers in activating chemical reaction is lack. While initial hot carriers possess higher energy and are supposed to be more effective in systems having high electron transferring barrier, the number of the thermalized hot carriers is augment through the electron-electron scattering and could be more efficient in cases where low resonant electronic states are present or chemical bond is activated through electron-vibrational excitation.

Phillip Christopher *et al.* have reported a theoretical investigation on the dynamic of hot carriers and the time-dependent contribution of thermalized hot carriers on several chemical process⁶⁵, including NO and CO desorption from Pt surface and oxygen diffusion on Pt surface. The result showed that the efficiency of thermalized hot carriers is quite low for these processes, mainly due to the high energy barriers of hot carriers transferring from metal surface to the antibonding orbital of the above molecules on Pt surface. However, it does show that the efficiency of thermalized hot carriers is inversely proportional to the energy barrier of hot carrier transferring. It is possible to achieve high quantum yield with thermalized hot carriers if a system with low resonant transferring barrier is discovered. Here we show that photoinduced desorption of H₂ on Cu surface is predominately contributed by thermalized hot carriers, gaining a quantum yield exceeding 1.

4.2. Synthesis and characterization of supported copper NPs

Plasmonically active Cu nanoparticles (NPs) supported on MgO/Al₂O₃ composited support was synthesized through the constant-pH co-precipitation method followed by in-situ annealing and reduction in a photocatalytic reaction chamber, as reported in our previous work¹⁶. In details, a 15 mL aqueous solution containing 0.2 M Cu(NO₃)₂, 0.6 M Mg(NO₃)₂ and 0.2 M Al(NO₃)₃, and a 20 mL 1.2 M Na₂CO₃ aqueous solution were first prepared for sequent use. 10 mL DI water was added to a 100 mL 5-neck, round-bottom flask and heated to 80 °C. Then the metal precursor solution and Na₂CO₃ solution were added simultaneously and dropwise to the preheated water. The pH was monitored with a pH meter and kept at pH = 8 by tuning the adding speed of both solutions. The resulting solid slurry was allowed to

stir at 80 °C for 24 hours before cooling to room temperature. The catalyst precursor was isolated by centrifuging and subsequently washed 4 times with DI water and dried in the air at 100-120 °C overnight. The obtained dry precursor was packed into the high-temperature reaction chamber and annealed at 500 °C under helium atmosphere (20 sccm He) for 1h before reduced at 500 °C under 20 sccm H₂ flow for another hour. Thereafter the catalyst is denoted as Cu₂₀ since the mole ratio of Cu in the total metal elements of the catalyst (Cu, Mg, and Al) is 20%.

High-resolution transmission electron microscopy (HR-TEM, Figure 4.1a) revealed that crystalline copper nanoparticle was embedded in and directly contact with crystalline MgO, which probably were supported on amorphous Al₂O₃ together. The statistical average diameter of Cu NPs is ~ 5 nm (Figure 4.1d) from the high-angle annular dark-field scan transmission electron microscopy (HAADF-STEM) images (Figure 4.1b&c). Both copper nanoparticles and MgO are crystallized while Al₂O₃ is amorphous according to the powder X-ray diffraction (XRD) result (Figure 4.2a), consistent with the observation in HR-TEM (Figure 4.1a). X-ray photoelectron spectroscopy (XPS) revealed the oxidation state of copper as a metallic state (Figure 4.2b), confirming the success of reduction treatment in the reaction chamber.

The sample exhibits a localized surface plasmon resonance (LSPR) peak at around 560 nm (Figure 4.3a). We first performed the FDTD simulation to calculate the absorption cross-section spectrum of a single copper NP embedded in an effective

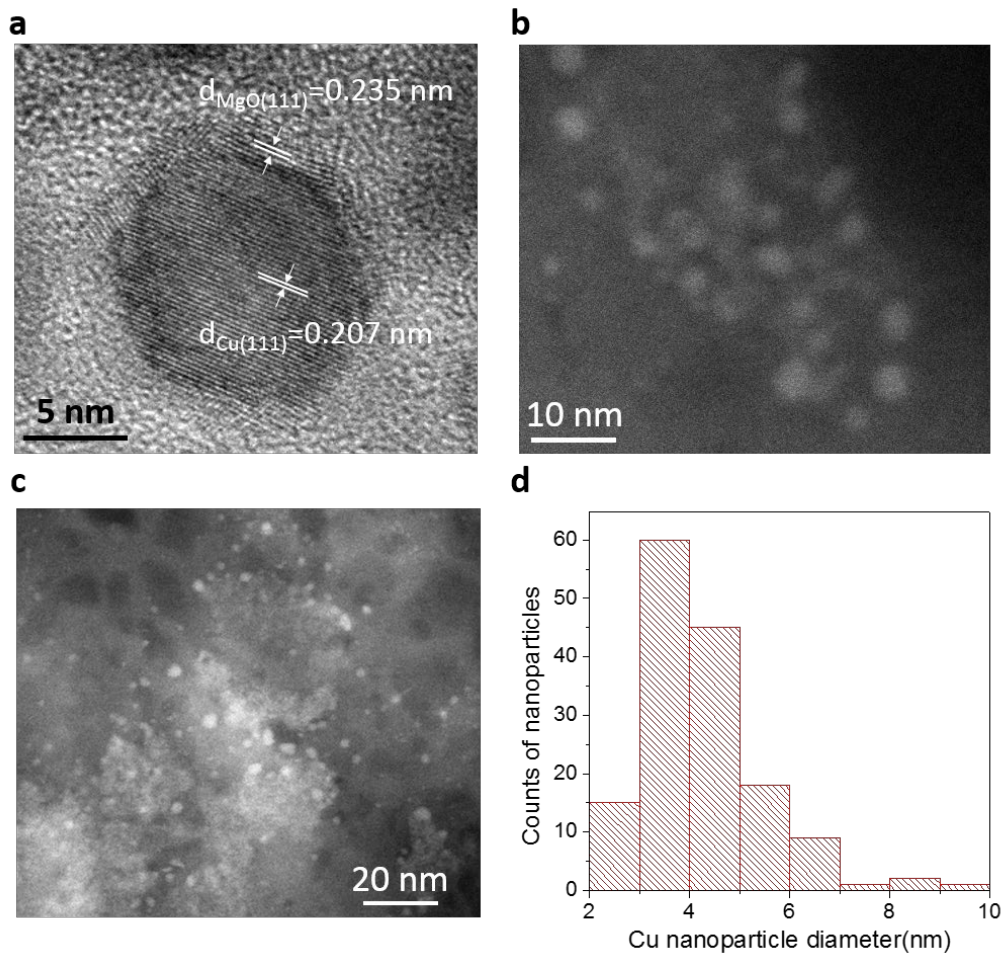


Figure 4.1 Electron microscopy measurement of supported Cu NPs on MgO- Al_2O_3 composite. (a) HR-TEM image of a Cu NP embedded in a MgO nanomatrix. (b-c) HAADF-STEM images of Cu NPs supported on MgO- Al_2O_3 composite. (d) Size distribution of Cu NPs.

dielectric environment composed of gas and oxide support¹⁶. The result shows a plasmonic absorption peak at $\sim 562 \text{ nm}$ (Figure 4.3b), consistent with the experimentally observed LSPR peak. However, the lineshape is quite different at the high-energy side of resonant wavelength ($\lambda < 550 \text{ nm}$). Amanda and her coauthors have shown that the optical absorption of plasmonic

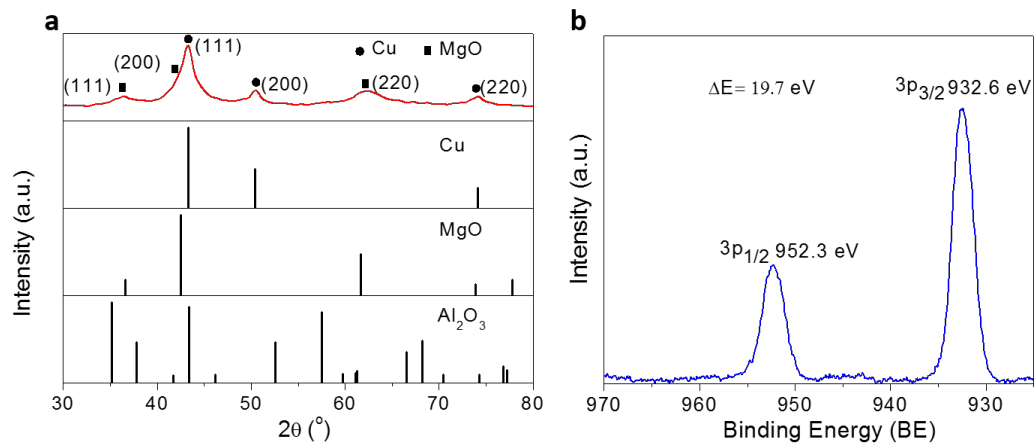


Figure 4.2 (a) Powder X-ray diffraction spectrum of supported Cu NPs. (b) X-ray photoelectron spectrum of supported Cu NPs. The BE of Cu 3p and the absence of shake-up satellite peaks indicate the metallic state of Cu NPs

assemble could be quite different from that of a single plasmonic NP, due to the secondary absorption effect of scattered photons from neighbored nanoparticles, especially for the sample with high concentration of plasmonic nanoparticles⁶⁹. Therefore we performed a similar Monte Carlo simulation to calculate the absorption quantum yield (fraction of impinged photons got absorbed) of assembling sample towards impinged photons of different wavelengths. Figure 4.3c shows the simulated spectrum, whose lineshape better matches the experimental spectrum than the simulated spectrum of a single Cu NP after normalization (Figure 4.3d), demonstrating the existence of secondary absorption of scattered photons within the ensemble of plasmonic Cu NPs. The calculated absorption quantum yield of

assembling sample will be used to calculate the effective absorption efficiency of copper NPs towards our laser light source later in section 4.4 to quantify the photothermal effect.

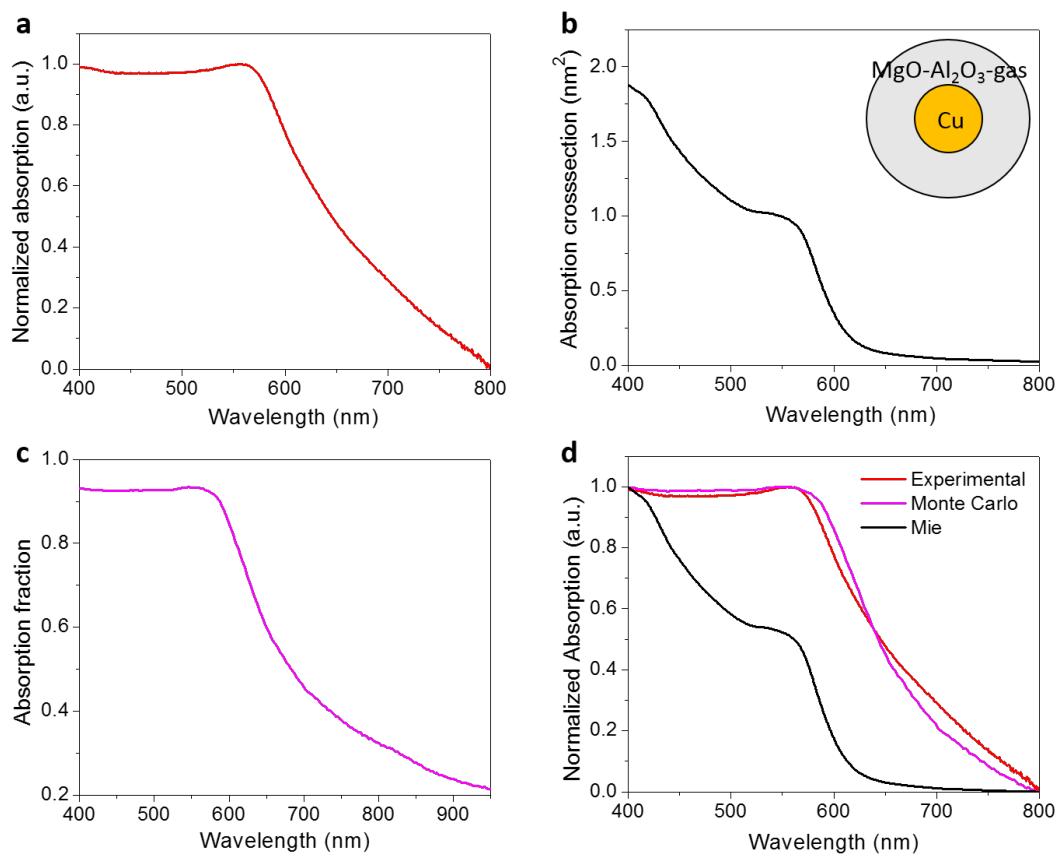


Figure 4.3 Optical property of supported Cu NPs. (a) The absorption spectrum of Cu/MgO-Al₂O₃ derived from UV-Vis diffused reflectance spectrum. (b) Calculated absorption cross-section spectrum of a single Cu NP embedded in an effective dielectric environment using FDTD simulation. (c) Calculated absorption fraction spectrum of Cu NPs ensemble using Monte Carlo simulation. (d) Comparison of the normalized experimental absorption

spectrum with normalized simulated absorption spectra by Mie theory and Monte Carlo simulation, respectively

4.3. Photocatalytic H₂-D₂ exchange on Cu/MgO-Al₂O₃

Photocatalytic H₂-D₂ exchange reaction was performed in the same photocatalysis system first described in section 3.2.2, but a new super-continuum fiber laser, SC-400-4, was used as the light source (light source spectrum as in Figure 2.1a). The laser spot size was focused to 1.4 mm in diameter. As the Cu/MgO-Al₂O₃ exhibit high activity, to maintain the differential reactor condition (low conversion), 100 sccm H₂ and 100 sccm D₂ flowed as the feed gases.

Under 16.2 W/cm² white light illumination, an extraordinary high reaction rate of 1.78 μmol /s (15.94 mmol HD/g Cu/s) was achieved. The HD formation rate returned to zero as soon as the light was turned off, confirming the contribution of light excitation to the observed catalytic activity. The sample is stable over 4 cycles of light on/off. Controlled photocatalysis experiment on oxide support (MgO-Al₂O₃) gave zero HD formation rate (Figure 4.4a) under the same illumination and flow conditions. This demonstrates that copper NPs are the active component in the photocatalyst. There is not HD formation either when the sample was illuminated in a helium atmosphere, excluding the possibility that HD signal might come from unknown contamination.

I further investigated the intensity dependence of photocatalysis (Figure 4.4b). Intriguing, the photocatalytic reaction rate exhibits an S-shape intensity dependence, a unique intensity dependence observed for the first time. Phenomenologically, the intensity dependence of photocatalytic efficiency can be categorized into three regions. At low-intensity region (0.32-1.6 W/cm²), the reaction rate seems to increase linearly with illumination intensity. While for intensity between 1.6 W/cm² and 5 W/cm², the reaction rate starts to show super-linear dependence on light intensity ($r \sim I^n$, $n > 1$) and the order (n) increases with light intensity. But for higher light intensity ($I > 5$ W/cm²), the order of super-linear dependence turned to decrease with intensity and finally returned to linear dependence.

Note that the measured photocatalytic reaction rate is the combined result of the hot-electron-mediated chemical reaction and photothermal-driven catalytic reaction. To extract the contribution of hot carriers and manifest the intensity dependence of hot-carrier-mediated reaction as well as the nature of hot carriers in this system, I quantified the photothermal effect through combining simulation and experimental measurement, which will be discussed in the next section.

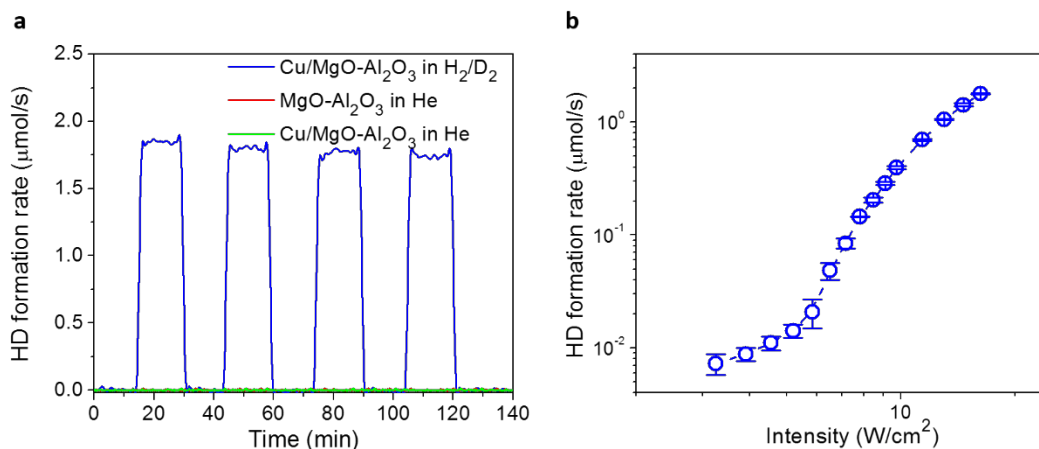


Figure 4.4 (a) Photocatalytic H₂-D₂ exchange reaction on Cu/MgO-Al₂O₃ and controlled experiments. (b) Intensity dependence of photocatalytic H₂-D₂ exchange reaction on Cu/MgO-Al₂O₃.

4.4. Quantification of the photothermal effect

The photothermal effect, which was defined as temperature increase and the concomitant thermocatalytic activity due to light-to-heat conversion through electron-phonon and phonon-phonon interaction during the non-radiative decay of plasmon, was quantitatively evaluated by combining experimental measurement and theoretical simulation.

Under continuum illumination, the sample pellet will reach a static-state temperature distribution in the volume balanced by adsorbed light power and heat dissipation rate. For pulse laser source, while the matrix will still reach a quasi-static-state temperature distribution controlled by the macroscopic heat conducting, the local temperature of individual copper NP will be higher than the matrix temperature

instantaneously after each pulse, as illustrated in Figure 4.5a. The upper limit of this instantaneous, local temperature on a single Cu NP was calculated using the adiabatic heating model, as described in Appendix A. It shows that this instantaneous, local temperature is < 1 K higher than the static-state, global temperature that can be measured by a thermal imaging camera, for Cu NP size ranging from 3 to 10 nm, due to the low pulse intensity we used Figure 4.5b-d. Note that though the time-average laser intensity was plot as the y axle in the figure, the pulse intensity was used in the calculation. Thus the steady-state, global temperature could effectively represent the photothermal effect.

To quantify the photothermal effect, a 3D temperature distribution in the volume of the sample pellet and the temperature dependence of the thermocatalytic reaction rate are needed. The static-state temperature distribution in the 3D volume of the sample pellet was calculated using the multi-physics method in COMSOL. A model mimicking the structure of reactor and catalyst pellet was built in COMSOL to obtained a spatial function of heat capacity ($C(T, x, y, z)$) and thermal conductivity ($\sigma(T, x, y, z)$), which also depend on the temperature. The light intensity distribution of the laser spot on the sample pellet is a 2D Gaussian function ($I(x, y)$). The surface distribution of absorbed light intensity ($I_a(x, y)$) on the pellet can be calculated by multiplying the light intensity function ($I(x,y)$) with the effective absorption efficiency of the sample pellet towards the light source (η), which was obtained by integrating the product of the calculated absorption quantum yield spectrum of ensemble sample

($\eta(\lambda)$) from Monte Carlo simulation (Fig Figure 4.3c) and the spectrum of our light source ($I(\lambda)$). By solving the heat transfer equation with the property functions

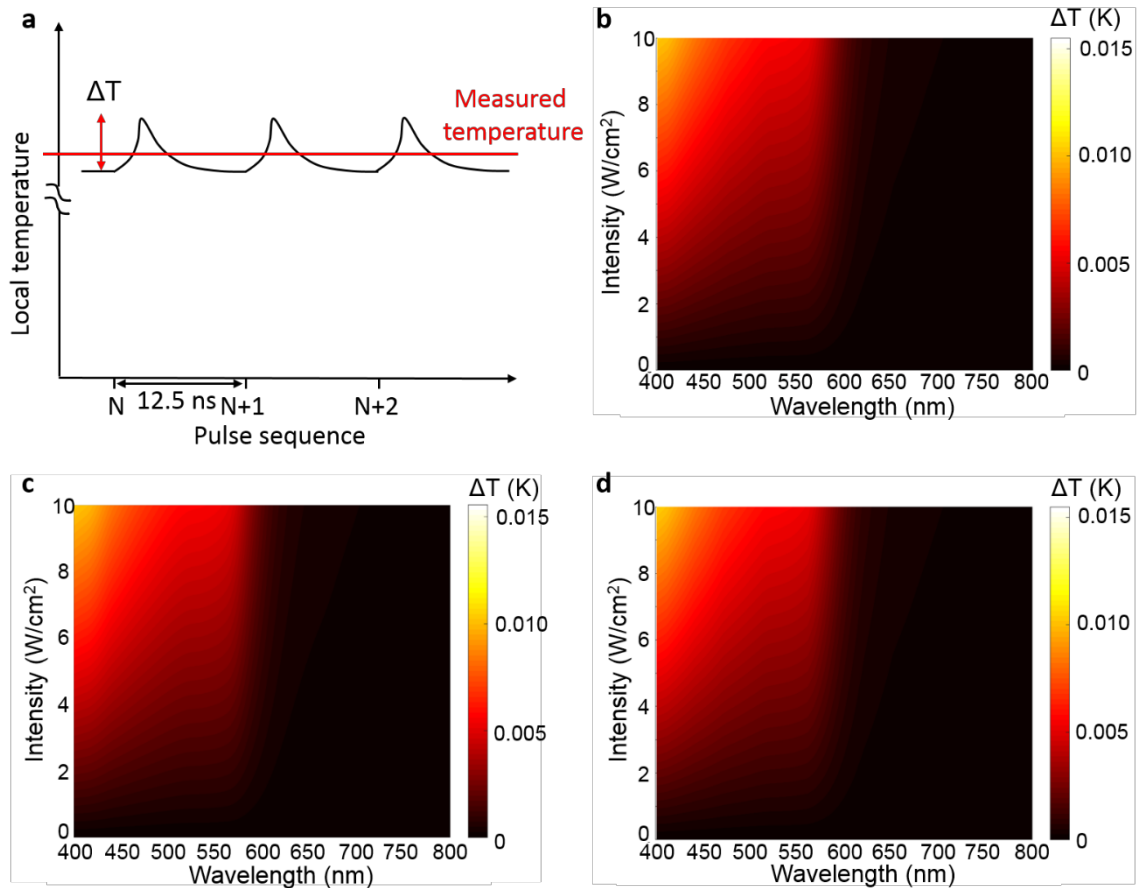


Figure 4.5 Instantaneous photothermal effect of laser pulse excitation. (a) Schematics of the local temporal temperature of copper nanoparticles under illumination of periodic pulses. (b-d) Contour map of the calculated instantaneous, local temperature increase of (b) 3 nm, (c) 5 nm and (d) 10 nm Cu NP. ¹⁶

($C(T, x, y, z)$ & $\sigma(T, x, y, z)$) and energy input functions ($I_a(x, y)$) as input, we were able to calculate the 3D temperature distribution ($T(x, y, z)$) in sample volume under

various light intensities. Figure 4.6a shows the calculated temperature distribution in the sample pellet under 16.2 W/cm² illumination, the maximal intensity we investigated in this system, as an example. The accuracy of the simulation results is confirmed with the coincidence of simulated surface temperature at the center of the light spot and the experimentally measured highest surface temperature with a thermal camera (Figure 4.6b). The thermocatalysis was performed in a quartz tube furnace with temperature ranging from 40 to 227 °C. The results were fitted with the Arrhenius equation to get an apparent activation barrier of 0.54 eV (Figure 4.6c) and an analytic rate equation as a function of temperature:

$$k = 2.1 * 10^9 * \exp\left(-\frac{6263}{T(K)}\right) \text{ umol} * \text{g}^{-1} * \text{s}^{-1}$$

Equation 4.1 rate equation of thermocatalytic H₂-D₂ exchange reaction

By applying the rate equation into the temperature distribution ($T(x, y, z)$), we obtain a reaction rate distribution ($r(x, y, z)$). Integrating $r(x, y, z)$ over the whole pellet volume gives the net photothermal reaction rate, as shown in Figure 4.6d. Different from the photocatalytic reaction rate, the photothermal reaction rate increases exponentially with the light intensity. This is reasonable as the surface temperature of photocatalyst pellet increases almost linearly with the impinged light intensity while the thermocatalytic reaction rate is exponentially dependent on temperature. The contrast intensity dependence between the photocatalytic rate and

the photothermal rate, especially at the high-intensity region, indicates a low contribution of photothermal effect in the photocatalysis.

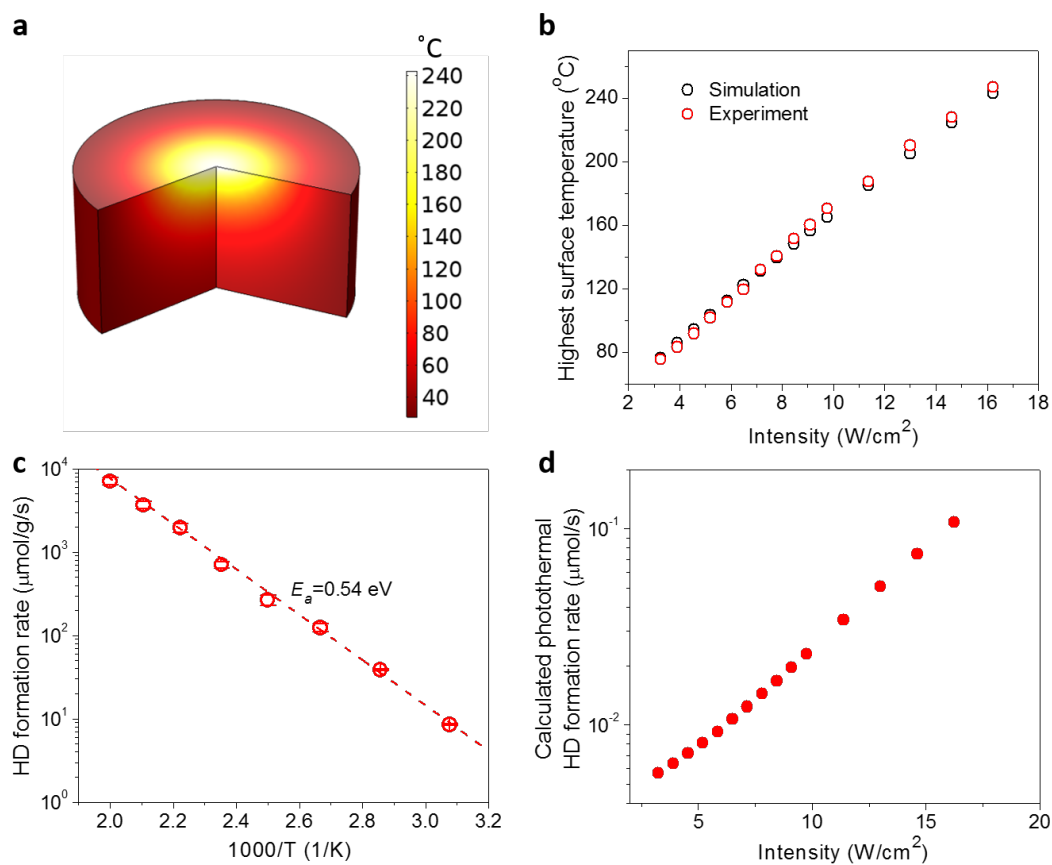


Figure 4.6 Quantification of photothermal effect. (a) The 3D temperature distribution of catalyst pellet under 16.2 W/cm² while light illumination without external heating. **(b)** Comparison of experimentally measured surface temperature with simulated surface temperature. **(c)** Temperature dependence of thermocatalytic reaction rate. The Dash straight line is the

Arrhenius fitting. (d) The calculated photothermal HD formation rate in photocatalysis.

4.5. Demonstration of the thermalized-hot-carrier mechanism

Since we have quantified the photothermal effect, hot-electron-mediated reaction rate can be obtained by subtracting the calculated photothermal reaction rate from the overall photocatalytic reaction rate and the external quantum yield (η_r) can be well defined as the ratio of hot-carrier-mediated HD formation rate to the impinge photon flux, which shows an S-shape intensity dependence (Figure 4.7a). Note that η_r exceeds 1 for light intensity above $\sim 13 \text{ W/cm}^2$! The contribution of hot electrons increases with light intensity and achieve above 90% when the light intensity is higher than 8 W/cm^2 (Figure 4.7b), supporting the predominated role of hot carriers in photocatalysis

Solely a linear dependence ($r \propto I$)^{3, 6} and a transition from linear to superlinear dependence ($r \propto I^n$) with n increasing¹⁴ have been reported for the intensity dependence of reaction rate in plasmonic photocatalysis, which were explained by the desorption induced by electronic transition (DIET) (ref) and desorption induced by multiple electronic transition (DIMET) mechanism (ref), respectively. Note that both models were discussed with a default hypothesis of one photon to one hot carrier conversion. In other words, initial hot carriers are the effective hot carriers. For thermalized hot carriers, due to the non-linear electron-electron scattering process, the amount of generated hot carriers is expected to exhibit a non-linear

dependence on the impinged photon intensity. Also, the external quantum yield of photon-to-chemical conversion can be more than 1 because of the conversion of one photon to multiple hot carriers in hot carrier multiplication process. Thus we propose the thermalized hot carriers to be the predominated effective hot carriers in this system.

A simplified model that separates the internal thermalization (electron-electron scattering) and external thermalization (electron-phonon scattering) was used to calculate a quasi-Fermi-Dirac distribution of thermalized hot carriers adiabatically and predict the quantum yield of thermalized hot carriers (see Appendix B for method details). The rationality of this simplification is the different lifetime of these two processes (sub-picosecond vs. picoseconds). Figure 4.8a shows an obtained quasi-Fermi-Dirac distribution of thermalized hot carriers in a single 5 nm Cu NP under a specific energy input (corresponding to a specific light intensity). By integrating the density of hot carriers over energies above different energy thresholds (E_a), we can obtain the theoretical quantum yield of effective thermalized hot carriers for different hot-carrier transferring barriers. For a specific energy threshold, the quantum yield of thermalized hot carriers exhibits a similar S-shape dependence on input energy (corresponding the light intensity in experiments), well reproducing the intensity dependence of external quantum yield of the hot-carrier-mediated chemical reaction. Moreover, as expected, with lower energy threshold (transferring barrier), the quantum yield of effective hot carriers increases under the same energy input. For low enough energy threshold ($E_a \leq 0.3$ eV), the quantum yield

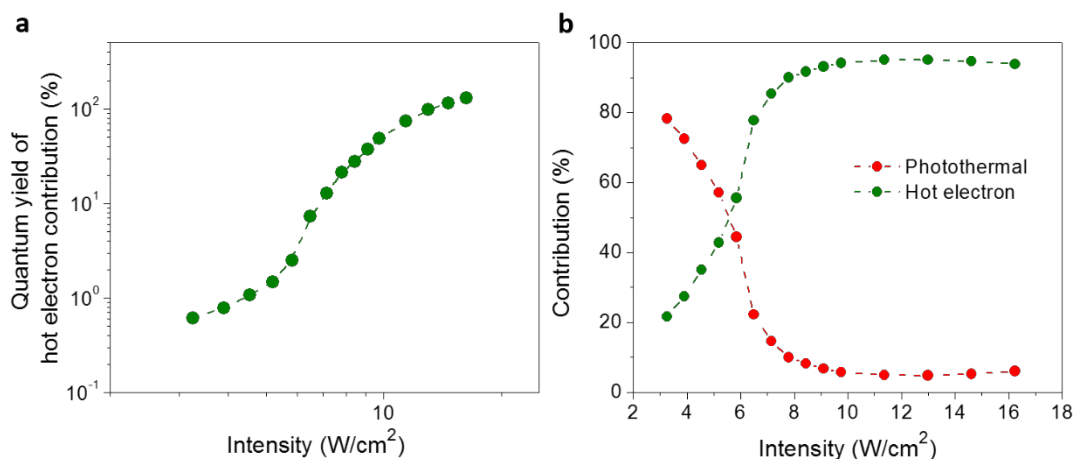


Figure 4.7 (a) Intensity dependence of hot-carrier-mediated chemical reaction. (b) Intensity dependence of contribution of hot-carrier-mediated chemical reaction and photothermal effect in photocatalysis.

of effective thermalized hot carriers could be more than 1. Here the highest energy threshold that could achieve quantum yield more than 1 can be defined as the critical energy threshold (E_c).

Note that the experimentally obtained external quantum yield is higher than the theoretically predicted upper-limit of quantum yield of thermalized hot carriers. This is probably caused by the difference between the ideal thermal distribution of hot carriers in the model and the realistic quasi-equilibrium distribution of hot carriers countered by surface adsorbed molecules. Contribution from the ineffective hot carriers in the model is possible during the thermalization process in reality

because the internal thermalization of hot carriers and the hot-carrier transferring for molecular activation happen simultaneously with similar lifetime. Thus the effective critical energy threshold could also be higher.

In a word, this theoretical model predicts phenomena that are coincident with the experimental results and demonstrates the dominated role of thermalized hot carriers in hot-carrier-mediated H₂-D₂ exchange reaction on copper. Compared to the Au and Al surface, where the H₂/D₂ dissociation is likely to be the rate-determining step and the corresponding antibonding orbital lays high above the Fermi level, requiring highly energetic electrons, the HD desorption is believed to be the rate-determining step on copper surface⁷⁰⁻⁷². Thus the reaction is likely to be enhanced through Cu-H bond weakened by hot carrier transition. DFT calculation showed that the antibonding orbital of Cu-H spans over the Fermi level of Cu, partially filled even at the ground state⁷³. The barriers for hot carriers to transfer to the Cu-H bond is therefore low, making the thermalized hot carriers, tremendous in number but lower in energy, very efficient.

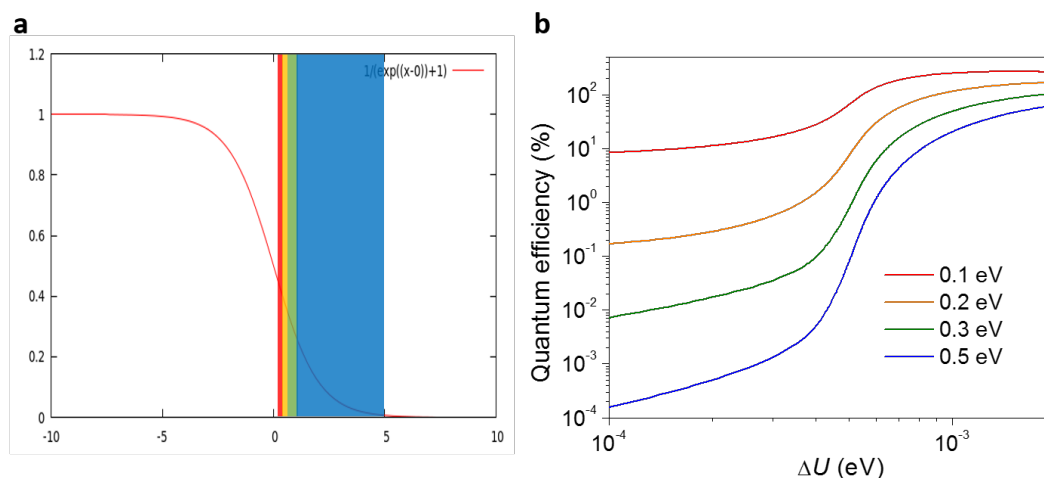


Figure 4.8 Theoretical calculation of generation of thermalized hot carriers (a) quasi-Fermi-Dirac distribution of thermalized hot carriers with color shadows indicating the integration ranges for different thresholds of hot carrier transferring. (b) Calculated input energy dependence of quantum yield of thermalized hot carriers generation.

4.6. Conclusion

In this chapter, I showed a unique, S-shape intensity dependence of plasmon photocatalysis, which is believed to be reported for the first time. The contribution of hot carriers was extracted by quantifying the photothermal effect and the external quantum yield of the hot-carrier-mediated chemical reaction is found to be more than 1. The true role of hot carriers is likely to be thermalized hot carriers because a model simulating the quantum yield of thermalized hot carrier generation reproduces the S-shape intensity dependence. The low barrier for hot carrier transferring to and

subsequently activating the intermediates in the rate-determining step is believed to be crucial in efficient usage of thermalized hot carriers.

Appendix B

Thermalized hot carrier calculation

In the calculation, we assume that the period of incoming photon is smaller than the typical electron-electron relaxation time. Thus, at the end of relaxation, the electron state is still Fermi-Dirac distribution at a higher temperature. In a very short period, the heat loss (electron-phonon scattering) is negligible, as electron-electron scattering and electron transferring have a shorter lifetime. Thus hot carriers will approach equilibrium while activating chemical reaction before substantially cooling down to Fermi level. The number of hot electrons above a certain threshold is given by

$$n = \int_{E_{thr}}^{\infty} f_T(E) \rho(E) dE$$

where $f_T(E)$ is the Fermi-Dirac distribution at temperature T , $\rho(E) = \frac{V}{2\pi^2} \left(\frac{2m}{\hbar^2}\right)^{3/2} \sqrt{E - E_F}$ is the electronic density of states.

The total energy absorbed can be written as

$$\Delta U = I\Delta t = U_T - U_{T_0} = \frac{1}{2} \int (f_T - f_{T_0}) \rho E dE$$

where T_0 is the initial temperature set as 300K, T is the equilibrium temperature, ω is incident photon energy, Δt is set as typical pulse period, I is the

intensity of the laser. We assume the timewise average distribution is the mean value of initial and fully relaxed states. Finally, the quantum yield is

$$QY = \frac{n}{\Delta n} = \frac{n\omega}{\Delta U}$$

From the QY formula, it is clear that the asymptotic value of QY is proportional to incident photon energy.

Surface alloy as a promising antenna-reactor structure for plasmonic photocatalysis

5.1. Antenna-reactor plasmonic photocatalysts

Although gold, aluminum and copper nanostructures exhibit strong LSPR and high optical cross-section towards the visible and ultraviolet light, rendering them high efficiency in light absorption and hot carriers generation, their relatively inert chemical activity limit the efficacy of generated hot carriers in activating molecules/intermediates on the catalyst surface. On the other hand, catalytically active nanoparticles, especially the noble metals which possess favorable electronic structure for molecule absorption and bond activation⁷⁴, interact weakly with the light⁷⁵⁻⁷⁶. A promising strategy to further improve the plasmonic photocatalysts is integrating the catalytic components with the plasmonic nanostructures to form the so-called antenna-reactor complex.

Previously, Dayne Swearer *et al.* have reported the transition metal nanoparticles decorated Al nanocrystal as an antenna-reactor structure^{17, 77}. In this structure, the antenna and reactor are bridged through the near-field driven oscillation. The LSPR excited in the plasmonic aluminum nanocrystal under illumination can drive the electron oscillating in the non-plasmonic reactor through its optical near field¹⁸. This “forced plasmon” will decay into hot carriers, even more efficiently than plasmonic metals due to the high damping effect of non-plasmonic metals, and activate chemical reaction with its innate catalytic activity. However, the overall efficiency of this satellites-planet antenna-reactor structure might be limited by the efficiency of energy transduction between the antenna and reactor.

Here I will show the surface alloy to be an effective antenna-reactor structure. The plasmonic antennas, when small, provide a high branching ratio in absorption and thus efficiently generate hot carriers under illumination, while the reactor sites on the antenna surface offer high catalytic activity¹⁶. The local electronic inhomogeneity at the reactor site could further facilitate the generation of hot carriers²⁰ and render high photocatalytic activity.

5.2. Ru-on-Cu surface alloy for photocatalytic ammonia decomposition

Ru-on-Cu surface alloy was prepared and applied in photocatalytic ammonia decomposition reaction. The Ru is chosen as the reactor as it exhibits the best activity towards NH_3 decomposition reaction⁷⁸. The hot carriers generated on Cu surface could transfer to surface Ru sites and activate the chemical reactions with a lower barrier. The reaction mechanism of NH_3 decomposition is well studied, with no side reactions⁷⁹⁻⁸⁰, and NH_3 is a promising medium for CO_x -free hydrogen storage⁸¹. This structure can potentially be applied to other antenna and reactor materials, providing the flexibility in optimizing the complex for specific reactions.

5.2.1. Synthesis and characterization of photocatalysts

A Ru-on-Cu surface alloy NPs (19.5 at% Cu & 0.5 at% Ru) supported on MgO- Al_2O_3 composite (60 at% Mg & 20 at% Al) was prepared by constant-pH coprecipitation method (ref), using the same procedure described in section 4.2. But an aqueous solution containing 0.195 M $\text{Cu}(\text{NO}_3)_2$, 0.005 M RuCl_3 , 0.6 M $\text{Mg}(\text{NO}_3)_2$ and 0.2 M $\text{Al}(\text{NO}_3)_3$ was used instead. Thereafter the Ru-on-Cu surface alloy photocatalyst was denoted as $\text{Cu}_{19.5}\text{Ru}_{0.5}$. Pure Cu NPs (Cu_{20}) and Ru NPs ($\text{Ru}_{0.5}$) supported on MgO- Al_2O_3 matrix were also synthesized and tested for comparison. Cu_{20} was prepared using the same procedure as described in section 4.2. For $\text{Ru}_{0.5}$, the same procedure was applied, but a solution containing 0.005 M RuCl_3 , 0.746 M $\text{Mg}(\text{NO}_3)_2$ and 0.249 M $\text{Al}(\text{NO}_3)_3$ was used.

The particle size distribution of Ru-on-Cu surface alloy nanoparticles and Cu nanoparticles were similar, with an average diameter of ~ 5 nm (a-c vs. d-f), while Ru nanoparticles synthesized under similar conditions are larger with an average diameter of ~ 15 nm (g-i). As like in the Cu₂₀ sample, the Cu and MgO are crystalline while the Al₂O₃ is amorphous in the Ru-on-Cu surface alloy sample (Figure 5.2a). The concentration of Ru is below the detection limit of PXRD. The Ru 3p_{3/2} binding energy in the Cu_{19.5}Ru_{0.5} sample shifts to a higher value than that in the Ru_{0.5} sample (Figure 5.2b), indicating electron transfer from Ru to Cu⁸² and forming of the copper-ruthenium alloy. The surface structure of the Cu_{19.5}Ru_{0.5} was verified using N₂O chemisorption experiment⁸³. According to the surface reaction: $2\text{Cu}_s + \text{N}_2\text{O} \rightarrow \text{Cu}_2\text{O} + \text{N}_2$, the concentration of surface copper atoms (Cu_s) was quantified by measuring the amount of released N₂ using the mass spectrometer. Ru surfaces are more resistant to oxidation and do not react with N₂O at 313 K.

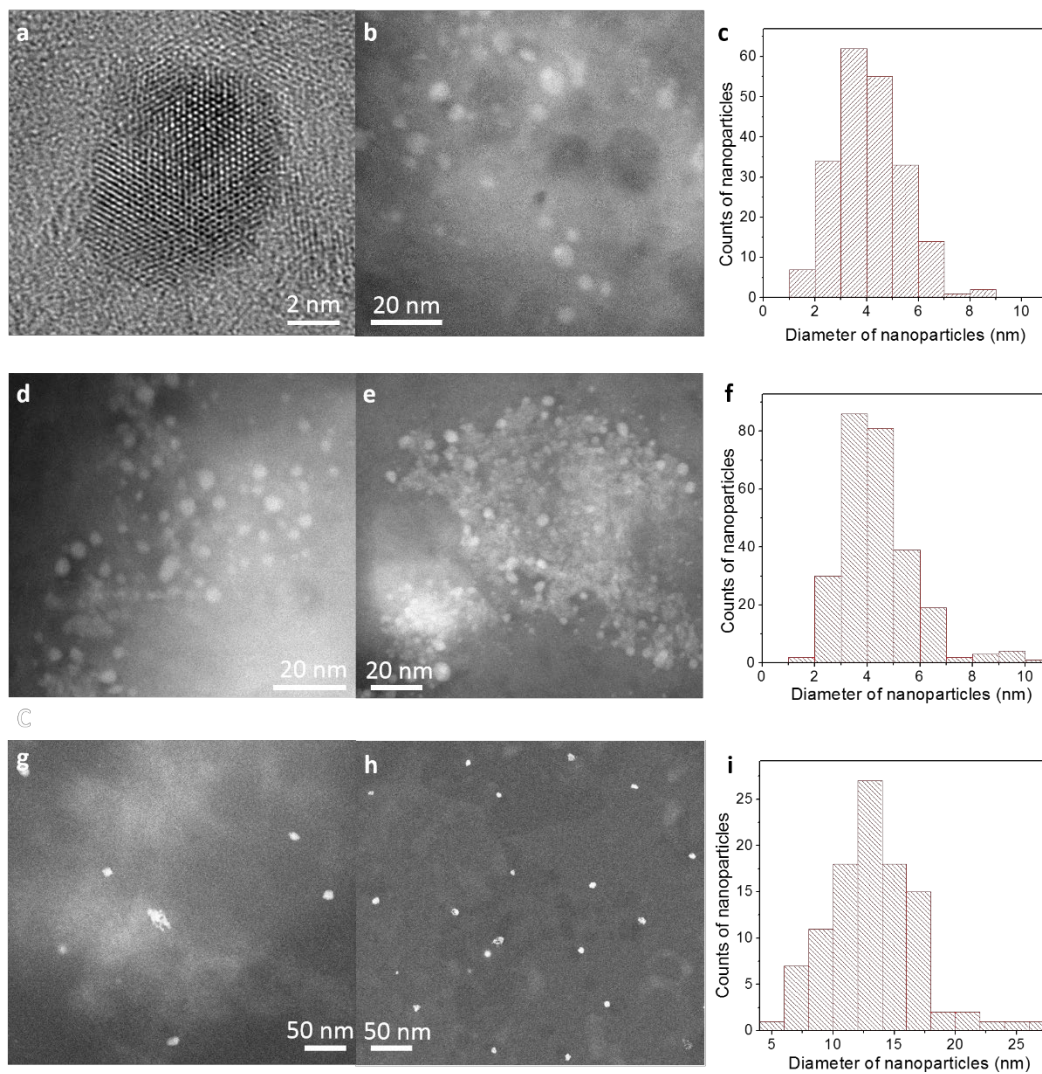


Figure 5.1 Transmission electron microscope (TEM) images and size statistics of supported metal NPs. (a) HR-TEM image of a single Ru-on-Cu surface alloy NP. (b) HAADF image of Ru-on-Cu surface alloy NPs on MgO-Al₂O₃ support. (c) Size distribution of Ru-on-Cu surface alloy NPs. (d,e) HAADF images of Cu NPs

on MgO-Al₂O₃ support. (f) Size distribution of Cu NPs. (g,h) HAADF images of Ru NPs on MgO-Al₂O₃ support. (i) Size distribution of Ru NPs. ¹⁶

Thus the surface concentration of Ru was calculated by subtracting the surface concentration of Cu in the Cu_{19.5}Ru_{0.5} sample from that of the Cu₂₀ sample. The concentration of Cu_s in the Cu₂₀ sample is 94.8 μmol/g (Figure 5.2c). In contrast, the concentration of Cu_s in the Cu_{19.5}Ru_{0.5} sample was measured to be 49.2 μmol/g. The decrease in concentration of surface copper (43.6 μmol/g) is close to the bulk concentration of Ru (56.5 μmol/g) in the Cu-Ru surface alloy measured by ICP-MS, suggesting that most of the Ru atoms enrich on the surface of Cu NPs in the Ru-on-Cu surface alloy sample. Ru-on-Cu surface alloy exhibits an LSPR peak centered at ~560 nm with high absorption, nearly identical to pure Cu NPs (Figure 5.2d), indicating a minimal perturbation of the optical property of plasmonic Cu due to the formation of surface alloy structure. Instead, the Ru NPs show a characteristic spectrum of transition metals with absorption monotonously rising when the wavelength scans from visible to UV due to interband transition (Figure 5.2d, short dash line). The low absorption of Ru NPs is in high contrast to the large absorption cross-section of Ru-on-Cu surface alloy NPs and Cu NPs that resulted from the LSPR of plasmonic Cu.

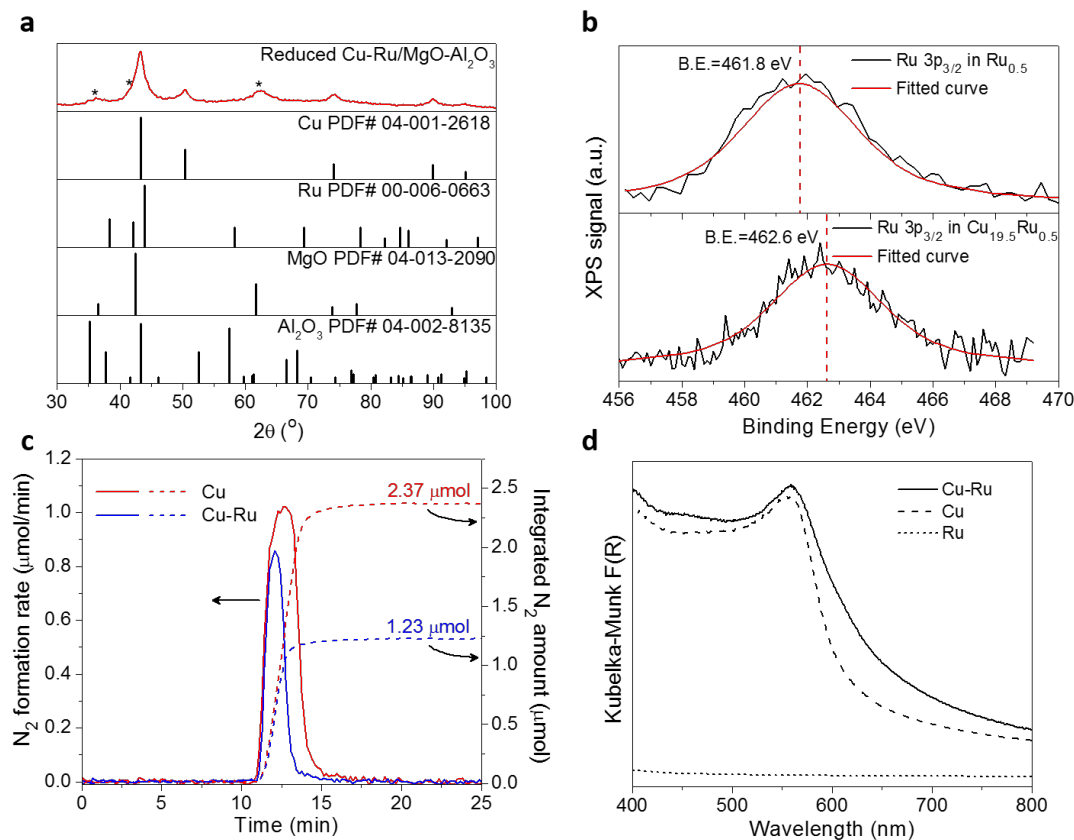


Figure 5.2 Other characterizations of Ru-on-Cu surface alloy NPs and Cu and Ru NPs. (a) Powder X-ray diffraction (PXRD) spectrum of supported Cu-Ru surface alloy NPs. The standard PXRD data of Cu, Ru, MgO, and Al₂O₃ from International Centre for Diffraction Data (ICDD) were plotted for reference. (b) X-ray photoelectron spectra of Ru 3p_{3/2} peaks for (top panel) supported Ru NPs (Ru_{0.5}) and (bottom panel) supported Cu-Ru surface alloy NPs (Cu_{19.5}Ru_{0.5}). The chemical shift of Ru 3p_{3/2} in Cu_{19.5}Ru_{0.5} to higher energy compared to that in Ru_{0.5} indicates electron transfer from Ru to Cu. (c) N₂O chemisorption spectra of 50 mg supported Cu-Ru surface alloy NPs (blue), and 50 mg supported Cu NPs (red) at 313 K. Solid lines represent the N₂ formation rates, while dash lines show the total released N₂ by integrating the formation rate of N₂ over time. (d)

UV-Vis diffuse reflectance spectra of supported Cu-Ru surface alloy NPs (solid line), Cu NPs (dashed line) and Ru NPs (short-dashed line).¹⁶

5.2.2. Photocatalytic ammonia decomposition for hydrogen storage

The photocatalytic NH₃ decomposition experiments were performed in the same photocatalysis system. Super-continuum fiber laser (SC-400-8) and Hiden mass spectrometer were used as the light source and detector, respectively, while anhydrous purity NH₃ (99.99%, Matheson) was used as the reactant. The laser spot size was focused to 2 mm diameter. Under 9.6 W/cm² white-light laser illumination, the photocatalytic reaction rate of Cu_{19.5}Ru_{0.5} was ~20 and ~177 times, respectively, higher than that of Cu₂₀ and Ru_{0.5} samples (Figure 5.3a), which demonstrates the advantage of surface alloy combining plasmonically active antenna and catalytically active reactor. Especially, the photocatalytic reaction rate of Cu_{19.5}Ru_{0.5} was as high as 1.2 mmol H₂/g cat/s. The turnover frequency (TOF) based on Ru loading was > 15 s⁻¹ and the energy efficiency (ammonia decomposition reaction is an endothermic reaction with $\Delta H_{rxn}^o = +46 \text{ kJ/mol}$) and quantum yield were calculated to be 18% and 33.5%, respectively, under this condition, according to the following equations.

$$TOF_{Ru}(h^{-1}) = \frac{r_{abs}(\mu\text{mol} \cdot \text{s}^{-1})}{n_{Ru}(\mu\text{mol})} \cdot 3600(\text{s} \cdot \text{h}^{-1})$$

Equation 5.1 Turnover frequency of H₂ production rate

$$\eta_{energy} = \frac{\text{reaction rate (mol NH}_3\text{/s)} * \text{reaction enthalpy (J/mol)}}{\text{optical power (J/s)}} \cdot 100\%$$

Equation 5.2 Energy efficiency of photocatalytic NH₃ decomposition

$$\text{Quantum yield} = \frac{\text{reaction rate (mol N}_2\text{/s)} * N_A}{\text{optical power (J/s)} / \bar{E}_{\text{photon}}(\text{J})} \cdot 100\%$$

Equation 5.3 Quantum yield of photocatalytic NH₃ decomposition

Where \bar{E}_{photon} is the average photon energy of our laser light source, which is 1.77 eV, equivalent to $2.83 \cdot 10^{-19}$ J

The thermocatalytic activity of Ru_{0.5} was higher than Cu₂₀ due to the intrinsically better activity of Ru metal towards ammonia decomposition reaction. Note that the loading of Ru is lower and the Ru NPs are larger. The Cu_{19.5}Ru_{0.5} shows better thermocatalytic activity than Ru_{0.5}, probably because of more surface sites of Ru in Ru-on-Cu surface alloy. The photocatalytic reaction on the Cu_{19.5}Ru_{0.5} sample responds instantaneously to light on/off operations and this process can be repeated reproducibly multiple times (Figure 5.3b, 5 times), indicating the stability of Ru-on-Cu surface alloy photocatalyst. The ratio of photocatalytic reaction rates based on the

measured amounts of NH_3 , N_2 , and H_2 were consistent with the stoichiometry of the reaction, confirming the absence of unintended side reactions.

Again, to differentiate the contributions of plasmon-induced hot carriers and photothermal heating, I measured the steady-state highest surface temperature (T_{hs}) on the photocatalyst pellet *in-situ* using the thermal imaging camera. The T_{hs} increased with laser intensity and reached ~ 475 °C at 9.6 W/cm^{-2} , the maximal intensity we investigated (Figure 5.3c). Compared to the case of H_2 - D_2 exchange reaction on Cu NPs, the dependence of T_{hs} on light intensity is sublinear in the NH_3 decomposition experiment. This is probably due to the different temperature dependence of the thermal conductivity of H_2/D_2 and NH_3 gases. When NH_3

decomposition was performed without illumination, but with external heating

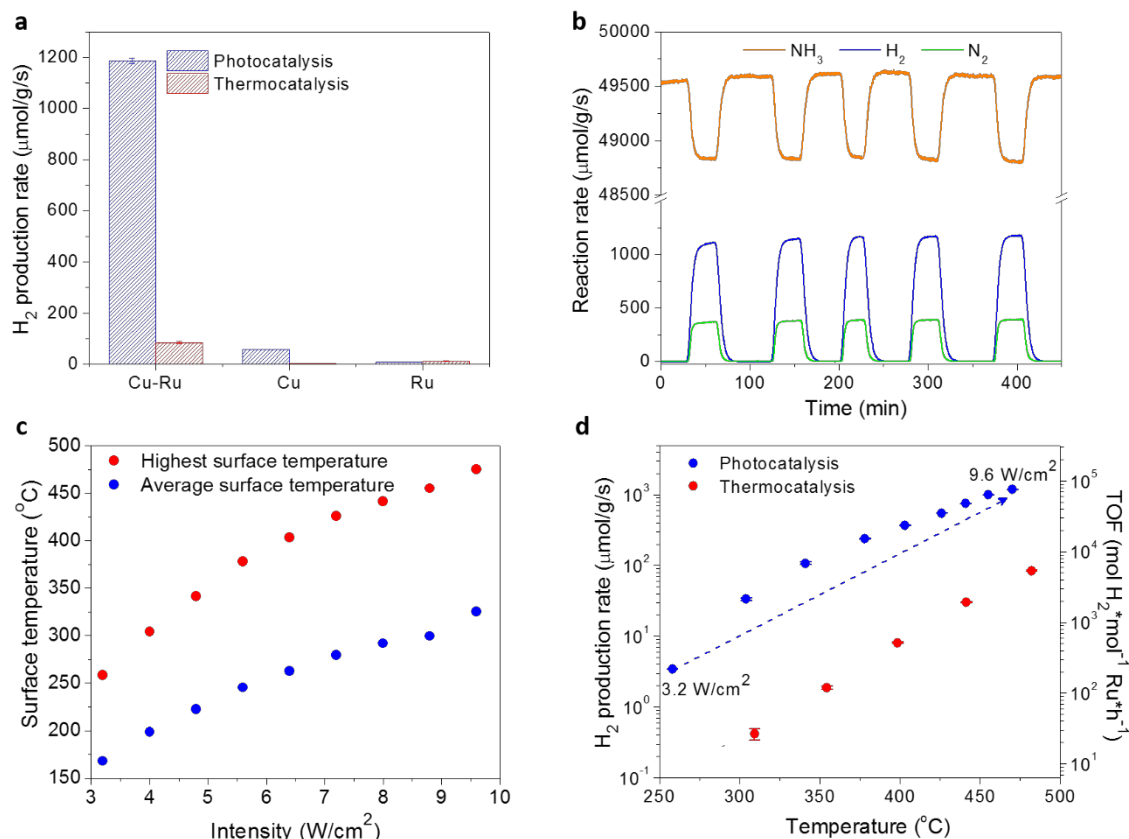


Figure 5.3 Catalytic measurement of ammonia decomposition reaction. (a) The H₂ formation rate of photocatalysis (9.6 W/cm²) and thermocatalysis (482 °C) on supported Cu-Ru surface alloy, Cu NPs, and Ru NPs (b) Multiple-hour measurement of photocatalytic ammonia decomposition on Cu_{19.5}Ru_{0.5} surface alloy NPs under 9.6 W/cm² white light illumination without external heating. (c) (d) Comparison of photocatalytic and thermocatalytic reaction rates on supported Cu-Ru surface alloy. The x-axis values of photocatalysis data points correspond to the highest surface temperature of the photocatalyst due to light-induced heating. The intensity differences between data points for photocatalysis is 0.8 W/cm².¹⁶

temperatures equivalent to those achieved under illumination, the thermocatalytic rates of H₂ production were one to two orders of magnitude lower than the observed photocatalytic rates (Figure 5.3d). Note that the instantaneous temperature on Cu NPs right after laser pulse excitation has been calculated to be less than 0.1 K higher than the steady-state global temperature measured by the thermal camera in section 4.4. Based on this observation, we conclude that the plasmon-induced hot carriers are the predominant effect that catalyzes NH₃ decomposition.

Photocatalytic NH₃ decomposition rate on Cu_{19.5}Ru_{0.5} surface alloy also exhibits an S-shape intensity dependence, indicating the likely thermalized-hot-carrier mechanism as in the H₂-D₂ exchange reaction on Cu NPs. This might be another reason for the high quantum yield in this system as the hot carrier multiplication process amplifies the effective hot carriers. The wavelength dependence experiments were performed by passing the white light laser through a series of bandpass filters with a bandwidth of 50 nm and a neutral density filter to get monochromatic lights with a constant intensity of 3.2 W/cm². The maximal photocatalytic reaction rate happened under excitation of 550 nm light, coincident with the dipolar LSPR mode of the Ru-on-Cu surface alloy sample (Figure 5.2d). For longer excitation wavelengths (> 550 nm), the photocatalytic reaction rate reduced due to the decreased optical absorption, and therefore a decrease in hot carrier generation. For shorter excitation wavelengths (< 550 nm), the absorption is still large, due to the Cu interband transition⁸⁴, but the enhancement of reaction rate is not as substantial because the energetic electrons produced by interband transitions

in coinage metals like Cu have significantly lower energies than those produced by plasmon decay⁶⁶.

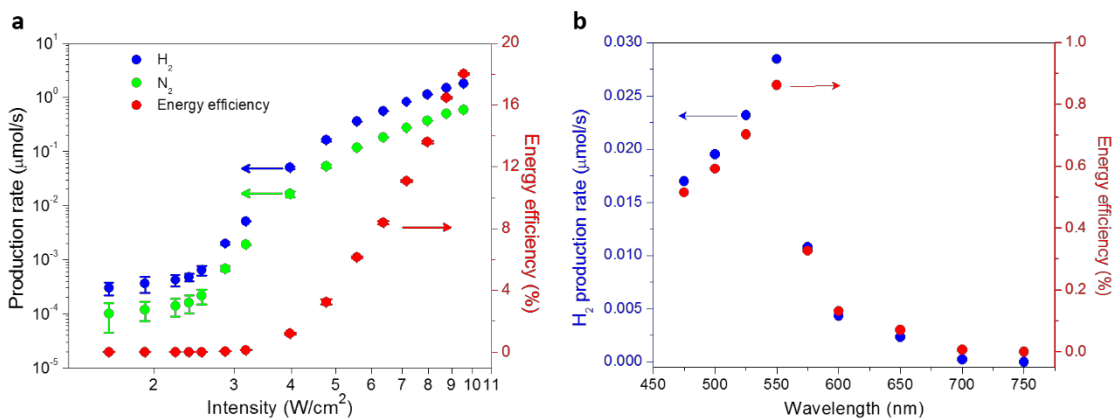


Figure 5.4 Photocatalytic behavior of supported Cu-Ru surface alloy NPs. (a) Intensity dependence of reaction rate and energy efficiency under white light illumination. Feeding rate of NH_3 was 5 sccm for the intensity range of 1.6-3.2 W/cm^2 and 100 sccm for 4-9.6 W/cm^2 . (b) Wavelength dependence of reaction rate and energy efficiency. The intensity was kept 3.2 W/cm^2 for all the wavelengths. Feeding rate of NH_3 was 5 sccm.¹⁶

5.2.3. Light-dependent activation barrier

In addition to enhancing reaction rate, another intriguing effect of the hot-carrier-mediated process that people expect to see is the reduction of thermal activation barrier. Although there are a few reports about the reduction of activation barriers by simultaneous illumination of plasmonic nanoparticles in thermal catalysis⁸⁵⁻⁸⁶, a comprehensive measurement of activation energies under various illumination conditions, which could shine light onto the mechanism of hot-carrier-induced

reduction of activation barriers, is lacking. Here I did a systematic investigation of the effect of light excitation on the activation barrier of ammonia decomposition reaction and revealed the origin as the excitation of the rate-determining step by hot carriers.

To quantify apparent activation barrier (E_{app}) under various illumination conditions, I measured the reaction rates over a series of surface temperatures for each wavelength (λ) and laser intensity (I) by varying the chamber temperature. The photocatalytic reaction rates were obtained by subtracting the reaction rate at a specific illumination condition and chamber temperature from the reaction rate at the same chamber temperature in the dark. This only includes the hot-carrier-driven contribution and photothermal effect. Since we have demonstrated that the photothermal effect is very weak in the photocatalysis of this system, the obtained photocatalytic reaction rate is mostly the hot-carrier-mediated reaction rate. The $E_{app}(\lambda, I)$ for each illumination condition was then obtained by fitting the hot-carrier-mediated reaction rates and the highest surface temperature (T_{hs}) measured by thermal camera using the Arrhenius equation, as shown in Figure 5.5a for examples of wavelength dependence of E_{app} for a fixed light intensity of 3.2 W/cm^2 (upper panel) and the intensity dependence of E_{app} for a fixed excitation wavelength of 550 nm (lower panel). In dark, the apparent activation barrier is 1.21 eV. While under illumination, the E_{app} decreases. When the excitation wavelength scanned from 700 nm to 550 nm, the reduction of E_{app} increased because the increase in optical absorption boosts the hot carrier generation. Especially at 550 nm, the wavelength most resonant with the LSPR of the $\text{Cu}_{19.5}\text{Ru}_{0.5}$ surface alloy NPs, the illumination led to the largest reduction of E_{app} , from 1.21 eV to 0.35 eV. For

shorter wavelengths ($\lambda < 550$ nm), the reduction in E_a was less substantial than light excitation at 550 nm, though the absorption was still high. Again this is because the interband transition predominates the absorption at the wavelength region of $\lambda < 550$ nm and hot carriers generated from interband transitions is less effective in activating surface reaction in this system⁸⁴. For illumination at 550 nm, E_{app} decreased with increasing the light intensity. A 3D contour mapping of the E_{app} to illumination intensities and wavelengths shows that the trend observed above are generally applicable to other wavelengths and intensities: 550 nm light excitation gives the largest reduction in E_{app} for all light intensities, and E_{app} decreases with increasing light intensity for all wavelengths studied. Under optimal illumination, at 550 nm and relatively high intensity of 4 W/cm^2 , E_{app} was reduced to ~ 0.27 eV.

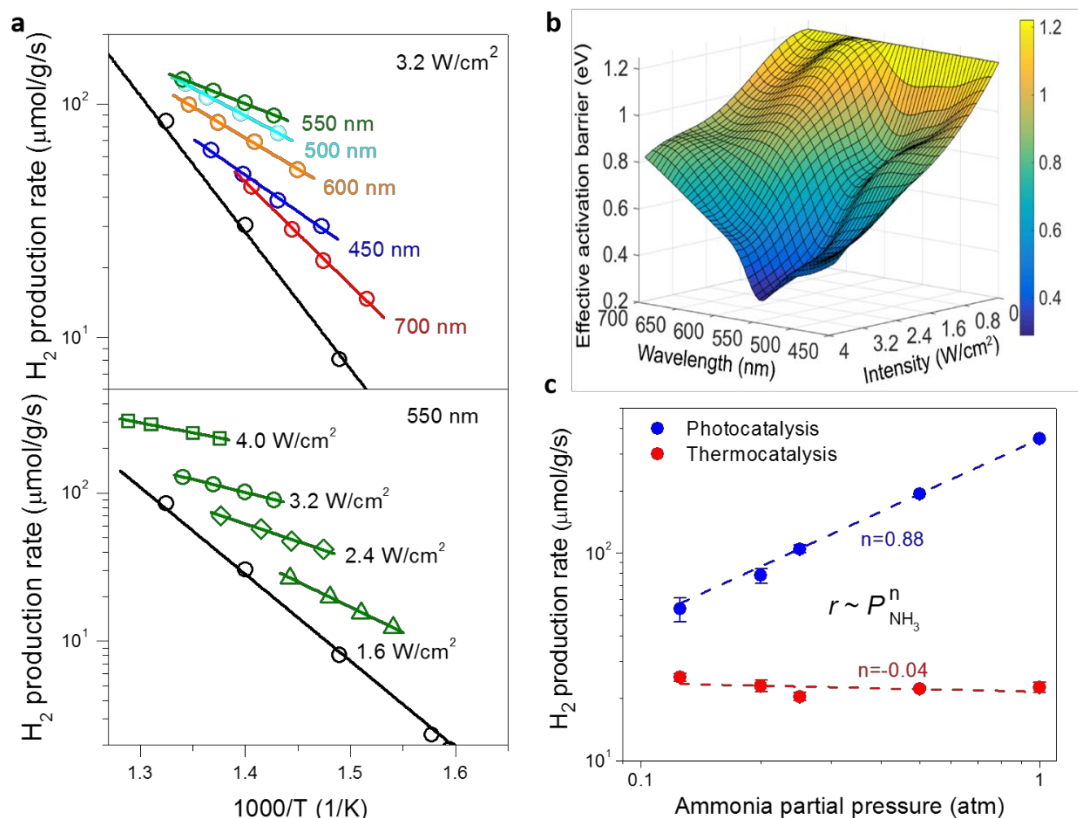


Figure 5.5 Light-dependent activation barrier and reaction order of ammonia. (a) Arrhenius plots of apparent activation barriers for different wavelengths under the constant intensity of 3.2 W/cm^2 (upper panel) and various light intensities at 550 nm (bottom panel). The black line represents thermocatalysis in the dark. (b) A 3D contour map of activation barrier for different wavelengths and intensities through interpolation of 46 data points. (c) Reaction order with respect to P_{NH_3} in photocatalysis (6.4 W/cm^2 white light) and thermocatalysis (427°C). r denotes the H_2 production rate while n represents the reaction order.¹⁶

The E_{app} of a reaction closely relates to the activation barrier of the rate-determining step (E_{a-RDS}) and the enthalpy required to clean active sites occupied by reaction intermediates⁸⁷. For ammonia decomposition on a Ru surface, there is two

possible rate-determining steps (RDS): (i) associative desorption of N_2 and (ii) N-H bond scissions⁸⁸⁻⁸⁹. At low temperatures and high ammonia partial pressures (P_{NH_3}), associative desorption of N_2 is the rate-determining step, characterized by an apparent activation barrier in the range of 1.5-2 eV and a zeroth reaction order of NH_3 in the rate equation⁸⁸⁻⁸⁹. The reaction intermediates, mostly N, adsorb on the surface and block the reaction sites for NH_3 absorption⁹⁰⁻⁹¹. With the increasing of temperature and/or decreasing of ammonia partial pressure, the rate-determining step will shift to N-H bond scission. Correspondingly, the reaction order of ammonia will increase to 1 while the apparent activation barrier decreases to ~ 0.2 eV, gradually⁸⁸⁻⁸⁹. For the thermocatalysis at 427 °C, the RDS is determined to be N_2 desorption. This is supported by the no dependence of reaction rate on the partial pressure of NH_3 and a high activation barrier of 1.21 eV. In contrast, for photocatalysis under 6.4 W/cm² white light illumination (surface temperature 403 °C), the reaction order of ammonia is 0.88 (Figure 5.5c). This increase in reaction order, along with a reduction in the apparent activation barrier under light illumination, suggests that hot carriers derived from plasmon decay modify the reaction kinetics by reducing the activation barrier for associative desorption of N_2 (E_{a-RDS}), while simultaneously decreasing the surface coverage of adsorbed intermediates. Both processes decrease E_{app} and lead to efficient plasmon-mediated NH_3 decomposition.

The reaction energetics of the ammonia decomposition is illustrated in Figure 5.6a. The two relevant reaction steps are indicated by (i) and (ii). The results from the experiments suggest that hot carriers significantly reduce the activation barrier

of associative desorption of N_2 . The E_{a-RDS} , and thus the E_{app} , can be reduced by activating the N_{ads} through hot carriers, in several ways, along with the reaction potential energy surface. Firstly, as the mechanism of electronic excitation, the hot carriers can weaken or directly break the Ru-N bond by transferring into its frontier orbital (red and yellow solid arrows in the Franck-Condon diagram inset in Figure 5.6a). However, this process requires energy resonance between the hot carriers and the acceptor levels of the activated bond. Once created by plasmon decay, the hot carriers will relax quickly toward the Fermi level through electron-electron scattering⁹². On the other hand, electron-phonon scattering can be substantial for localized vibrational modes involving charges heterogeneously distributed among atoms, such as the Ru-N surface species. This process does not require resonant conditions and can occur as long as the energies of hot carriers are higher than the vibrational quantum. Thus the Ru-N bond would be more likely activated through electron-vibrational scattering. Multiple vibrational excitations could also happen (blue solid arrows in the Franck-Condon diagram inset in Figure 5.6), and as the vibronic energy stored in the bond increases, the activation energy is reduced. Overall, both excitations (hot carrier transfer and electron-vibrational scattering) could facilitate the associative desorption of N_2 , which has been described previously as desorption induced by electronic transitions (DIET) on metal substrates under light excitation^{32, 93-94}. With more molecules excited to higher vibronic states by higher light intensities and/or closer-to-resonant photoexcitation, the activation barrier of associative desorption of N_2 decreases, and so does the apparent activation

barrier of the whole reaction. It is plausible that the $E_{a\text{-RDS}}$ reduced so much under high-intensity illumination (3.2 W/cm^2 at 550 nm) that the RDS shifted from N_2 desorption to N-H bond breaking. Note that Hot carrier-induced desorption of intermediates (Fig. 3B) would also contribute to the decrease of E_{app} by decreasing the coverage of intermediates and releasing the active sites.

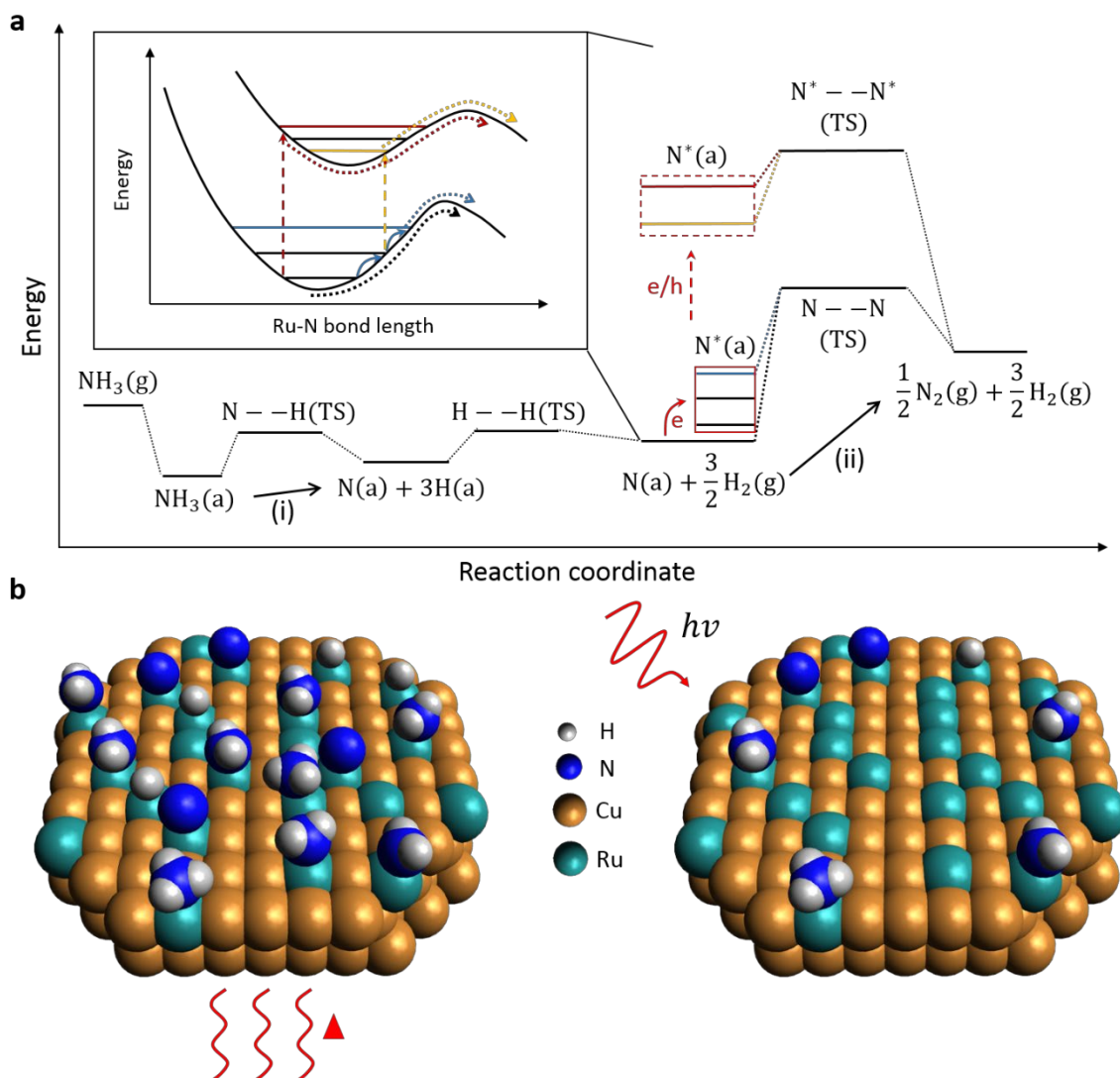


Figure 5.6 Mechanisms for hot-carrier-mediated reduction of activation barrier. **(A)** Schematic energetics of elementary reaction steps for NH_3 decomposition. The \ddagger denotes transition state, and the two relevant RDSs, N-H bond scission and associative desorption of N_2 , are labeled. N^* refers to excited Ru-N surface species: either vibronic levels in an excited electronic state (red dashed arrow and box) or vibrational excitations in the electronic ground state (red solid arrow and box). The activation barriers after excitation (red, yellow, and blue dotted lines) are all lower than that of the ground state (black dotted line). The Franck-Condon diagram inset illustrates the mechanisms in more detail. Dark red and yellow dashed arrows denote possible hot carrier transfer

into or electronic excitation of the Ru-N surface species. Blue solid arrows denote multiple vibrational excitations of the electronic ground state. e^- , electron; h^+ , hole. (B) Schematics of surface coverage under heating versus light-illumination conditions. In contrast to thermocatalysis (left), photocatalysis and hot carrier generation (right) can promote desorption of “poisoning” adsorbed intermediates. $h\nu$, light.¹⁶

5.3. Conclusion

In conclusion, we have introduced a light-dependent activation barrier for distinguishing hot carrier contributions from photothermal effects in plasmon-enhanced photocatalysis. In the plasmonic photocatalytic decomposition of ammonia, the apparent activation barrier depends strongly on both incident wavelength and light intensity. This dependence can be accounted for by hot carrier-induced associative desorption of N_2 , which simultaneously reduces the coverage of reaction intermediates, significantly decreasing the apparent activation barrier. A knowledge of the light-dependent activation barrier can be used to quantitatively predict photocatalytic reaction rates for given reaction conditions, such as illumination and external heating. The predictive and quantitative methodology presented here paves the way for optimization of plasmonic photocatalysis for energy efficient applications.

Coke-resistant methane activation by single-atom-alloy plasmonic photocatalysts

6.1. Methane activation

To produce the industrially important syngas (CO+H₂), methane dry reforming ($\text{CH}_4 + \text{CO}_2 \rightarrow 2\text{CO} + 2\text{H}_2$) has been long considered as a more environmentally friendly reaction compared to the currently applied methane steam reforming ($\text{CH}_4 + \text{H}_2\text{O} \rightarrow \text{CO} + \text{H}_2$) in industry, since it converts two greenhouse gases into valuable chemical feedstock⁹⁵. However, it is also quite challenging, since CO₂ is more inert than H₂O. Not only is dry methane reforming both kinetically and thermodynamically unfavorable, but it is also highly vulnerable to coke deposition and concomitant catalyst deactivation⁹⁶⁻⁹⁷. Although numerous catalysts have been explored, the conventional thermal-driven approach inevitably requires high temperatures (700-1000 °C) to achieve appreciable reaction rates and to mitigate coking^{95, 98}.

Given the ability to activate chemical reaction in milder conditions by light, Plasmonic photocatalysis potentially can achieve low-temperature activation of methane by photon excitation. Very recently, several bimetallic-alloy plasmonic photocatalysts (Au-Pd and Au-Pt) have been reported⁹⁹⁻¹⁰⁰ for light-activated methane drying reforming (MDR). However, their homogeneous alloy structure appeared to limit their performance, by highly damping the LSPR of plasmonic Au with the high loading of Pd or Pt and consequently compromising the absorption amplitude and hot carrier generation. They also exhibited low stability, probably because the adjacent active sites on the nanoparticle surfaces facilitate coke formation. In contrast, it has been shown that coke-resistance merit can be achieved with a single atom alloy structure¹⁰¹.

Here I developed a single-atom-alloy plasmonic photocatalyst from the surface alloy structure for achieving an efficient, stable and selective photocatalytic MDR process. Cu is used as the core antenna while atomic Ru sites are sparsely distributed on the Cu surface as the reactor.

6.2. Light-driven methane dry reforming with Ru-on-Cu single-atom-alloy photocatalysts

6.2.1. Synthesis and characterization of Cu-Ru single atom alloy

A series of Ru-on-Cu surface alloy NPs with different Ru loadings were prepared onto the MgO-Al₂O₃ composite support using the same procedure for

$\text{Cu}_{19.5}\text{Ru}_{0.5}$, with the concentrations of $\text{Cu}(\text{NO}_3)_2$ and RuCl_3 in the metal precursor solution varying accordingly for the desired loading of Ru. The photocatalysts are denoted as Cu_xRu_y , with x and y referring to the respective atomic percentage of Cu and Ru considering all the metal elements in the reactant mixture (Cu, Ru, Mg, and Al). The post-treatment, including annealing in He and reduction by H_2 , were performed at a higher temperature, $600\text{ }^\circ\text{C}$. All the Ru-on-Cu surface alloy NPs exhibit similar size distributions (Figure 6.1c-h) as the Cu NPs (Figure 6.1a-b), indicating a minimal perturbation of the Cu nanoparticle morphology due to the formation of the Cu-Ru surface alloy. Again I performed the N_2O chemisorption experiment to investigate the variation of the surface composition of Ru-on-Cu surface alloy samples with different Ru loadings, which was summarized in Table 6.1. For Ru-on-Cu surface alloys, the concentration of Cu_s decreased with increasing loading of Ru, suggesting the occupation of Ru on the surface of Cu NPs. Quantitatively, the calculated surface concentrations of Ru are close to the bulk concentration of Ru as determined by ICP-MS (Table 6.2), an indication of Ru enrichment on the surface of Cu NPs. As expected, UV-Vis diffuse reflectance spectra show an LSPR peak of Cu NP at $\sim 560\text{ nm}$ for all samples.

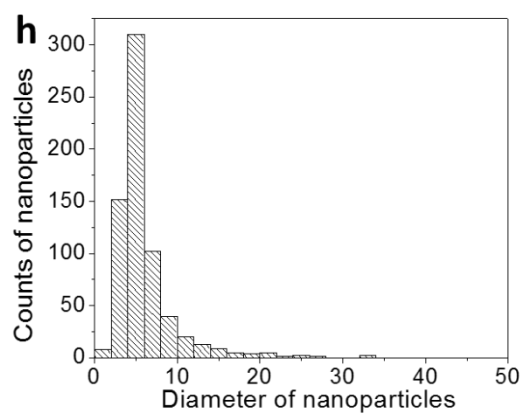
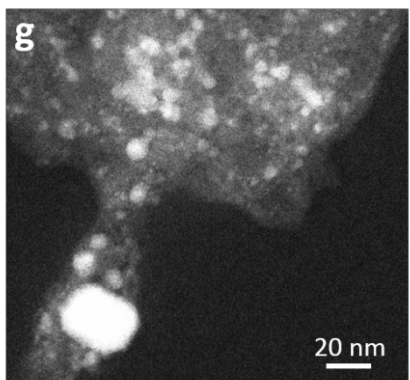
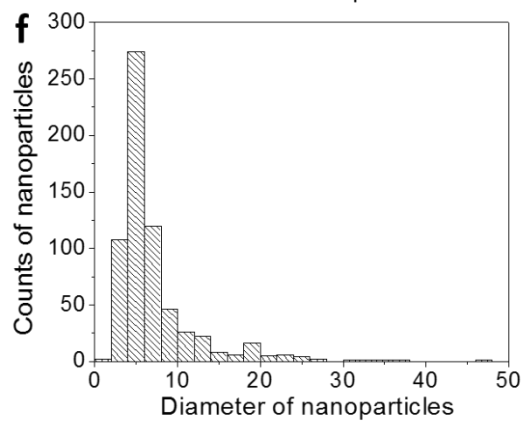
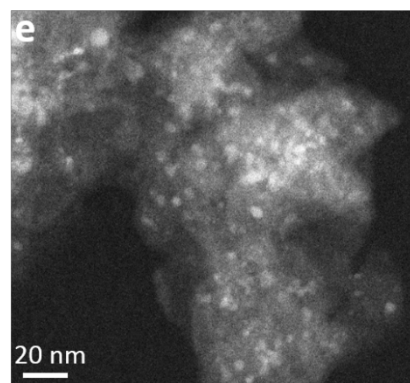
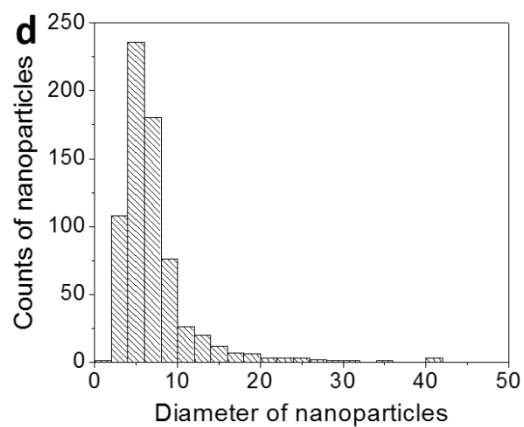
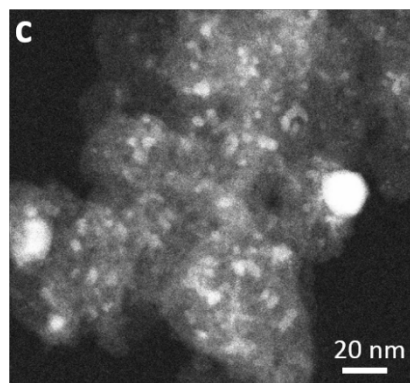
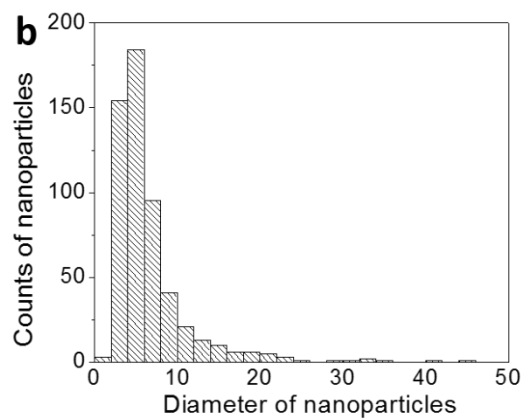
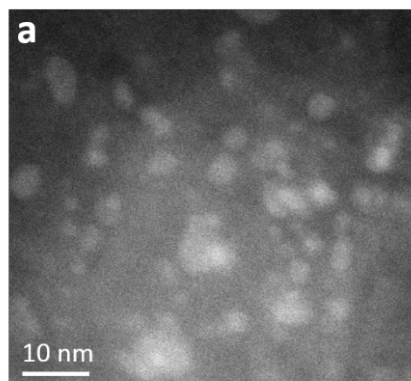


Figure 6.1 HAADF images and size distribution of (a,b) Cu_{20} NPs, (c,d) $\text{Cu}_{19.9}\text{Ru}_{0.1}$ surface alloy NPs, (e,f) $\text{Cu}_{19.8}\text{Ru}_{0.2}$ surface alloy NPs (g,h) $\text{Cu}_{19.5}\text{Ru}_{0.5}$ surface alloy NPs.

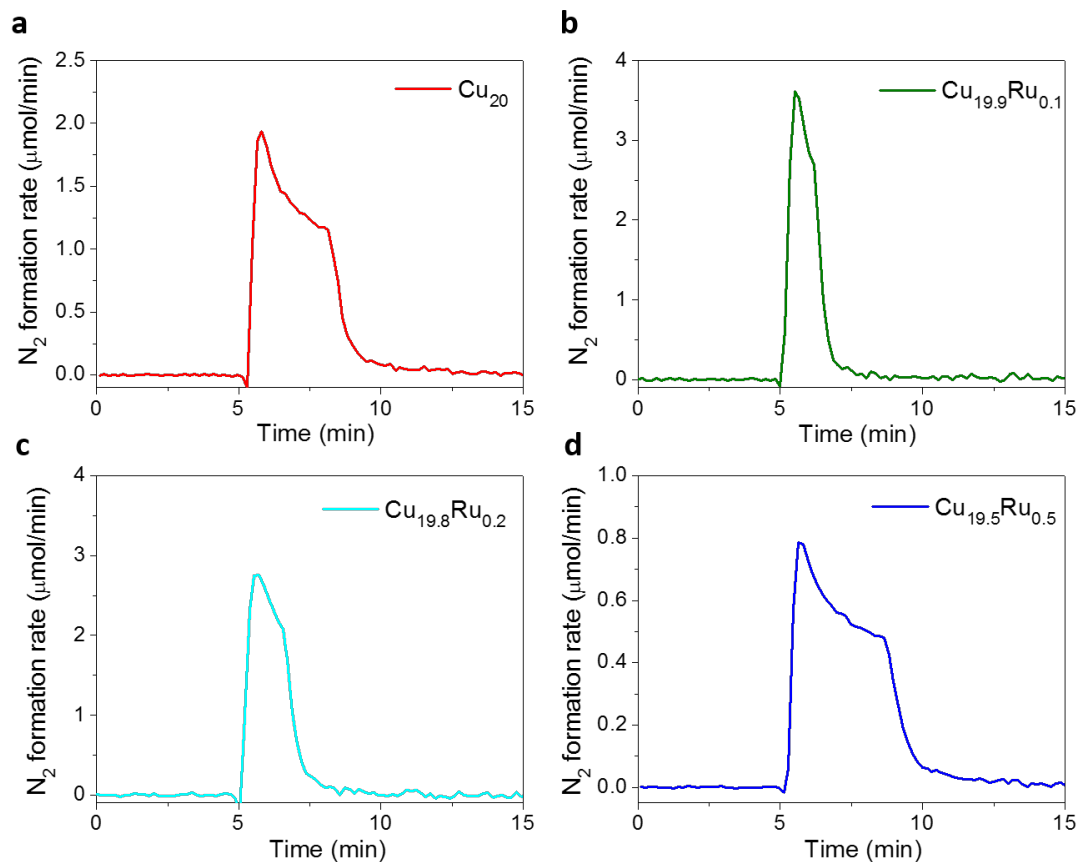


Figure 6.2 Representative N_2O dissociative chemisorption spectra of (a) Cu_{20} , (b) $\text{Cu}_{19.9}\text{Ru}_{0.1}$, (c) $\text{Cu}_{19.8}\text{Ru}_{0.2}$ and (d) $\text{Cu}_{19.5}\text{Ru}_{0.5}$. Desorbing N_2 is the measured reaction product. Note differences in scale of vertical axes.

Table 6.1 N₂O chemisorption experiment results

Samples	Mass* (g)	Integrated amount of released N ₂ (μmol)				Average amount (μmol)	Surface Cu concentration (μmol/g)	Calculated surface Ru concentration (μmol/g)
		1 st run	2 nd run	3 rd run	4 th run			
Cu ₂₀	0.1000	4.85	4.66	4.69	4.74	4.74	94.8	0**
Cu _{19.9} Ru _{0.1}	0.1022	4.25	4.23	4.16		4.21	82.4	12.4
Cu _{19.8} Ru _{0.2}	0.0950	3.24	3.05			3.14	66.2	28.6
Cu _{19.5} Ru _{0.5}	0.0997	2.07	2.37	2.33		2.26	45.3	49.5

* mass of catalyst precursor

** Assumed to be zero since no Ru was added for Cu₂₀ sample during synthesis

Table 6.2 Element concentration determined from ICP-MS

Sample	Metal element concentration	
	Cu (mmol/g)	Ru (μmol/g)
Cu ₂₀	1.936	0.00
Cu _{19.95} Ru _{0.05}	1.866	5.76
Cu _{19.9} Ru _{0.1}	1.844	12.6
Cu _{19.8} Ru _{0.2}	1.951	23.5
Cu _{19.5} Ru _{0.5}	1.794	56.5

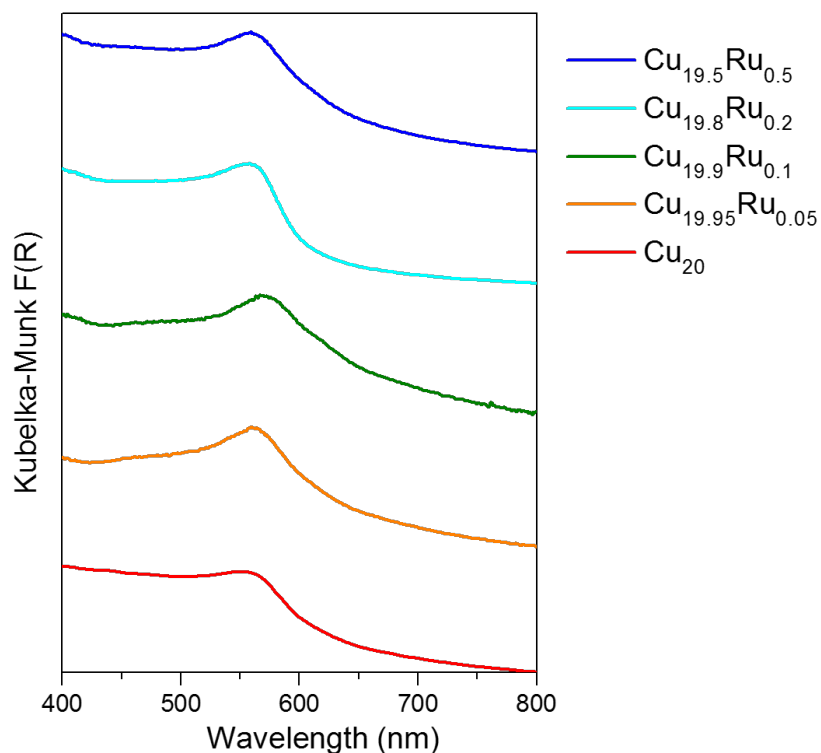


Figure 6.3 UV-Vis diffuse reflectance spectra of CuRu surface alloy samples. Reflectance was transformed to absorption through Kubelka-Munk transformation¹⁰², $F(R) = \frac{(1-R_\infty)^2}{2R_\infty}$

6.2.2. Photocatalytic performance of Ru-on-Cu surface alloys with different Ru loading for methane dry reforming

The photocatalytic methane dry reforming reaction was tested for Cu NPs as well as all the surface alloy samples under 19.2 W/cm² white-light laser (SC-400-8) illumination without external heating. The flow rate of CH₄ and CO₂ were set to 8 sccm

each. The effluents were analyzed by a gas chromatograph (Shidmazu-2014). H₂ and CO were separated by a Shincarbon packed column (Restek, 60/80 mesh, 1/16" OD, 2m) and detected by a pulsed discharge helium ionization detector (PDHID), while CH₄ was separated by a Rt®-Q-BOND capillary column (Restek, 0.53 mmID, 20 μ m, 30 m) and detected by a flame ionization detector (FID).

The reaction rate, stability, and selectivity all change substantially with the Ru loading (Figure 6.4). For pure Cu NPs, an initial reaction rate of $\sim 50 \mu\text{mol CH}_4\cdot\text{g}^{-1}\cdot\text{s}^{-1}$ was achieved, but the activity quickly decayed to only $\sim 4 \mu\text{mol}\cdot\text{g}^{-1}\cdot\text{s}^{-1}$ after 5 h (Figure 6.4a, red). The decrease in activity was attributed to coke deposition, as carbon nanofibers were observed in the used sample by TEM (Figure 6.6a-c) and identified as graphitic carbon by Raman spectroscopy (Figure 6.5a). The size of NPs also increased (Figure 6.6d-e)

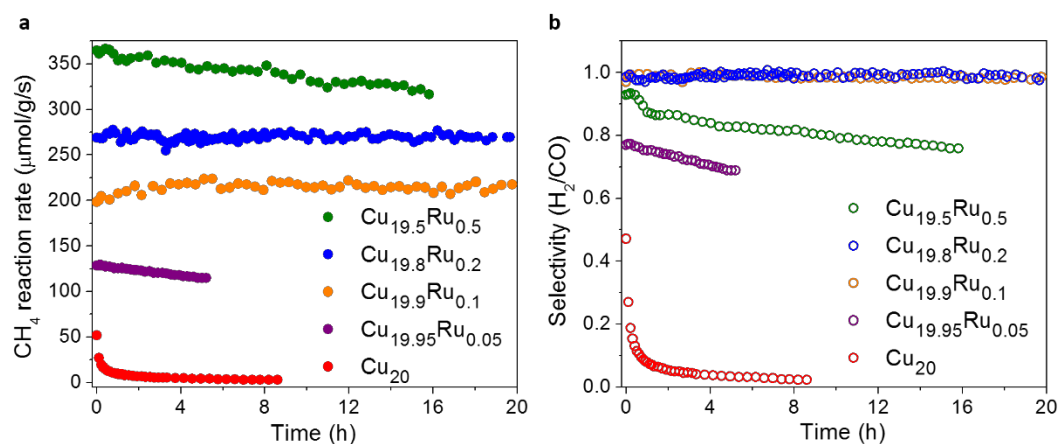


Figure 6.4 Effect of ruthenium loading on the photocatalytic behavior of Ru-on-Cu surface alloy NPs. (a) Reaction rate and long-term stability as a function of

Ru loading of the photocatalyst nanoparticles. (b) Selectivity of photocatalytic MDR reaction under $19.2 \text{ W}\cdot\text{cm}^{-2}$ white light illumination. The reactor was kept at room temperature, and selectivity is defined as the ratio of the formation rate of H_2 to CO

Introducing a trace amount of Ru ($\text{Cu}_{19.95}\text{Ru}_{0.05}$, Figure 6.4a, purple) increases the initial photocatalytic efficiency to $\sim 128 \mu\text{mol}\cdot\text{g}^{-1}\cdot\text{s}^{-1}$, and dramatically improves the stability, with $\sim 90\%$ of the initial activity remaining after the continuous 5-h experiment. Correspondingly, less coke was formed as weaker Raman features of graphitic carbon were observed (Figure 6.5b) compared to the Cu_{20} sample. Slightly increasing the Ru loading to $\text{Cu}_{19.9}\text{Ru}_{0.1}$ (Figure 6.4a, orange) and $\text{Cu}_{19.8}\text{Ru}_{0.2}$ (Figure 6.4a, blue) further enhances the photocatalytic rate and provides better stability, with 100% performance maintained over a 20-h photocatalytic reaction. The stability of these catalysts was attributed to their coke-resistance merit since there is a lack of detectable graphitic carbon in the Raman spectra of the samples after use (Figure 6.5c-d).

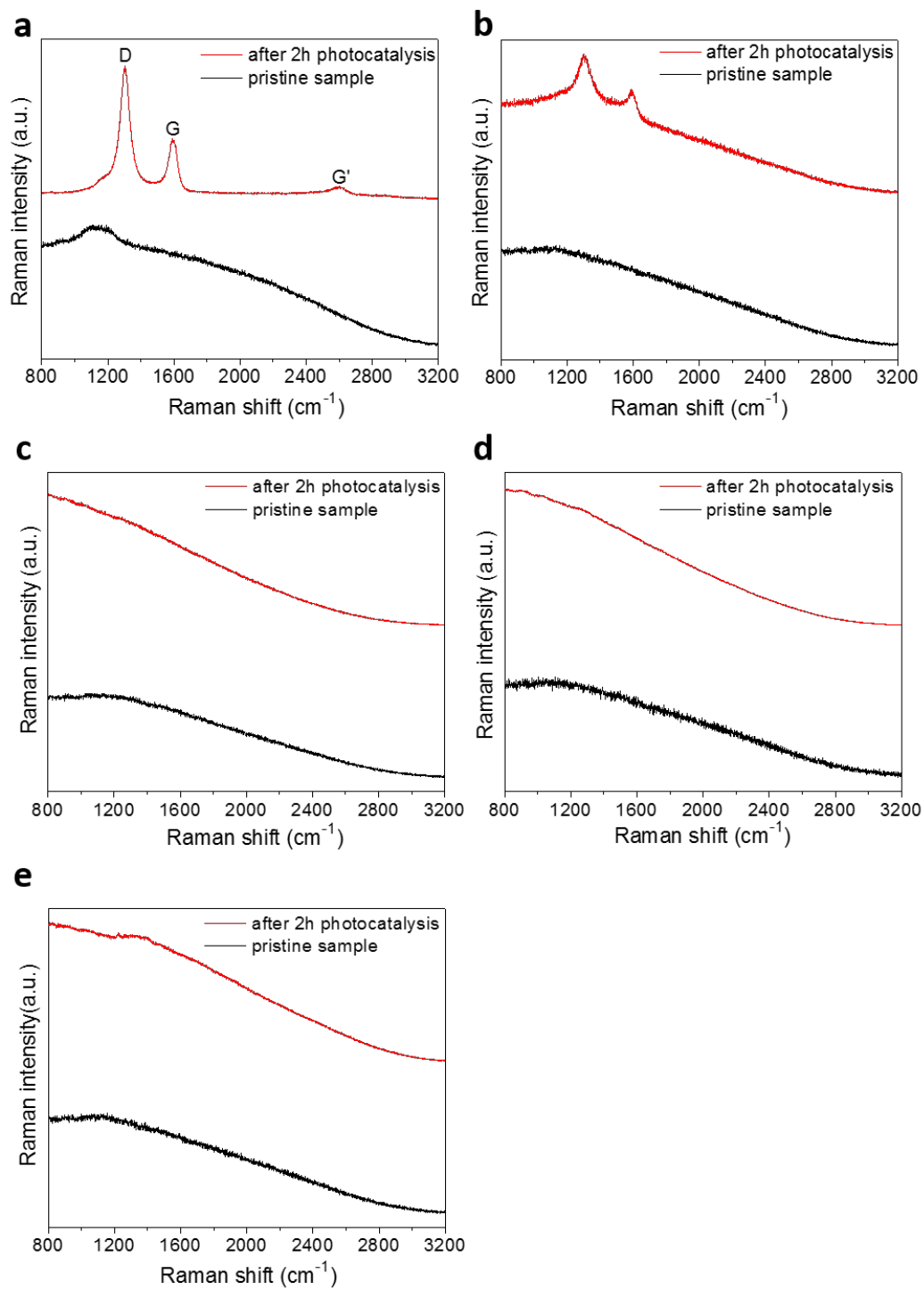


Figure 6.5 Raman spectra at the spot of light illumination before (black lines) and after (red lines) 2h photocatalysis under $19.2 \text{ W}\cdot\text{cm}^{-2}$ white light

illumination for samples of (A) Cu₂₀, (B) Cu_{19.95}Ru_{0.05}, (C) Cu_{19.9}Ru_{0.1}, (D) Cu_{19.8}Ru_{0.2} and (E) Cu_{19.5}Ru_{0.5}.

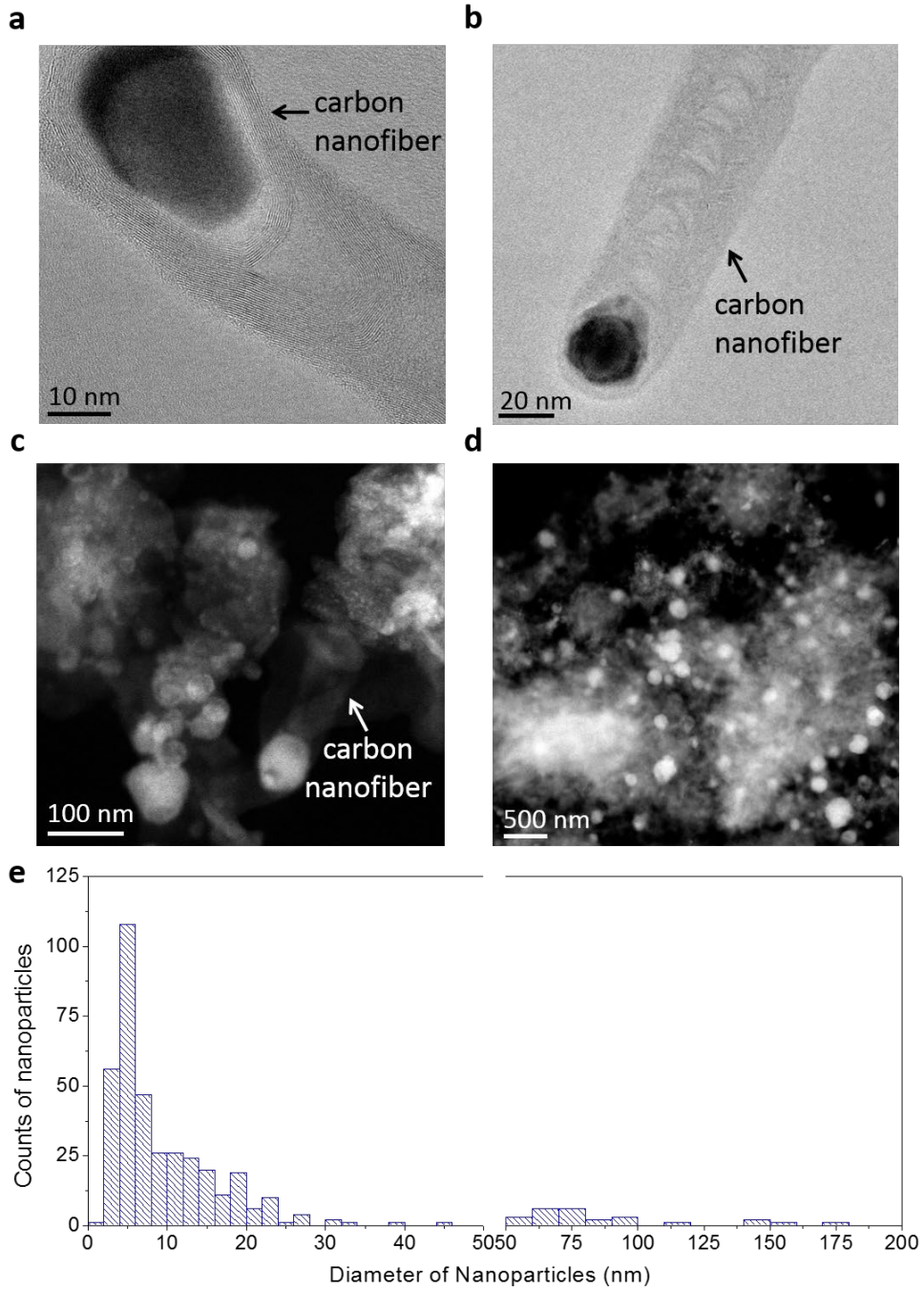


Figure 6.6 (a-b) HR-TEM images, (c-d) HAADF images and (e) size distribution of Cu NPs in Cu₂₀ sample after 2h photocatalysis under 19.2 W/cm² while-light illumination.

Further increasing Ru loading (Cu_{19.5}Ru_{0.5}) compromises the stability, with 13% of photocatalytic activity lost after a 16-h reaction (Figure 6.4a, green), though gives a higher initial photocatalytic rate. The coking rate on Cu_{19.5}Ru_{0.5} was slower than that on Cu₂₀ and Cu_{19.95}Ru_{0.05} samples since the Raman peaks of graphitic species in the Cu_{19.5}Ru_{0.5} sample after use were hardly observable (Figure 6.5e). I attributed the trend of stability with the Ru loading to the formation of atomically dispersed Ru sites on Cu surface at Ru loading below 0.2%. The atomically dispersed Ru sites strongly anchor C with a high barrier for C diffusion, as supported by the DFT calculation (Figure 6.7a), therefore isolate the surface carbon intermediates and suppress coke formation (Figure 6.7, middle panel). In contrast, the surface concentration of Ru is too high in Cu_{19.5}Ru_{0.5} sample such that Ru islands formed. Neighboring Ru sites will facilitate polymerization of surface carbon intermediates by virtue of their proximity (Figure 6.7b, left panel). While for the Cu_{19.95}Ru_{0.05} sample, though atomic dispersion of Ru also formed, the surface coverage of Ru was too low and a substantial part of the reaction was catalyzed by the exposed Cu surface, which is vulnerable to coking (Figure 6.7b, right panel).

Except for H₂ and CO, no other hydrocarbons or oxygenates were produced from the photocatalytic MDR reaction. Apart from coking, the reverse water gas shift (RWGS) reaction ($\text{CO}_2 + \text{H}_2 \rightarrow \text{CO} + \text{H}_2\text{O}$) is likely to be the only side reaction. Thus we

define the selectivity as the ratio of formation rate of H₂ to CO ($S = r_{H_2}/r_{CO}$). The Cu₂₀ sample shows a very low selectivity as it is widely recognized that Cu exhibits good catalytic activity towards RWGS reaction¹⁰³. Covering the Cu surface with Ru greatly

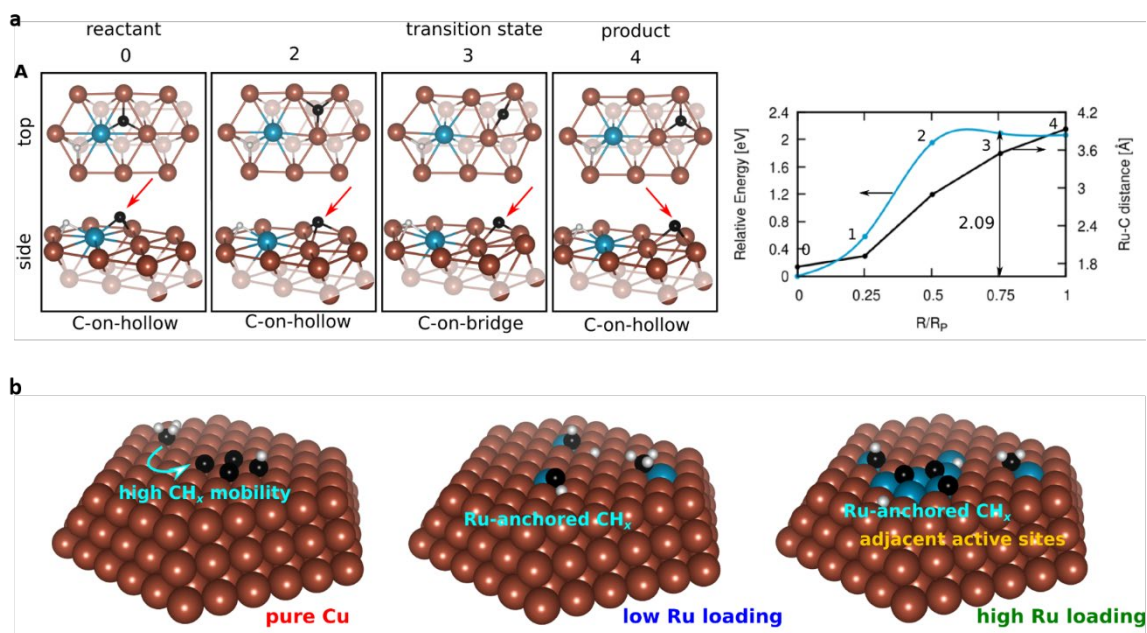


Figure 6.7. (a) DFT calculation for C diffusion away from Ru. Pathway for C diffusion away from Ru onto a Cu₃ fcc-hollow site via a Cu-Cu bridge-site transition state. Red arrows point to the diffusing C. Corresponding MEPs is shown in the right panel with the barriers marked. (b) Schematics of the compositional dependence of the Cu_xRu_y photocatalysts with respect to coke resistance.

increases the selectivity by suppressing the RWGS reaction. Especially, the Cu_{19.9}Ru_{0.1} and Cu_{19.8}Ru_{0.2} exhibit selectivity close to 1. High selectivity of MDR reaction is extremely beneficial, for example, in Fischer-Tropsch synthesis¹⁰⁴, as further adjustment of the H₂/CO ratio via the high-temperature water gas shift reaction (CO

+ H₂O → H₂ + CO₂) is not necessary anymore. Higher loading of Ru (Cu_{19.5}Ru_{0.5}) is also unfavorable to selectivity. This is most likely caused by the longer residence of adsorbed H (H^{ads}) on the Ru-rich surface due to the stronger interaction between H^{ads} and Ru, resulting in a higher probability for H^{ads} to react with adsorbed oxygen (O^{ads}).

6.2.3. Photo- vs. thermo- catalysis on the single-atom-alloy catalyst with Cu_{19.8}Ru_{0.2} composition

From considerations of efficiency, stability, and selectivity, the best overall photocatalytic performance is provided by the Cu_{19.8}Ru_{0.2} composition. I further investigated the thermocatalytic performance of Cu_{19.8}Ru_{0.2} and compared it to the photocatalytic results to reveal how hot carriers modulate the reaction selectivity and stability.

The initial thermocatalytic rate for MDR on Cu_{19.8}Ru_{0.2} sample at 1000 K in the dark was ~ 60 μmol CH₄·g⁻¹·s⁻¹ (Figure 6.8a). Since the maximum surface temperature under 19.2W/cm² white light excitation is ~1000 K, but the photocatalytic reaction rate (~275 μmol CH₄·g⁻¹·s⁻¹) was more than 4 times of the thermocatalytic rate at 1000 K, I propose that hot-carrier-mediated chemical reaction to be the primary mechanism in photocatalytic MDR reaction. Moreover, when the reaction was performed in the dark, the thermocatalytic reaction rate decayed quickly to be less than 10% of initial rate after an 8-h reaction. The contrast difference in stability between photocatalysis and thermocatalysis correlates to their sharp difference in selectivity (Figure 6.8b vs. Figure 6.8d). In photocatalysis, the associative desorption

of H₂ is enhanced by hot carriers through the desorption induced by electronic transitions (DIET) mechanism¹⁰⁵, as reflected by the high photocatalytic selectivity, resulting in a scarce abundance of H^{ads}. Thus this DIET process will suppress the consumption of O^{ads} by H^{ads}, and maintains a high concentration of reactive O^{ads} for removal of adsorbed C (C^{ads}) through oxidative gasification (C^{ads} + O^{ads} → CO (*g*)). On the other hand, the low selectivity of the thermocatalytic reaction indicates that H^{ads} inclines to react with CO₂ and decreases the abundance of O^{ads}, enabling coke formation.

The selectivity of photocatalytic MDR increases monotonically with light intensity, consistent with the DIET mechanism, and reaches ~ 100% for intensities above ~10 W·cm⁻² (Figure 6.8b). In contrast, thermocatalytic selectivity shows a V-shaped dependence on temperature, with a minimum (<10% H₂/CO) occurring at a transition temperature of ~ 800 K (Figure 6.8d). This dramatic difference confirms the dominant role of hot-carrier-mediated mechanism in photocatalysis. The V-shaped dependence of selectivity in thermocatalysis is caused by a transition from an

initial kinetically controlled to a thermodynamically controlled regime with

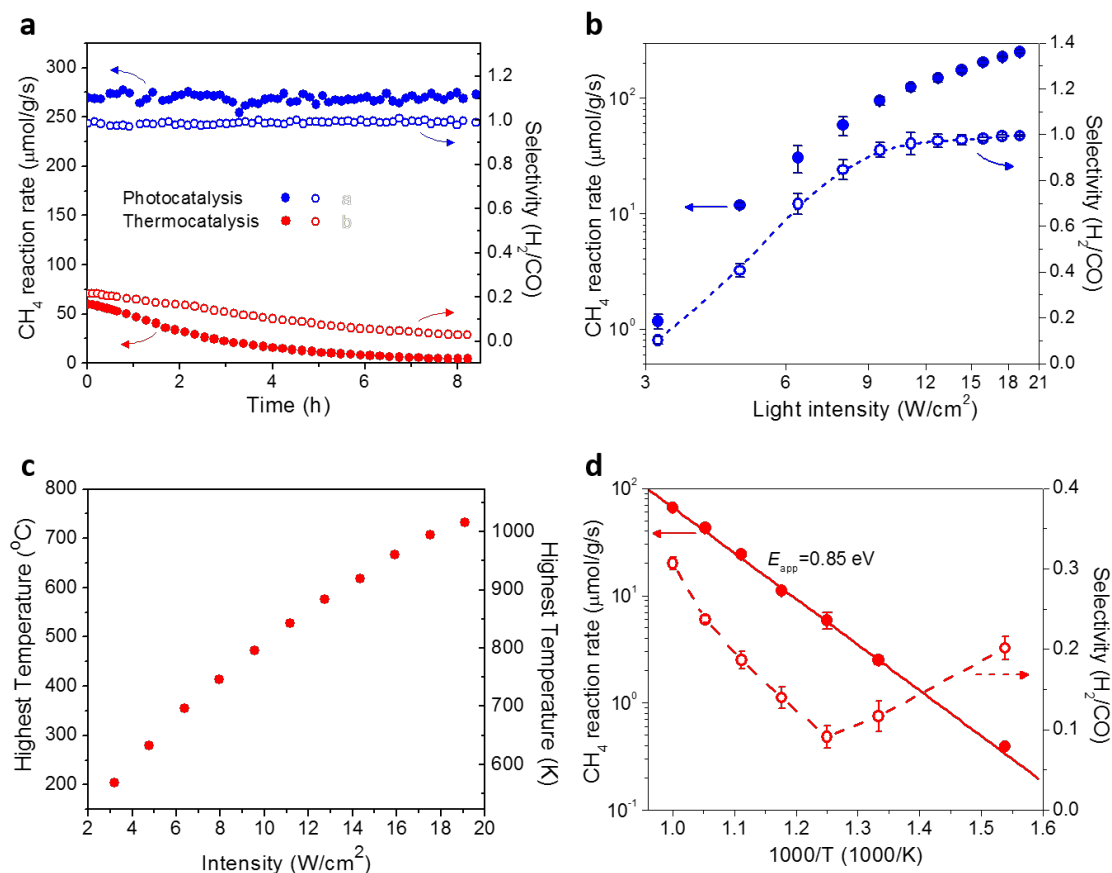


Figure 6.8 Photo- and thermo-catalytic characterization of the Cu_{19.8}Ru_{0.2} catalyst for methane dry reforming. (a) Long-term stability (filled circles) and selectivity (open circles) for photocatalysis under 19.2 W·cm⁻² white light illumination (blue circles) and thermocatalysis at 1000 K reactor temperature (red circles). (b) Light intensity dependence of reaction rate and selectivity in photocatalysis. Error bars represent the standard deviation (σ_{std}) of measurements of three different batches of the sample. (c) Light intensity dependence of the highest surface temperature (T_{hs}) on sample pellet. (d) Temperature dependence of reaction rate and selectivity in thermocatalysis.

Error bars represent the σ_{std} of measurements of two different batches of sample.

increasing temperature. Initially, the selectivity decreases because the RWGS reaction rate increases faster with temperature than the MDR reaction. At higher temperatures ($T > 800$ K), the RWGS reaction reached equilibrium due to its fast reaction rate. The $\Delta_r G$ of the RWGS reaction decreases with increasing temperature, shifting its equilibrium toward the reactants, and thus limit the reaction rate (see Appendix C). The predicted lower limit of the selectivity by thermodynamics reproduces the experimental values quite well (Table 6.3).

Table 6.3 Calculated selectivity of thermocatalysis based on data from NIST database¹⁰⁶

T (K)	$\Delta_r G$ (kJ/mol)	K	α ($\mu\text{mol/s}$)	β ($\mu\text{mol/s}$)	S (theory)	S (experiment)
800	9.565	0.2374	0.0442	0.0721	0.102	0.913
850	7.878	0.3280	0.0832	0.128	0.131	0.140
900	6.222	0.4354	0.182	0.248	0.191	0.186
950	4.595	0.5589	0.320	0.395	0.237	0.237
1000	3.071	0.6911	0.493	0.562	0.273	0.307

6.2.4. Energy efficiency and reaction conversion consideration

The energy efficiency and methane conversion by photocatalysis on $\text{Cu}_{19.8}\text{Ru}_{0.2}$ were studied. Under white light illumination, the energy efficiency increased with light intensity, reaching a plateau of $\sim 15\%$ at the intensities above $16 \text{ W}\cdot\text{cm}^{-2}$ (Figure 6.9a).

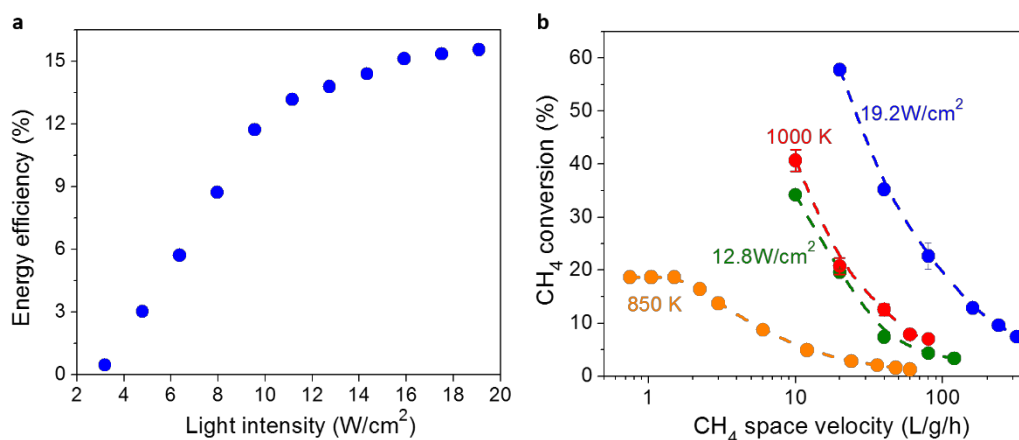


Figure 6.9 Photocatalytic energy efficiency and the methane conversion of $\text{Cu}_{19.8}\text{Ru}_{0.2}$. (a) Light-to-chemical energy efficiency of photocatalysis as a function of white light intensity. (b) Methane conversion by photocatalysis (blue and olive) and thermocatalysis (red and orange) as a function of space velocity, defined as the volumetric flow rate of the reactants divided the mass of the catalyst. Error bars represent the σ_{std} of measurements of two different batches of the sample.

For a highly endothermic reaction ($\Delta H_r \gg 0$) with a positive reaction entropy ($\Delta S_r > 0$), like MDR, thermodynamic equilibrium severely limits the conversion of reactants in thermocatalysis⁹⁸. In our experiment, the methane conversion by thermocatalysis

at 850 K reached a saturated value of only $\sim 20\%$ when the space velocity (SV) is below $1.5 \text{ L}\cdot\text{g}^{-1}\cdot\text{h}^{-1}$ (Figure 6.9b). In contrast, photocatalysis performed under $12.8 \text{ W}\cdot\text{cm}^{-2}$ white light illumination, with the T_{hs} close to 850K (Figure 6.9b), achieved a $\sim 35\%$ methane conversion, with no conversion limit observed yet even for SVs as high as $10 \text{ L}\cdot\text{g}^{-1}\cdot\text{h}^{-1}$. Photocatalysis under $19.2 \text{ W}\cdot\text{cm}^{-2}$, with T_{hs} at $\sim 1000 \text{ K}$, also achieved higher conversion than thermocatalysis at 1000 K for all the SVs investigated. This result shows that hot-carrier-mediated reactions can overcome the thermodynamic limit and provide an approach for low-temperature catalysis of industrially relevant reactions with high positive reaction enthalpy.

Concentrated solar power (CSP) is an industrially available sunlight-focusing technology that has been applied to MDR based on purely photothermal effects¹⁰⁷⁻¹⁰⁸. Generally, high light intensities (>400 suns), and consequently high temperatures ($>1000 \text{ K}$) are needed to achieve useful energy efficiencies and conversion rates. High energy efficiency of $\sim 50\%$ and conversion of $\sim 73\%$ with 180-suns intensity has been reported by designing a porous metal foam structure with low thermal conductivity to achieve high temperature ($\sim 1200 \text{ K}$) at relatively low light intensity¹⁰⁹. However, a high loading of Ru-based catalyst (5 wt% Ru) was used with a TOF of only $\sim 0.15 \text{ mol H}_2\cdot(\text{mol Ru})^{-1}\cdot\text{s}^{-1}$, which is well below the TOF of $34 \text{ mol H}_2\cdot(\text{mol Ru})^{-1}\cdot\text{s}^{-1}$ achieved in our system. Note that our results were achieved without any optimization of the catalyst structure and reactor design to better engineer the thermal conductivity and mass diffusion. Our discovery provides a practical, stable and sustainable route for syngas production from methane using lower noble-metal loadings and light

intensities, and therefore has potentially lower costs, for both of the catalyst and the reactor system.

6.3. Conclusion

I showed that single-atom-alloy plasmonic photocatalysts composed of a Cu NP antenna with atomically distributed Ru sites achieved photocatalytic MDR with high efficiencies, selectivities, and greatly suppressed coking at low temperature. Hot-carrier generation is the predominant mechanism in photocatalytic MDR, resulting in dramatically different behavior from the thermally driven reaction. Plasmon-mediated DIET greatly enhances the H₂ desorption and the atomic Ru sites effectively anchor and isolate the carbon intermediates, which together make the photocatalyst better resistant to coking compared to conventional catalysts. Since the photocatalyst is primarily composed of inexpensive and abundant Cu, this work may pave the way for low-temperature methane-reforming reactions for H₂ production using with sustainable light energy.

Appendix C

Explanation of temperature dependence of selectivity in thermocatalytic MDR reaction

At low temperatures ($T < 800$ K), the conversion of both the MDR and the RWGS reactions is low. Thus the reaction rates are in the kinetically controlled regime and can be determined from the rate law,

$$r = A \cdot e^{-E_{app}/k_b T} \cdot P_{R1}^a \cdot P_{R2}^b,$$

where A is the pre-exponential factor, P_{R1} , P_{R2} the partial pressures of the reactants and a , b are their reaction orders.

Thus we have,

$$\begin{aligned} S = \frac{r_{H_2}}{r_{CO}} &= \frac{2\alpha - \beta}{2\alpha + \beta} = \frac{2r_{MDR} - r_{RWGS}}{2r_{MDR} + r_{RWGS}} = \frac{2 - \frac{r_{RWGS}}{r_{MDR}}}{2 + \frac{r_{RWGS}}{r_{MDR}}} \\ &= \frac{2 - \frac{A_{RWGS}}{A_{MDR}} \cdot \exp\left(\frac{-E_{app,RWGS} + E_{app,MDR}}{RT}\right) \cdot \frac{P_{H_2}^a \cdot P_{CO_2}^b}{P_{CH_4}^c \cdot P_{CO_2}^d}}{2 + \frac{A_{RWGS}}{A_{MDR}} \cdot \exp\left(\frac{-E_{app,RWGS} + E_{app,MDR}}{RT}\right) \cdot \frac{P_{H_2}^a \cdot P_{CO_2}^b}{P_{CH_4}^c \cdot P_{CO_2}^d}} \end{aligned}$$

Kinetic measurements showed that the apparent activation barrier of the MDR and RWGS reactions are 0.85 and 0.77 eV, respectively (Figure 6.10). The partial pressures of CH_4 and CO_2 can be regarded as constant since the conversion of the MDR reaction is low (only $\sim 0.5\%$ at 800 K). On the other hand, the partial pressure of H_2 is proportional to the reaction rate of MDR approximately ($P_{H_2} \propto B \cdot r_{MDR}$, with B as a coefficient), since it is one of the products of the MDR reaction. For the RWGS reaction on supported Cu catalysts, the reaction order of H_2 (a) is ~ 1 in a CO_2 -rich environment¹⁰³. Thus, we have

$$P_{H_2}^a \propto r_{MDR} \propto A_{MDR} \cdot \exp(-E_{app,MDR}/RT) \cdot P_{CH_4}^c \cdot P_{CO_2}^d$$

$$\text{Furthermore, } \frac{A_{RWGS}}{A_{MDR}} \cdot \exp\left(\frac{-E_{app,RWGS} + E_{app,MDR}}{RT}\right) \cdot \frac{P_{H_2}^a \cdot P_{CO_2}^b}{P_{CH_4}^c \cdot P_{CO_2}^d} \propto A_{RWGS} \cdot$$

$\exp(-E_{app,RWGS}/RT) \cdot P_{CO_2}^b$, increases with T. Therefore, S will decrease with increasing temperature.

At high temperature (T>800 K), we assume that the RWGS side reaction reached equilibrium since the reaction rate of the RWGS reaction is much faster than the MDR reaction (Figure 6.10). This is similar to the quasi-equilibrium assumption for non-rate-limiting elementary steps in reaction kinetics analysis but here applied to two sequential reactions. Using the thermochemistry data and equations in NIST database (<https://webbook.nist.gov/chemistry/>), we calculate the reaction Gibbs free energy change and equilibrium constants (Table 6.1 Table 6.3 Calculated selectivities of thermocatalysis based on data from NIST database⁸⁹) of the RWGS reaction at different temperatures according to the following formulas:

$$H_T^0 = A \cdot T + B \cdot T^2/2 + C \cdot T^3/3 + D \cdot T^4/4 - E/T + F$$

$$S_T^0 = A \cdot \ln(T) + B \cdot T + C \cdot T^2/2 + D \cdot T^3/3 - E/(2 \cdot T^2) + G$$

$$\Delta_r H_T = \sum_{\text{product } i} c_i \cdot H_{T,i}^0 - \sum_{\text{reactant } j} c_j \cdot H_{T,j}^0$$

$$\Delta_r S_T = \sum_{\text{product } i} c_i \cdot S_{T,i}^0 - \sum_{\text{reactant } j} c_j \cdot S_{T,j}^0$$

$$\Delta_r G_T = \Delta_r H - T \cdot \Delta_r S$$

$$K_T = \exp\left(-\Delta_r G_T/RT\right).$$

In these equations H_T^0 and S_T^0 represent the standard enthalpy and entropy of chemicals at temperature T; $\Delta_r H_T$, $\Delta_r S_T$, $\Delta_r G_T$ and K_T are the reaction enthalpy change, reaction entropy change, reaction Gibbs free energy change and equilibrium constant at temperature T; c_i and c_j are the stoichiometric coefficients of products and reactants; R is the gas constant. The constants A to G of chemicals involved in

MDR and RWGS reactions are obtained from NIST database and k_b is the Boltzmann constant.

Minimal selectivity happens when the RWGS reaction reaches equilibrium,

$$K_{T,RWGS} = \exp\left(-\Delta_r G_{T,RWGS}/RT\right) = \frac{[P_{H_2O}] \cdot [P_{CO}]}{[P_{H_2}] \cdot [P_{CO_2}]},$$

where $[P_i]$ is the equilibrium partial pressure of species i in units of atmospheres.

As the feed flows of CH₄ and CO₂ were both 8 sccm, which corresponds to 5.95 μmol/s, the steady-state flow rates of CO₂, H₂, CO, and H₂O are 5.95-α-β, 2α-β, 2α+β and β, respectively, with α and β being the reaction rates of the MDR and RWGS reactions. Thus, we have

$$K_{T,RWGS} = \frac{(2\alpha + \beta) \cdot \beta}{(5.95 - \alpha - \beta) \cdot (2\alpha - \beta)}.$$

With the measured methane reaction rate (α) and calculated $K_{T,RWGS}$, we can solve for a positive β.

Finally, the theoretical minimal possible selectivity at different temperatures are calculated according to the following equation

$$S = \frac{r_{H_2}}{r_{CO}} = \frac{2\alpha - \beta}{2\alpha + \beta}$$

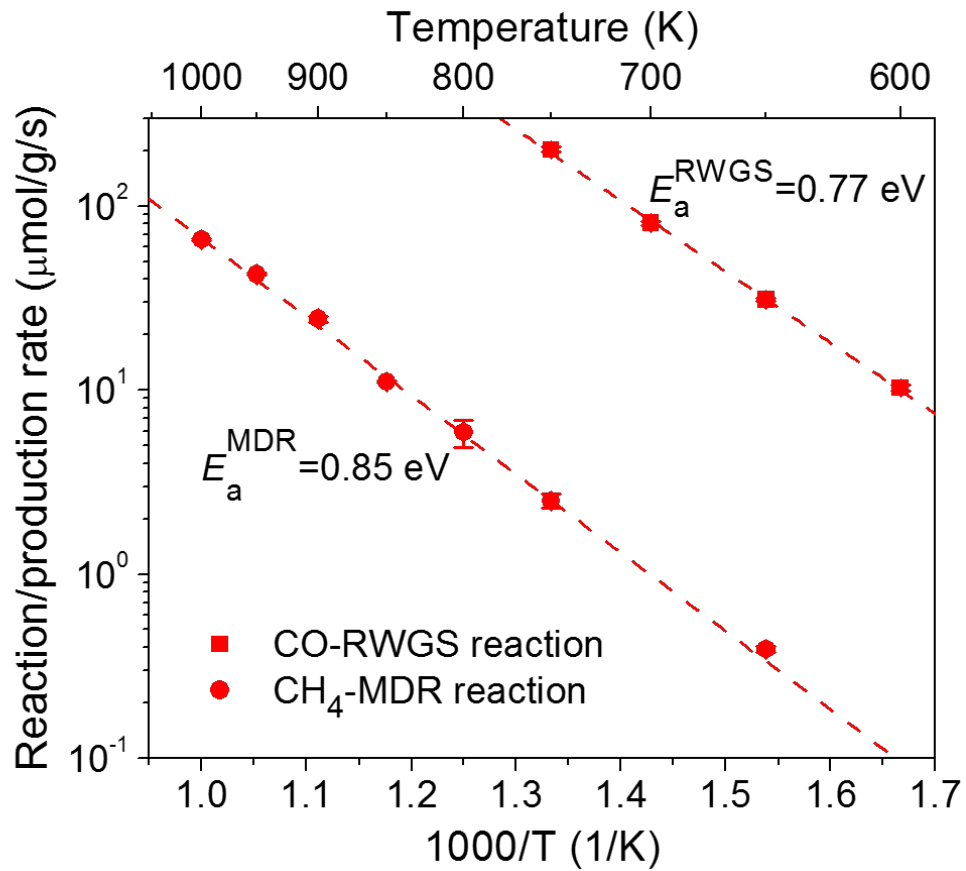


Figure 6.10 Arrhenius fitting of thermocatalytic MDR and RWGS reactions on Cu_{19.8}Ru_{0.2}

Reference

1. Zhang, Y.; He, S.; Guo, W.; Hu, Y.; Huang, J.; Mulcahy, J. R.; Wei, W. D., *Chemical Reviews* **2018**, *118* (6), 2927-2954.
2. Mukherjee, S.; Libisch, F.; Large, N.; Neumann, O.; Brown, L. V.; Cheng, J.; Lassiter, J. B.; Carter, E. A.; Nordlander, P.; Halas, N. J., *Nano Letters* **2013**, *13* (1), 240-247.
3. Mukherjee, S.; Zhou, L.; Goodman, A. M.; Large, N.; Ayala-Orozco, C.; Zhang, Y.; Nordlander, P.; Halas, N. J., *Journal of the American Chemical Society* **2014**, *136* (1), 64-67.
4. Christopher, P.; Xin, H.; Linic, S., *Nature Chemistry* **2011**, *3*, 467.
5. Marimuthu, A.; Zhang, J.; Linic, S., *Science* **2013**, *339* (6127), 1590.
6. Zhou, L.; Zhang, C.; McClain, M. J.; Manjavacas, A.; Krauter, C. M.; Tian, S.; Berg, F.; Everitt, H. O.; Carter, E. A.; Nordlander, P.; Halas, N. J., *Nano Letters* **2016**, *16* (2), 1478-1484.
7. Mukherjee, S.; Libisch, F.; Large, N.; Neumann, O.; Brown, L. V.; Cheng, J.; Lassiter, J. B.; Carter, E. A.; Nordlander, P.; Halas, N. J., *Nano Letters* **2013**, *13* (1), 240-247.
8. Swearer, D. F.; Zhao, H.; Zhou, L.; Zhang, C.; Robotjazi, H.; Martirez, J. M. P.; Krauter, C. M.; Yazdi, S.; McClain, M. J.; Ringe, E.; Carter, E. A.; Nordlander, P.; Halas, N. J., *P. Natl. Acad. Sci USA* **2016**, *113* (32), 8916-8920.
9. Zhou, L.; Zhang, C.; McClain, M. J.; Manjavacas, A.; Krauter, C. M.; Tian, S.; Berg, F.; Everitt, H. O.; Carter, E. A.; Nordlander, P.; Halas, N. J., *Nano Letters* **2016**, *16* (2), 1478-1484.
10. Hou, W. B.; Hung, W. H.; Pavaskar, P.; Goepfert, A.; Aykol, M.; Cronin, S. B., *ACS Catalysis* **2011**, *1* (8), 929-936.
11. Robotjazi, H.; Zhao, H. Q.; Swearer, D. F.; Hogan, N. J.; Zhou, L. N.; Alabastri, A.; McClain, M. J.; Nordlander, P.; Halas, N. J., *Nature Communications* **2017**, *8*.
12. Martirez, J. M. P.; Carter, E. A., *Journal of the American Chemical Society* **2017**, *139* (12), 4390-4398.
13. Martirez, J. M. P.; Carter, E. A., *Science Advances* **2017**, *3* (12).
14. Christopher, P.; Xin, H.; Marimuthu, A.; Linic, S., *Nature Materials* **2012**, *11*, 1044.
15. Brongersma, M. L.; Halas, N. J.; Nordlander, P., *Nature Nanotechnology* **2015**, *10*, 25.
16. Zhou, L.; Swearer, D. F.; Zhang, C.; Robotjazi, H.; Zhao, H.; Henderson, L.; Dong, L.; Christopher, P.; Carter, E. A.; Nordlander, P.; Halas, N. J., *Science* **2018**, *362* (6410), 69.
17. Swearer, D. F.; Zhao, H.; Zhou, L.; Zhang, C.; Robotjazi, H.; Martirez, J. M. P.; Krauter, C. M.; Yazdi, S.; McClain, M. J.; Ringe, E.; Carter, E. A.; Nordlander, P.; Halas, N. J., *Proceedings of the National Academy of Sciences* **2016**, *113* (32), 8916-8920.

18. Zhang, C.; Zhao, H.; Zhou, L.; Schlather, A. E.; Dong, L.; McClain, M. J.; Swearer, D. F.; Nordlander, P.; Halas, N. J., *Nano Letters* **2016**, *16* (10), 6677-6682.
19. Robotjazi, H.; Zhao, H.; Swearer, D. F.; Hogan, N. J.; Zhou, L.; Alabastri, A.; McClain, M. J.; Nordlander, P.; Halas, N. J., *Nature Communications* **2017**, *8* (1), 27.
20. Aslam, U.; Chavez, S.; Linic, S., *Nature Nanotechnology* **2017**, *12*, 1000.
21. Linic, S.; Christopher, P.; Ingram, D. B., *Nature Materials* **2011**, *10*, 911.
22. Kelly, K. L.; Coronado, E.; Zhao, L. L.; Schatz, G. C., *The Journal of Physical Chemistry B* **2003**, *107* (3), 668-677.
23. Rycenga, M.; Cobley, C. M.; Zeng, J.; Li, W.; Moran, C. H.; Zhang, Q.; Qin, D.; Xia, Y., *Chemical Reviews* **2011**, *111* (6), 3669-3712.
24. Bohren, C. F., *American Journal of Physics* **1983**, *51* (4), 323-327.
25. Jiang; Bosnick, K.; Maillard, M.; Brus, L., *The Journal of Physical Chemistry B* **2003**, *107* (37), 9964-9972.
26. Ueno, K.; Oshikiri, T.; Sun, Q.; Shi, X.; Misawa, H., *Chemical Reviews* **2018**, *118* (6), 2955-2993.
27. Qiu, M.; Chen, X.; Shi, Y.; Chen, Y.; Gong, H.; Zhao, D.; Chen, X.; Yang, Y.; Yan, M.; Li, Q. In *Plasmonic enhanced photothermal effects and its applications*, 2014 16th International Conference on Transparent Optical Networks (ICTON), 6-10 July 2014; 2014; pp 1-2.
28. Blaber, M. G.; Arnold, M. D.; Ford, M. J., *Journal of Physics-Condensed Matter* **2010**, *22* (14).
29. Li, X. G.; Xiao, D.; Zhang, Z. Y., *New Journal of Physics* **2013**, *15*.
30. Hao, F.; Sonnefraud, Y.; Dorpe, P. V.; Maier, S. A.; Halas, N. J.; Nordlander, P., *Nano Letters* **2008**, *8* (11), 3983-3988.
31. Sundararaman, R.; Narang, P.; Jermyn, A. S.; Goddard Iii, W. A.; Atwater, H. A., *Nature Communications* **2014**, *5*, 5788.
32. Frischkorn, C.; Wolf, M., *Chemical Reviews* **2006**, *106* (10), 4207-4233.
33. Olsen, T.; Gavnholt, J.; Schiøtz, J., *Physical Review B* **2009**, *79* (3), 035403.
34. Olsen, T.; Schiøtz, J., *Physical Review Letters* **2009**, *103* (23), 238301.
35. Aslam, U.; Rao, V. G.; Chavez, S.; Linic, S., *Nature Catalysis* **2018**, *1* (9), 656-665.
36. Baeza, J. A.; Calvo, L.; Gilarranz, M. A.; Mohedano, A. F.; Casas, J. A.; Rodriguez, J. J., *J. Catal.* **2012**, *293* (0), 85-93.
37. Pretzer, L. A.; Song, H. J.; Fang, Y.-L.; Zhao, Z.; Guo, N.; Wu, T.; Arslan, I.; Miller, J. T.; Wong, M. S., *J. Catal.* **2013**, *298* (0), 206-217.
38. Prinz, J.; Pignedoli, C. A.; Stöckl, Q. S.; Armbrüster, M.; Brune, H.; Gröning, O.; Widmer, R.; Passerone, D., *J. Am. Chem. Soc.* **2014**, *136* (33), 11792-11798.
39. Pei, G. X.; Liu, X. Y.; Wang, A.; Lee, A. F.; Isaacs, M. A.; Li, L.; Pan, X.; Yang, X.; Wang, X.; Tai, Z.; Wilson, K.; Zhang, T., *ACS Catal* **2015**, *5* (6), 3717-3725.
40. Eller, F. J.; List, G. R.; Teel, J. A.; Steidley, K. R.; Adlof, R. O., *Journal of Agricultural and Food Chemistry* **2005**, *53* (15), 5982-5984.
41. Yu, W.; Porosoff, M. D.; Chen, J. G., *Chem. Rev.* **2012**, *112* (11), 5780-817.

42. Mukherjee, S.; Libisch, F.; Large, N.; Neumann, O.; Brown, L. V.; Cheng, J.; Lassiter, J. B.; Carter, E. A.; Nordlander, P.; Halas, N. J., *Nano Lett.* **2012**, *13* (1), 240-247.
43. Szydlo, N.; Poirier, R., *Journal of Applied Physics* **1980**, *51* (6), 3310-3312.
44. Mukherjee, S.; Libisch, F.; Large, N.; Neumann, O.; Brown, L. V.; Cheng, J.; Lassiter, J. B.; Carter, E. A.; Nordlander, P.; Halas, N. J., *Nano letters* **2013**, *13* (1), 240-7.
45. Mukherjee, S.; Zhou, L.; Goodman, A. M.; Large, N.; Ayala-Orozco, C.; Zhang, Y.; Nordlander, P.; Halas, N. J., *J. Am. Chem. Soc.* **2014**, *136* (1), 64-7.
46. Baffou, G.; Quidant, R.; Girard, C., *Appl. Phys. Lett.* **2009**, *94* (15), 153109-3.
47. Govorov, A. O.; Richardson, H. H., *Nano Today* **2007**, *2* (1), 30-38.
48. Johnson, P. B.; Christy, R. W., *Phys. Rev. B* **1972**, *6* (12), 4370-4379.
49. Fang, J.; Huang, Y.; Lew, C. M.; Yan, Y.; Pilon, L., *J. Appl. Phys.* **2012**, *111* (5), 054910-4.
50. Philipp, H. R., Silicon Dioxide (SiO₂) (Glass). In *Handbook of Optical Constants of Solids*, Edward, D. P., Ed. Academic Press: Burlington, 1997; pp 749-763.
51. Arup, S.; Debajyoti, D., *J PHYS D APPL PHYS* **2009**, *42* (21), 215404.
52. Lenz, D. H.; Conner Jr, W. C., *Journal of Catalysis* **1987**, *104* (2), 288-298.
53. Conner, W. C.; Falconer, J. L., *Chem. Rev.* **1995**, *95* (3), 759-788.
54. Valerii, V. R.; Oleg, V. K., *Russian Chemical Reviews* **1997**, *66* (2), 107.
55. Jabłoński, J. M.; Okal, J.; Potoczna-Petru, D.; Krajczyk, L., *J. Catal.* **2003**, *220* (1), 146-160.
56. McTaggart, F. K., *Nature* **1964**, *201* (4926), 1320-1321.
57. Han, G.; Sohn, H. Y., *J. Am. Ceram. Soc.* **2005**, *88* (4), 882-888.
58. Hass, G.; Salzberg, C. D., *J. Opt. Soc. Am.* **1954**, *44* (3), 181-183.
59. Langhammer, C.; Schwind, M.; Kasemo, B.; Zorić, I., *Nano Letters* **2008**, *8* (5), 1461-1471.
60. Knight, M. W.; King, N. S.; Liu, L.; Everitt, H. O.; Nordlander, P.; Halas, N. J., *ACS Nano* **2014**, *8* (1), 834-840.
61. Harris, J., *Langmuir* **1991**, *7* (11), 2528-2533.
62. Hammer, B.; Jacobsen, K. W.; Nørskov, J. K., *Surface Science* **1993**, *297* (1), L68-L72.
63. McClain, M. J.; Schlather, A. E.; Ringe, E.; King, N. S.; Liu, L.; Manjavacas, A.; Knight, M. W.; Kumar, I.; Whitmire, K. H.; Everitt, H. O.; Nordlander, P.; Halas, N. J., *Nano Letters* **2015**, *15* (4), 2751-2755.
64. Ehrenreich, H.; Philipp, H. R.; Segall, B., *Physical Review* **1963**, *132* (5), 1918-1928.
65. Avanesian, T.; Christopher, P., *The Journal of Physical Chemistry C* **2014**, *118* (48), 28017-28031.
66. Zheng, B. Y.; Zhao, H.; Manjavacas, A.; McClain, M.; Nordlander, P.; Halas, N. J., *Nature Communications* **2015**, *6*, 7797.
67. Baffou, G.; Rigneault, H., *Physical Review B* **2011**, *84* (3), 035415.

68. Linic, S.; Aslam, U.; Boerigter, C.; Morabito, M., *Nature Materials* **2015**, *14*, 567.
69. Hogan, N. J.; Urban, A. S.; Ayala-Orozco, C.; Pimpinelli, A.; Nordlander, P.; Halas, N. J., *Nano Letters* **2014**, *14* (8), 4640-4645.
70. Kiyomiya, M.; Momma, N.; Yasumori, I., *Bulletin of the Chemical Society of Japan* **1974**, *47* (8), 1852-1857.
71. Alexander, C. S.; Pritchard, J., *Journal of the Chemical Society, Faraday Transactions 1: Physical Chemistry in Condensed Phases* **1972**, *68* (0), 202-215.
72. Genger, T.; Hinrichsen, O.; Muhler, M., *Catalysis Letters* **1999**, *59* (2), 137-141.
73. Sakong, S.; Groß, A., *Surface Science* **2003**, *525* (1), 107-118.
74. Aiken, J. D.; Finke, R. G., *Journal of Molecular Catalysis A: Chemical* **1999**, *145* (1), 1-44.
75. Langhammer, C.; Kasemo, B.; Zorić, I., *The Journal of Chemical Physics* **2007**, *126* (19), 194702.
76. Pinchuk, A.; Kreibig, U.; Hilger, A., *Surface Science* **2004**, *557* (1), 269-280.
77. Swearer, D. F.; Leary, R. K.; Newell, R.; Yazdi, S.; Robotjazi, H.; Zhang, Y.; Renard, D.; Nordlander, P.; Midgley, P. A.; Halas, N. J.; Ringe, E., *ACS Nano* **2017**, *11* (10), 10281-10288.
78. Schüth, F.; Palkovits, R.; Schlögl, R.; Su, D. S., *Energy Environ. Sci.* **2012**, *5* (4), 6278-6289.
79. Ertl, G.; Huber, M., *Journal of Catalysis* **1980**, *61* (2), 537-539.
80. Bradford, M. C. J.; Fanning, P. E.; Vannice, M. A., *Journal of Catalysis* **1997**, *172* (2), 479-484.
81. Bell, T. E.; Torrente-Murciano, L., *Topics in Catalysis* **2016**, *59* (15), 1438-1457.
82. Rodriguez, J. A.; Goodman, D. W., *Science* **1992**, *257* (5072), 897.
83. Hinrichsen, O.; Genger, T.; Muhler, M., *Chemical Engineering and Technology* **2000**, *23* (11), 956-959.
84. Chan, G. H.; Zhao, J.; Hicks, E. M.; Schatz, G. C.; Van Duyne, R. P., *Nano Letters* **2007**, *7* (7), 1947-1952.
85. Zhang, X.; Li, X.; Zhang, D.; Su, N. Q.; Yang, W.; Everitt, H. O.; Liu, J., *Nature Communications* **2017**, *8*, 14542.
86. Song, H.; Meng, X.; Dao, T. D.; Zhou, W.; Liu, H.; Shi, L.; Zhang, H.; Nagao, T.; Kako, T.; Ye, J., *ACS Applied Materials & Interfaces* **2017**, *10* (1), 408-416.
87. Lynggaard, H.; Andreasen, A.; Stegelmann, C.; Stoltze, P., *Progress in Surface Science* **2004**, *77* (3), 71-137.
88. Tsai, W.; Weinberg, W. H., *The Journal of Physical Chemistry* **1987**, *91* (20), 5302-5307.
89. Egawa, C.; Nishida, T.; Naito, S.; Tamaru, K., *Journal of the Chemical Society, Faraday Transactions 1: Physical Chemistry in Condensed Phases* **1984**, *80* (6), 1595-1604.
90. Hellman, A.; Honkala, K.; Remediakis, I. N.; Logadóttir, Á.; Carlsson, A.; Dahl, S.; Christensen, C. H.; Nørskov, J. K., *Surface Science* **2009**, *603* (10), 1731-1739.

91. Prasad, V.; Karim, A. M.; Arya, A.; Vlachos, D. G., *Industrial & Engineering Chemistry Research* **2009**, *48* (11), 5255-5265.
92. Liu, J. G.; Zhang, H.; Link, S.; Nordlander, P., *ACS Photonics* **2017**.
93. Buntin, S. A.; Richter, L. J.; Cavanagh, R. R.; King, D. S., *Physical Review Letters* **1988**, *61* (11), 1321-1324.
94. Spata, V. A.; Carter, E. A., *ACS Nano* **2018**, *12* (4), 3512-3522.
95. Lavoie, J.-M., *Frontiers in Chemistry* **2014**, *2*, 81.
96. Arora, S.; Prasad, R., *RSC Advances* **2016**, *6* (110), 108668-108688.
97. Aramouni, N. A. K.; Touma, J. G.; Tarboush, B. A.; Zeaiter, J.; Ahmad, M. N., *Renewable and Sustainable Energy Reviews* **2018**, *82*, 2570-2585.
98. Pakhare, D.; Spivey, J., *Chemical Society Reviews* **2014**, *43* (22), 7813-7837.
99. Liu, H.; Li, M.; Dao, T. D.; Liu, Y.; Zhou, W.; Liu, L.; Meng, X.; Nagao, T.; Ye, J., *Nano Energy* **2016**, *26* (Complete), 398-404.
100. Song, H.; Meng, X.; Dao, T. D.; Zhou, W.; Liu, H.; Shi, L.; Zhang, H.; Nagao, T.; Kako, T.; Ye, J., *ACS Applied Materials & Interfaces* **2018**, *10* (1), 408-416.
101. Marcinkowski, M. D.; Darby, M. T.; Liu, J.; Wimble, J. M.; Lucci, F. R.; Lee, S.; Michaelides, A.; Flytzani-Stephanopoulos, M.; Stamatakis, M.; Sykes, E. C. H., *Nature Chemistry* **2018**, *10*, 325.
102. Hecht, H. G., *Journal of Research of NBS, Section A: Physics and Chemistry* **1976**, *80A* (4), 567.
103. Daza, Y. A.; Kuhn, J. N., *RSC Advances* **2016**, *6* (55), 49675-49691.
104. Jiao, F.; Li, J.; Pan, X.; Xiao, J.; Li, H.; Ma, H.; Wei, M.; Pan, Y.; Zhou, Z.; Li, M.; Miao, S.; Li, J.; Zhu, Y.; Xiao, D.; He, T.; Yang, J.; Qi, F.; Fu, Q.; Bao, X., *Science* **2016**, *351* (6277), 1065.
105. Luntz, A. C.; Persson, M.; Wagner, S.; Frischkorn, C.; Wolf, M., *The Journal of Chemical Physics* **2006**, *124* (24), 244702.
106. Chase Jr, M. W., *NIST-JANAF thermochemical tables, Fourth Edition*. 1998; Vol. 9, p 1-1951.
107. Simakov, D. S. A.; Wright, M. M.; Ahmed, S.; Mokheimer, E. M. A.; Roman-Leshkov, Y., *Catalysis Science & Technology* **2015**, *5* (4), 1991-2016.
108. Said, S. A. M.; Waseuddin, M.; Simakov, D. S. A., *Renewable and Sustainable Energy Reviews* **2016**, *59*, 149-159.
109. Kodama, T.; Kiyama, A.; Shimizu, K. I., *Energy & Fuels* **2003**, *17* (1), 13-17.